Eur. Phys. J. C manuscript No.
(will be inserted by the editor)

Towards an Understanding of the Correlations in Jet Substructure

Report of BOOST2013, hosted by the University of Arizona, 12^{th}-16^{th} of August 2013.

D. Adams[1], A. Arce[2], L. Asquith[3], M. Backovic[4], T. Barillari[5], P. Berta[6], D. Bertolini[2], A. Buckley[8], J. Butterworth[9], R. C. Camacho Toro[10], J. Caudron[9], Y.-T. Chien[11], J. Cogan[12], B. Cooper[9], D. Curtin[17], C. Debenedetti[18], J. Dolen[9], M. Eklund[22], S. El Hedri[22], S. D. Ellis[22], T. Embry[22], D. Ferencek[23], J. Ferrando[24], S. Fleischmann[16], M. Freytsis[25], M. Giulini[21], Z. Han[27], D. Hare[4], P. Harris[4], A. Hinzmann[4], R. Hoing[4], A. Hornig[22], M. Jankowiak[4], K. Johns[28], G. Kasieczka[23], T. Knight[24], G. Kasieczka[29], R. Kogler[30], W. Lampl[4], A. J. Larkoski[4], C. Lee[31], R. Leone[31], P. Loch[31], D. Lopez Mateos[27], H. K. Lou[27], M. Low[27], P. Maksimovic[32], I. Marchesini[32], S. Marzani[32], L. Masetti[33], R. McCarthy[32], S. Menke[32], D. W. Miller[35], K. Mishra[36], B. Nachman[32], P. Nef[4], F. T. O'Grady[24], A. Ovcharova[23], A. Picazio[37], C. Pollard[38], B. Potter Landua[29], C. Potter[29], S. Rappoccio[39], J. Rojo[48], J. Rutherfoord[40], G. P. Salam[10,11], J. Schabinger[23], A. Schwartzman[4], M. D. Schwartz[27], B. Shuve[43], P. Sinervo[44], D. Soper[45], D. E. Sosa Corral[45], M. Spannowsky[32], E. Strauss[34], M. Swiatlowski[4], J. Thaler[34], C. Thomas[34], E. Thompson[1], N. V. Tran[36], J. Tseng[36], E. Usai[36], L. Valery[36], J. Veatch[23], M. Vos[23], W. Waalewijn[4], and C. Young[47]

[1] *Columbia University, Nevis Laboratory, Irvington, NY 10533, USA*
[2] *Duke University, Durham, NC 27708, USA*
[3] *Argonne National Laboratory, Lemont, IL 60439, USA*
[4] *SLAC National Accelerator Laboratory, Menlo Park, CA 94025, USA*
[5] *Deutsches Elektronen-Synchrotron, DESY, D-15738 Zeuthen, Germany*
[6] *Cornell University, Ithaca, NY 14853, USA*
[7] *Lund University, Lund, SE 22100, Sweden*
[8] *University of Edinburgh, EH9 3JZ, UK*
[9] *University College London, WC1E 6BT, UK*
[10] *LPTHE, UPMC Univ. Paris 6 and CNRS UMR 7589, Paris, France*
[11] *CERN, CH-1211 Geneva 23, Switzerland*
[12] *CAFPE and U. of Granada, Granada, E-18071, Spain*
[13] *McGill University, Montreal, Quebec H3A 2T8, Canada*
[14] *Iowa State University, Ames, Iowa 50011, USA*
[15] *Rutgers University, Piscataway, NJ 08854, USA*
[16] *Bergische Universitaet Wuppertal, Wuppertal, D-42097, Germany*
[17] *YITP, Stony Brook University, Stony Brook, NY 11794-3840, USA*
[18] *University of Manchester, Manchester, M13 9PL, UK*
[19] *UNESP - Universidade Estadual Paulista, Sao Paulo, 01140-070, Brazil*
[20] *INFN and University of Naples, IT80216, Italy*
[21] *University of Geneva, CH-1211 Geneva 4, Switzerland*
[22] *University of Washington, Seattle, WA 98195, USA*
[23] *Instituto de Física Corpuscular, IFIC/CSIC-UVEG, E-46071 Valencia, Spain*
[24] *University of Glasgow, Glasgow, G12 8QQ, UK*
[25] *Berkeley National Laboratory, University of California, Berkeley, CA 94720, USA*
[26] *Universidad de Buenos Aires, AR-1428, Argentina*
[27] *Harvard University, Cambridge, MA 02138, USA*
[28] *Weizmann Institute, 76100 Rehovot, Israel*
[29] *Universitaet Hamburg, DE-22761, Germany*
[30] *Universitaet Heidelberg, DE-69117, Germany*
[31] *University of Arizona, Tucson, AZ 85719, USA*
[32] *IPPP, University of Durham, Durham, DH1 3LE, UK*
[33] *Universitaet Mainz, DE 55099, Germany*
[34] *MIT, Cambridge, MA 02139, USA*
[35] *University of Chicago, IL 60637, USA*
[36] *Fermi National Accelerator Laboratory, Batavia, IL 60510, USA*
[37] *Indiana University, Bloomington, IN 47405, USA*
[38] *University of California, Davis, CA 95616, USA*
[39] *Johns Hopkins University, Baltimore, MD 21218, USA*
[40] *INFN and University of Pisa, Pisa, IT-56127, Italy*
[41] *Texas A & M University, College Station, TX 77843, USA*
[42] *INFN and University of Calabria, Rende, IT-87036, Italy*
[43] *Brown University, Richmond, RI 02912, USA*
[44] *Yale University, New Haven, CT 06511, USA*
[45] *CEA Saclay, Gif-sur-Yvette, FR-91191, France*
[46] *University of Illinois, Chicago, IL 60607, USA*
[47] *University of California, Berkeley, CA 94720, USA*

Abstract Insert your abstract here. Insert your abstract here. Insert your abstract here. Insert your abstract here. Insert your abstract here. Insert your abstract here. Insert your abstract here. Insert your abstract here. Insert your abstract here.

1 Introduction

The characteristic feature of collisions at the LHC is a center-of-mass energy, 7 TeV in 2010 and 2011, of 8 TeV in 2012, and near 14 TeV with the start of the second phase of operation in 2015, that is large compared to even the heaviest of the known particles. Thus these particles (and also previously unknown ones) will often be produced at the LHC with substantial boosts. As a result, when decaying hadronically, these particles will not be observed as multiple jets in the detector, but rather as a single hadronic jet with distinctive internal substructure. This realization has led to a new era of sophistication in our understanding of both standard QCD jets and jets containing the decay of a heavy particle, with an array of new jet observables and detection techniques introduced and studies. To allow the efficient sharing of results from these jet substructure studies a series of BOOST Workshops have been held on a yearly basis: SLAC (2009, [1]), Oxford University (2010, [2]), Princeton University University (2011, [3]), IFIC Valencia (2012 [4]), University of Arizona (2013 [5]), and, most recently, University College London (2014 [6]). After each of these meetings Working Groups have functioned during the following year to generate reports highlighting the most interesting new results, including studies of ever maturing details. Previous BOOST reports can be found at [7–9].

This report from BOOST 2013 thus views the study and implementation of jet substructure techniques as a fairly mature field, and focuses on the question of the correlations between the plethora of observables that have been developed and employed, and their dependence on the underlying jet parameters, especially the jet radius R and jet p_T. Samples of quark-, gluon-, W- and Top-initiated jets are reconstructed at the particle-level using FASTJET [10], and the performance, in terms of separating signal from background, of various groomed jet masses and jet substructure observables investigated through Receiver Operating Characteristic (ROC) curves, which show the efficiency to "tag" the signal as a function of the efficiency (or rejection, being 1/efficiency) to "tag" the background. We investigate the separation of a quark signal from a gluon background (q/g tagging), a W signal from a gluon background (W-tagging) and a Top signal from a mixed quark/gluon QCD background (Top-tagging). In the case of Top-tagging, we also investigate the performance of dedicated Top-tagging algorithms, the HepTopTagger [11] and the Johns Hopkins Tagger [12]. Using multivariate techniques, we study the degree to which the discriminatory information provided by the observables and taggers overlaps, by examining in particular the extent to which the signal-background separation performance increases when two or more variables/taggers are combined, via a Boosted Decision Tree (BDT), into a single discriminant.

The report is organized as follows. In Section 2 we describe the generation of the Monte Carlo event samples that we use in the studies that follow. In Section 3 we detail the jet algorithms, observables and taggers investigated in each section of the report, and in Section 4 the multivariate techniques used to combine the one or more of the observables into single discriminants. In Section 5 we describe the q/g-tagging studies, in Section 6 we describe the W-tagging studies, and in Section 7 we describe the Top-tagging studies. Finally we offer some summary of the studies and general conclusions in Section 8.

2 Monte Carlo Samples

In the below sections the Monte Carlo samples used in the q/g tagging, W tagging and Top tagging sections of this report are described. Note that in all cases the samples used contain no additional proton-proton interactions beyond the hard scatter (no pile-up), and there is no attempt to emulate the degradation in angular and p_T resolution that would result when reconstructing the jets inside a real detector.

2.1 Quark/gluon and W tagging

Samples were generated at $\sqrt{s} = 8$ TeV for QCD dijets, and for W^+W^- pairs produced in the decay of a (pseudo) scalar resonance and decaying hadronically. The QCD events were split into subsamples of gg and $q\bar{q}$ events, allowing for tests of discrimination of hadronic W bosons, quarks, and gluons.

Individual gg and $q\bar{q}$ samples were produced at leading order (LO) using MADGRAPH5 [13], while W^+W^- samples were generated using the JHU GENERATOR [14–16] to allow for separation of longitudinal and transverse polarizations. Both were generated using CTEQ6L1 PDFs [17]. The samples were produced in exclusive p_T bins of width 100 GeV, with the slicing parameter chosen to be the p_T of any final state parton or W at LO. At the parton-level the p_T bins investigated were 300-400 GeV, 500-600 GeV and 1.0-1.1 TeV. Since no matching was performed, a cut on any parton was equivalent. The samples were then all showered through PYTHIA8 (version 8.176) [18] using the default tune 4C [19]. For each of the various samples (W,q,g) and p_T bins, 500,000 events were simulated.

2.2 Top tagging

Samples were generated at $\sqrt{s} = 14$ TeV. Standard Model dijet and top pair samples were produced with SHERPA 2.0.0 [20–25], with matrix elements of up to two extra partons matched to the shower. The top samples included only hadronic decays and were generated in exclusive p_T bins of width 100 GeV, taking as slicing parameter the maximum of the top/anti-top p_T. The QCD samples were generated with a cut on the leading parton-level jet p_T, where parton-level jets are clustered with the anti-k_t algorithm and jet radii of $R = 0.4, 0.8, 1.2$. The matching scale is selected to be $Q_{\text{cut}} = 40, 60, 80$ GeV for the $p_{T\,\text{min}} = 600, 1000$, and 1500 GeV bins, respectively. For the top samples, 100k events were generated in each bin, while 200k QCD events were generated in each bin.

3 Jet Algorithms and Substructure Observables

In this section, we define the jet algorithms and observables used in our analysis. Over the course of our study, we considered a larger set of observables, but for the final analysis, we eliminated redundant observables for presentation purposes. In Sections 3.1, 3.2, 3.3 and 3.4 we first describe the various jet algorithms, groomers, taggers and other substructure variables used in these studies.

3.1 Jet Clustering Algorithms

Jet clustering: Jets were clustered using sequential jet clustering algorithms [26] implemented in FASTJET 3.0.3. Final state particles i, j are assigned a mutual distance d_{ij} and a distance to the beam, $d_{i\text{B}}$. The particle pair with smallest d_{ij} are recombined and the algorithm repeated until the smallest distance is instead the distance to the beam, $d_{i\text{B}}$, in which case i is set aside and labelled as a jet. The distance metrics are defined as

$$d_{ij} = \min(p_{Ti}^{2\gamma}, p_{Tj}^{2\gamma}) \frac{\Delta R_{ij}^2}{R^2}, \tag{1}$$

$$d_{i\text{B}} = p_{Ti}^{2\gamma}, \tag{2}$$

where $\Delta R_{ij}^2 = (\Delta\eta)^2 + (\Delta\phi)^2$. In this analysis, we use the anti-k_t algorithm ($\gamma = -1$) [27], the Cambridge/Aachen (C/A) algorithm ($\gamma = 0$) [28, 29], and the k_t algorithm ($\gamma = 1$) [30, 31], each of which has varying sensitivity to soft radiation in defining the jet.

Qjets: We also perform non-deterministic jet clustering [32, 33]. Instead of always clustering the particle pair with smallest distance d_{ij}, the pair selected for combination is chosen probabilistically according to a measure

$$P_{ij} \propto e^{-\alpha(d_{ij}-d_{\min})/d_{\min}}, \tag{3}$$

where $d_{\min}$ is the minimum distance for the usual jet clustering algorithm at a particular step. This leads to a different cluster sequence for the jet each time the Qjet algorithm is used, and consequently different substructure properties. The parameter α is called the rigidity and is used to control how sharply peaked the probability distribution is around the usual, deterministic value. The Qjets method uses statistical analysis of the resulting distributions to extract more information from the jet than can be found in the usual cluster sequence. We use $\alpha = 0.1$ and 25 trees per event for all of the studies presented here.

3.2 Jet Grooming Algorithms

Pruning: Given a jet, re-cluster the constituents using the C/A algorithm. At each step, proceed with the merger as usual unless both

$$\frac{\min(p_{Ti}, p_{Tj})}{p_{Tij}} < z_{\text{cut}} \text{ and } \Delta R_{ij} > \frac{2m_j}{p_{Tj}} R_{\text{cut}}, \tag{4}$$

in which case the merger is vetoed and the softer branch discarded. The default parameters used for pruning [34] in this study are $z_{\text{cut}} = 0.1$ and $R_{\text{cut}} = 0.5$. One advantage of pruning is that the thresholds used to veto soft, wide-angle radiation scale with the jet kinematics, and so the algorithm is expected to perform comparably over a wide range of momenta.

Trimming: Given a jet, re-cluster the constituents into subjets of radius R_{trim} with the k_t algorithm. Discard all subjets i with

$$p_{Ti} < f_{\text{cut}}\, p_{TJ}. \tag{5}$$

The default parameters used for trimming [35] in this study are $R_{\text{trim}} = 0.2$ and $f_{\text{cut}} = 0.03$.

Filtering: Given a jet, re-cluster the constituents into subjets of radius R_{filt} with the C/A algorithm. Re-define the jet to consist of only the hardest N subjets, where N is determined by the final state topology and is typically one more than the number of hard prongs in the resonance decay (to include the leading final-state gluon emission) [36]. While we do not independently use filtering, it is an important step of the HEPTopTagger to be defined later.

Soft drop: Given a jet, re-cluster all of the constituents using the C/A algorithm. Iteratively undo the last stage of the C/A clustering from j into subjets j_1, j_2. If

$$\frac{\min(p_{T1}, p_{T2})}{p_{T1} + p_{T2}} < z_{\text{cut}} \left(\frac{\Delta R_{12}}{R}\right)^{\beta}, \tag{6}$$

discard the softer subjet and repeat. Otherwise, take j to be the final soft-drop jet [37]. Soft drop has two input parameters, the angular exponent β and the soft-drop scale z_{cut}, with default value $z_{\mathrm{cut}} = 0.1$. **ED: Soft-drop actually functions as a tagger when $\beta = -1$**

3.3 Jet Tagging Algorithms

Modified Mass Drop Tagger: Given a jet, re-cluster all of the constituents using the C/A algorithm. Iteratively undo the last stage of the C/A clustering from j into subjets j_1, j_2 with $m_{j_1} > m_{j_2}$. If either

$$m_{j_1} > \mu\, m_j \text{ or } \frac{\min(p_{T1}^2, p_{T2}^2)}{m_j^2} \Delta R_{12}^2 < y_{\mathrm{cut}}, \tag{7}$$

then discard the branch with the smaller transverse mass $m_T = \sqrt{m_i^2 + p_{Ti}^2}$, and re-define j as the branch with the larger transverse mass. Otherwise, the jet is tagged. If de-clustering continues until only one branch remains, the jet is untagged [38]. In this study we use by default $\mu = 1.0$ and $y_{\mathrm{cut}} = 0.1$.

Johns Hopkins Tagger: Re-cluster the jet using the C/A algorithm. The jet is iteratively de-clustered, and at each step the softer prong is discarded if its p_{T} is less than $\delta_p\, p_{\mathrm{T\,jet}}$. This continues until both prongs are harder than the p_{T} threshold, both prongs are softer than the p_{T} threshold, or if they are too close ($|\Delta\eta_{ij}| + |\Delta\phi_{ij}| < \delta_R$); the jet is rejected if either of the latter conditions apply. If both are harder than the p_{T} threshold, the same procedure is applied to each: this results in 2, 3, or 4 subjets. If there exist 3 or 4 subjets, then the jet is accepted: the top candidate is the sum of the subjets, and W candidate is the pair of subjets closest to the W mass [12]. The output of the tagger is m_t, m_W, and θ_{h}, a helicity angle defined as the angle, measured in the rest frame of the W candidate, between the top direction and one of the W decay products. The two free input parameters of the John Hopkins tagger in this study are δ_p and δ_R, defined above.

HEPTopTagger: Re-cluster the jet using the C/A algorithm. The jet is iteratively de-clustered, and at each step the softer prong is discarded if $m_1/m_{12} > \mu$ (there is not a significant mass drop). Otherwise, both prongs are kept. This continues until a prong has a mass $m_i < m$, at which point it is added to the list of subjets. Filter the jet using $R_{\mathrm{filt}} = \min(0.3, \Delta R_{ij})$, keeping the five hardest subjets (where ΔR_{ij} is the distance between the two hardest subjets). Select the three subjets whose invariant mass is closest to m_t [11]. The output of the tagger is m_t, m_W, and θ_{h}, a helicity angle defined as the angle, measured in the rest frame of the W candidate, between the top direction and one of the W decay products. The two free input parameters of the HEPTopTagger in this study are m and μ, defined above.

Top Tagging with Pruning: For comparison with the other top taggers, we add a W reconstruction step to the trimming algorithm described above. A W candidate is found as follows: if there are two subjets, the highest-mass subjet is the W candidate (because the W prongs end up clustered in the same subjet); if there are three subjets, the two subjets with the smallest invariant mass comprise the W candidate. In the case of only one subjet, no W is reconstructed.

Top Tagging with Trimming: For comparison with the other top taggers, we add a W reconstruction step to the trimming algorithm described above. A W candidate is found as follows: if there are two subjets, the highest-mass subjet is the W candidate (because the W prongs end up clustered in the same subjet); if there are three subjets, the two subjets with the smallest invariant mass comprise the W candidate. In the case of only one subjet, no W is reconstructed.

3.4 Other Jet Substructure Observables

Qjet mass volatility: As described above, Qjet algorithms re-cluster the same jet non-deterministically to obtain a collection of interpretations of the jet. For each jet interpretation, the pruned jet mass is computed with the default pruning parameters. The mass volatility, Γ_{Qjet}, is defined as [32]

$$\Gamma_{\mathrm{Qjet}} = \frac{\sqrt{\langle m_J^2\rangle - \langle m_J\rangle^2}}{\langle m_J\rangle}, \tag{8}$$

where averages are computed over the Qjet interpretations.

***N*-subjettiness:** N-subjettiness [39] quantifies how well the radiation in the jet is aligned along N directions. To compute N-subjettiness, $\tau_N^{(\beta)}$, one must first identify N axes within the jet. Then,

$$\tau_N = \frac{1}{d_0} \sum_i p_{Ti} \min\left(\Delta R_{1i}^{\beta}, \ldots, \Delta R_{Ni}^{\beta}\right), \tag{9}$$

where distances are between particles i in the jet and the axes,

$$d_0 = \sum_i p_{Ti} R^{\beta} \tag{10}$$

and R is the jet clustering radius. The exponent β is a free parameter. There is also some choice in how the axes used to compute N-subjettiness are determined. The optimal configuration of axes is the one that minimizes N-subjettiness; recently, it was shown that the "winner-takes-all" (WTA) axes can be easily computed and have superior performance compared to other minimization techniques [40]. We use both the WTA and one-pass k_t optimization axes in our analyses.

A more powerful discriminant is often the ratio,

$$\tau_{N,N-1} \equiv \frac{\tau_N}{\tau_{N-1}}. \tag{11}$$

While this is not an infrared-collinear (IRC) safe observable, it is calculable [41] and can be made IRC safe with a loose lower cut on τ_{N-1}.

Energy correlation functions: The transverse momentum version of the energy correlation functions are defined as [42]:

$$\mathrm{ECF}(N,\beta) = \sum_{i_1<i_2<\ldots<i_N \in j} \left(\prod_{a=1}^{N} p_{Ti_a}\right)\left(\prod_{b=1}^{N-1}\prod_{c=b+1}^{N} \Delta R_{i_b i_c}\right)^{\beta}, \tag{12}$$

where i is a particle inside the jet. It is preferable to work in terms of dimensionless quantities, particularly the energy correlation function double ratio:

$$C_N^{(\beta)} = \frac{\mathrm{ECF}(N+1,\beta)\,\mathrm{ECF}(N-1,\beta)}{\mathrm{ECF}(N,\beta)^2}. \tag{13}$$

This observable measures higher-order radiation from leading-order substructure.

4 Multivariate Analysis Techniques

Multivariate techniques are used to combine variables into an optimal discriminant. In all cases variables are combined using a boosted decision tree (BDT) as implemented in the TMVA package [43]. We use the BDT implementation including gradient boost. An example of the BDT settings are as follows:

- NTrees=1000
- BoostType=Grad
- Shrinkage=0.1
- UseBaggedGrad=F
- nCuts=10000
- MaxDepth=3
- UseYesNoLeaf=F
- nEventsMin=200

Exact parameter values are chosen to best reduce the effect of overtraining. Additionally, the simulated data were split into training and testing samples and comparisons of the BDT output were compared to reduced the effect of overtraining as well.

5 Quark-Gluon Discrimination

In this section, we examine the differences between quark- and gluon-initiated jets in terms of substructure variables, and to determine to what extent these variables are correlated. Along the way, we provide some theoretical understanding of these observables and their performance. The motivation for these studies comes not only from the desire to "tag" a jet as originating from a quark or gluon, but also to improve our understanding of the quark and gluon components of the QCD backgrounds relative to boosted resonances. While recent studies have suggested that quark/gluon tagging efficiencies depend highly on the Monte Carlo generator used[44, 45], we are more interested in understanding the scaling performance with p_T and R, and the correlations between observables, which are expected to be treated consistently within a single shower scheme.

5.1 Methodology

These studies use the qq and gg MC samples, described previously in Section 2. The showered events were clustered with FastJet 3.03 using the anti-k_{T} algorithm with jet radii of $R = 0.4, 0.8, 1.2$. In both signal (quark) and background (gluon) samples, an upper and lower cut on the leading jet p_T is applied after showering/clustering, to ensure similar p_T spectra for signal and background in each p_T bin. The bins in leading jet p_T that are considered are 300-400 GeV, 500-600 GeV, 1.0-1.1 TeV, for the 300-400 GeV, 500-600 GeV, 1.0-1.1 TeV parton p_T slices respectively. Various jet grooming approaches are applied to the jets, as described in Section 3.4. Only leading and subleading jets in each sample are used. The following observables are studied in this section:

- The number of constituents (N_{constits}) in the jet.
- The pruned Qjet mass volatility, Γ_{Qjet}.
- 1-point energy correlation functions, C_1^{β} with $\beta = 0, 1, 2$.
- 1-subjettiness, τ_1^{β} with $\beta = 1, 2$. The N-subjettiness axes are computed using one-pass k_t axis optimization.
- The ungroomed jet mass, m.

We will see below that, in terms of their jet-by-jet correlations and their ability to separate quark initiated jets from gluon initiated jets (hereafter called simply quark jets and gluon jets), these observables fall into five classes. The first three, N_{constits}, Γ_{Qjet} and $C_1^{\beta=0}$, form classes by themselves (Classes I to III) in the sense that they each carry some independent information about a jet and, when combined, provide substantially better quark jet and gluon jet separation than either observable by itself. Of the remaining observables, $C_1^{\beta=1}$ and $\tau_1^{\beta=1}$ comprise a single class (Class IV) in the sense that they exhibit similar distributions when applied to a sample of jets, their jet-by-jet values are highly correlated, they exhibit very similar power to separate quark jets and gluon jets (with very similar dependence on the jet parameters R and p_T) and this separation power is essentially unchanged when they are combined. The fifth class (Class V) is composed of $C_1^{\beta=2}$, $\tau_1^{\beta=2}$ and the (ungroomed) jet mass. Again the issue is that jet-by-jet correlations are strong (even though the individual observable distributions are somewhat different), quark versus gluon separation power is very similar (including the R and p_T dependence) and little is achieved by combining more than one of these observables. This class structure is not surprising given that within a class the observables exhibit very similar dependence on the kinematics of the underlying jet constituents. For example, the members of Class V are constructed from of a sum over pairs of constituents using products of the energy of each member of the pair times the angular separation squared for the pair (for the mass case think in terms of mass squared with small angular separations). By the same argument the Class IV and Class V observables will be seen to be more similar than any other pair of classes, differing only in the power (β) of the dependence on the angular separations, which will produce small but detectable differences. We will return to a more complete discussion of jet masses at the end of Section 5.

5.2 Single Variable Discrimination

The quark and gluon distributions of different substructure observables are shown in Figure 1, which already illustrates at least some of the points about the Classes made above. At a fundamental level the primary difference between quark jets and gluon jets is the color charge of the initiating parton, typically expressed in terms of the ratio of the corresponding Casimir factors $C_F/C_A = 4/9$. Since the quark has the smaller color charge, it will radiate less than a corresponding gluon and the resulting jet will contain fewer constituents. This difference is clearly indicated in Figure 1(a), suggesting that simply counting constituents will provide good separation between quark and gluon jets. In fact, among the observables considered, one can see by eye that N_{constits} should provide the highest separation power, *i.e.*, the quark and gluon distributions are most distinct, as was originally noted in [45, 46]. Figure 1 further suggests that $C_1^{\beta=0}$ should provide the next best separation followed by $C_1^{\beta=1}$, as was also found by the CMS and ATLAS Collaborations[44].

To more quantitatively study the power of each observable as a discriminator for quark/gluon tagging, ROC curves are built by scanning each distribution and plotting the background efficiency (to select gluon jets) vs. the signal efficiency (to select quark jets). Figure 2 shows these ROC curves for all of the substructure variables shown in Figure 1, along with the ungroomed mass, representing the best performing mass variable, for R=0.4, 0.8 and 1.2 jets in the $p_T = 300-400$ GeV bin. In addition, the ROC curve for a tagger built from a BDT combination of all the variables (see Section 4) is shown. Clearly, and as suggested earlier, n_{constits} is the best performing variable for all Rs, even though $C_1^{\beta=0}$ is close, particularly for R=0.8. Most other variables have similar performance, except Γ_{Qjet}, which shows significantly worse discrimination (this may be due to our choice of rigidity $\alpha = 0.1$, with other studies suggesting that a smaller value, such as $\alpha = 0.01$, produces better results[32, 33]). The combination of all variables shows somewhat better discrimination, and we will discuss in more detail below the correlations between the observables and their impact on the combined discrimination power.

We now examine how the performance of the substructure observables changes with p_T and R. To present the results in a "digestible" fashion we will focus on the gluon jet "rejection" factor, $1/\varepsilon_{\text{bkg}}$, for a quark signal efficiency, ε_{sig}, of 50%. We can use the values of $1/\varepsilon_{\text{bkg}}$ generated for the 9 kinematic points introduced above ($R = 0.4, 0.8, 1.2$ and the 100 GeV p_T bins with lower limits $p_T = 300$ GeV, 500 GeV, 1000 GeV) to generate surface plots. The surface plots in Figure 3 indicate both the level of gluon rejection and the variation with p_T and R for each of the studied single observable. The color shading is defined so that a change in color corresponds to a change of about 0.4 in $1/\varepsilon_{\text{bkg}}$. The colors have the same correlation with the magnitude of $1/\varepsilon_{\text{bkg}}$ in all of the plots, but repeat after a change of about 4. Thus "blue" corresponds to a value of about 2.5 in Figure 3(b) and the values 6.5 and 10.5 in Figure 3(a), while "yellow" corresponds to about 5 in Figures 3(c) to (h) and about 9 in Figure 3(a).

We see, as expected, that the numerically largest rejection rates occur for the observable N_{constits} in Figure 3(a), where the rejection factor is in the range 6 to 11 and varies rather dramatically with R. As R increases the jet collects more constituents from the underlying event, which are the same for quark and gluon jets, and the separation power decreases. At large R, there is some improvement with increasing p_T due to the enhanced radiation, which does distinguish quarks from gluons. Figure 3(b) confirms the limited efficacy of the single observable Γ_{Qjet} (at least for our parameter choices) with a rejection rate only in the range 2.5 to 2.8. On the other hand, this observable probes a very different property of jet substructure, *i.e.*, the sensitivity to detailed changes in the grooming procedure, and this difference is suggested by the distinct R and p_T dependence illustrated in Figure 3(b). The rejection rate increases with increasing R and decreasing p_T, since the distinction between quark and gluon jets for this observable arises from the relative importance of the one "hard" gluon emission configuration.

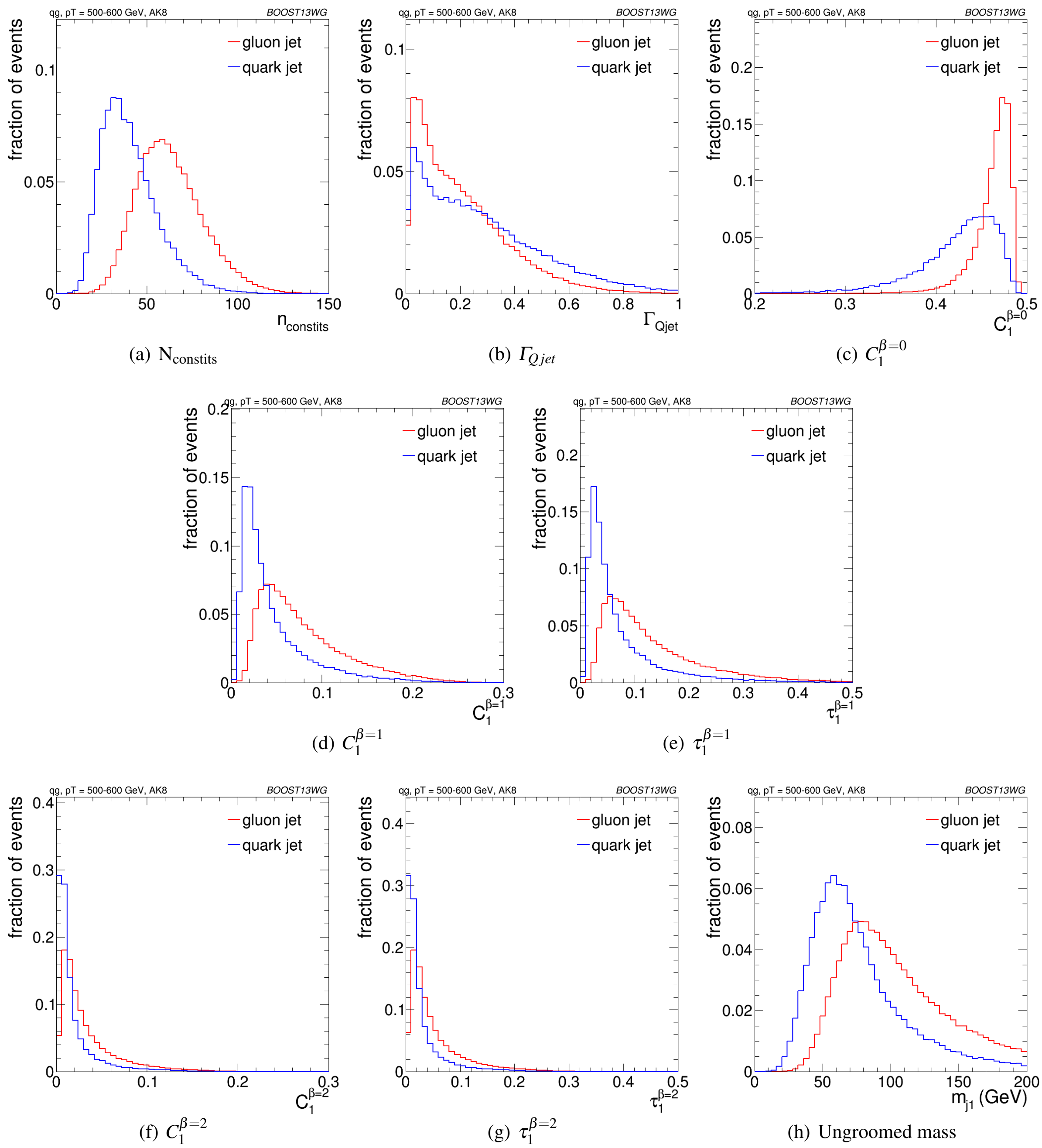

(a) $\mathrm{N_{constits}}$ (b) Γ_{Qjet} (c) $C_1^{\beta=0}$

(d) $C_1^{\beta=1}$ (e) $\tau_1^{\beta=1}$

(f) $C_1^{\beta=2}$ (g) $\tau_1^{\beta=2}$ (h) Ungroomed mass

Fig. 1 Comparisons of quark and gluon distributions of different substructure variables (organized by Class) for leading jets in the $p_T = 500-600$ GeV bin using the anti-k_{T} $R = 0.8$ algorithm.

The role of this contribution is enhanced for both decreasing p_T and increasing R. Figure 3(c) indicates that the observable $C_1^{\beta=0}$ can, by itself, provide a rejection rate in the range 7.8 to 8.6 (intermediate between the two previous observables) and again with distinct R and p_T dependence. In this case the rejection rate decreases slowly with increasing R ($\beta = 0$ explicitly means that the angular dependence is much reduced), while the rejection rate peaks at intermediate p_T values (an effect visually enhanced by the limited number of p_T values included). Both the distinct values of the rejection rates and the differing R and p_T dependence serve to confirm that these three observables tend to probe independent features of the quark and gluon jets.

Figures 3(d) and (e) serve to confirm the very similar properties of the Class IV observables $C_1^{\beta=1}$ and $\tau_1^{\beta=1}$ (as already suggested in Figures 1(d) and (e)) with essentially identical rejection rates (4.1 to 5.4) and identical R and p_T dependence (a slow decrease with increasing R and an even

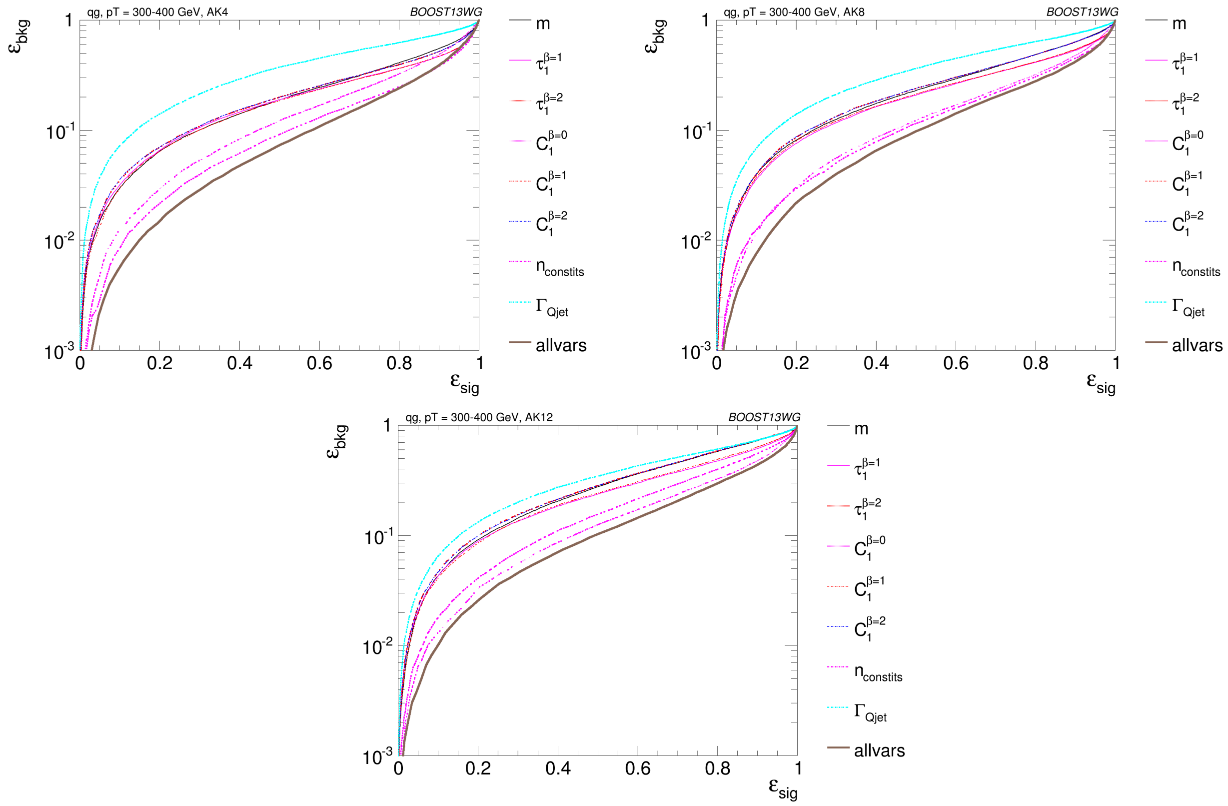

Fig. 2 The ROC curve for all single variables considered for quark-gluon discrimination in the p_T 300-400 GeV bin using the anti-k_T R=0.4, 0.8 and 1.2 algorithm.

slower increase with increasing p_T). A similar conclusion for the Class V observables $C_1^{\beta=2}$, $\tau_1^{\beta=2}$ and m with similar rejection rates in the range 3.5 to 5.3 and very similar R and p_T dependence (a slow decrease with increasing R and an even slower increase with increasing p_T). Arguably, drawing a distinction between the Class IV and Class V observables, is a fine point, but the color shading does suggest some distinction from the slightly smaller rejection rate in Class V. Again the strong similarities between the plots within the second and third rows in Figure 3 speaks to the common properties of the observables within the two classes.

In summary, the overall discriminating power between quark and gluon jets tends to decrease with increasing R, except for the Γ_{Qjet} observable, presumably primarily due to the increasing contamination from the underlying event. Since the construction of the Γ_{Qjet} observable explicitly involves pruning away the soft, large angle constituents, it is not surprising that it exhibits different R dependence. In general the discriminating power increases slowly and monotonically with p_T (except for the Γ_{Qjet} and $C_1^{\beta=0}$ observables) presumably because there is overall more (color charge related) radiation as p_T increasing providing some increase in discrimination (except for the Γ_{Qjet} observable). We turn now to the question of the impact of employing more than one observable at a time.

5.3 Combined Performance and Correlations

The quark/gluon tagging performance can be further improved over cuts on single observables by combining multiple observables in a BDT; due to the challenging nature of q/g-tagging, any improvement in performance with multivariable techniques could be critical for certain analyses, and the improvement could be more substantial in data than the marginal benefit found in MC and shown in Fig. 2. Furthermore, insight can be gained into the features allowing for quark/gluon discrimination if the origin of the improvement is understood. To quantitatively study this improvement, we build quark/gluon taggers from every pair-wise combination of variables studied in the previous section for comparison with the all-variable combination. To illustrate the results achieved in this way we will exhibit the same sort 2D of surface plots as in Figure 3. Based on our discussion of the correlated properties of observables within a single class, we expect little improvement in the rejection rate when combining observables from the same class and substantial improvement when combining observables from different classes.

Figure 4 shows pairwise plots for (a) Class IV and (b) Class V. Comparing to the corresponding plots in Figure 3 we see that combining $C_1^{\beta=1}+\tau_1^{\beta=1}$ provides a small im-

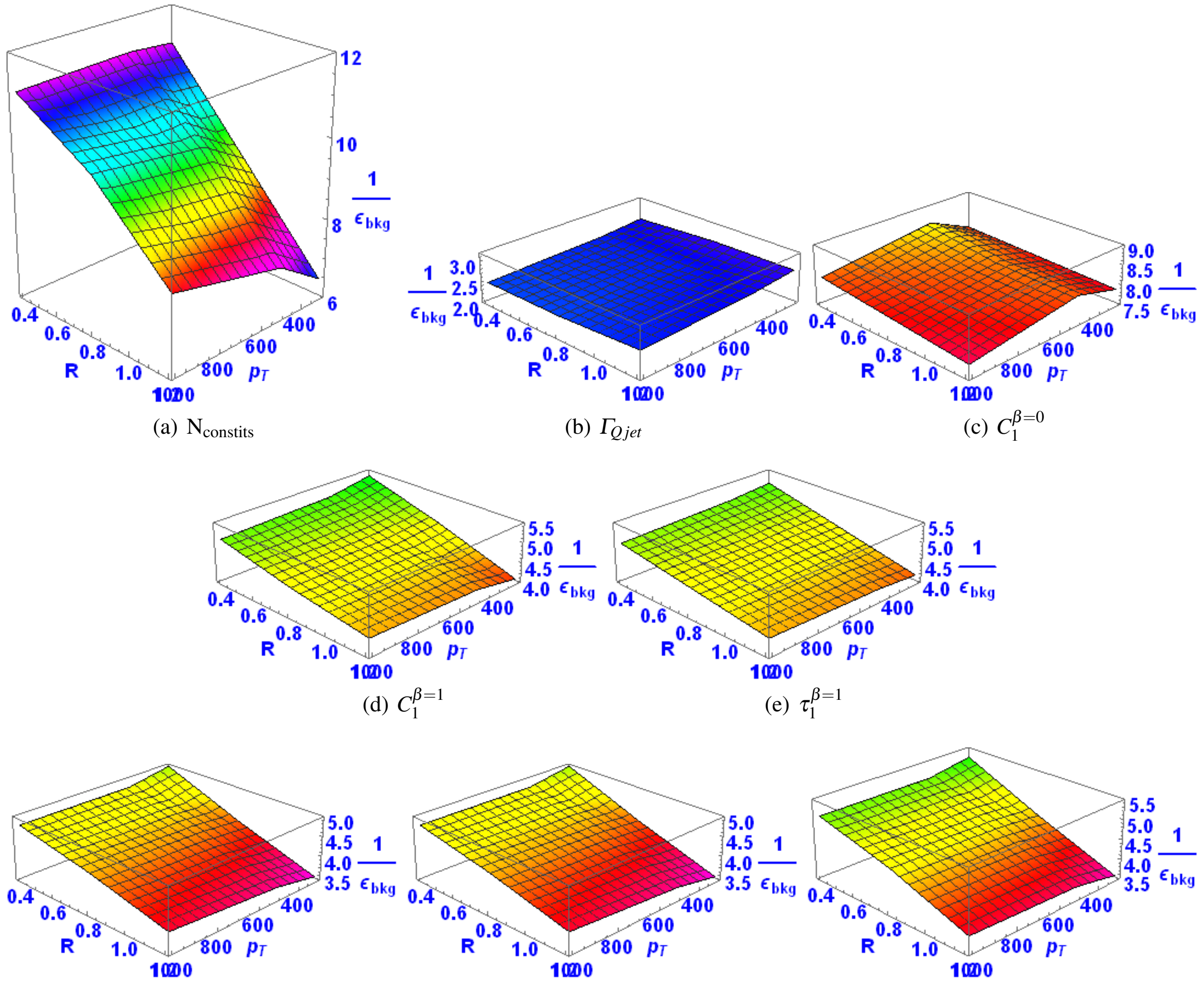

(a) $\mathrm{N}_{\mathrm{constits}}$ (b) Γ_{Qjet} (c) $C_1^{\beta=0}$

(d) $C_1^{\beta=1}$ (e) $\tau_1^{\beta=1}$

(f) $C_1^{\beta=2}$ (g) $\tau_1^{\beta=2}$ (h) Ungroomed mass

Fig. 3 Surface plots of $1/\varepsilon_{\mathrm{bkg}}$ for all single variables considered for quark-gluon discrimination as functions of R and p_T.

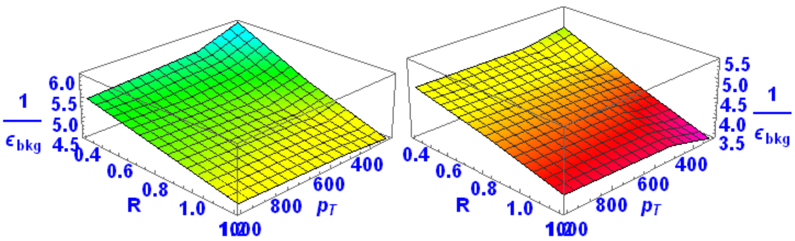

(a) $C_1^{\beta=1}+\tau_1^{\beta=1}$ (b) $C_1^{\beta=2}+\tau_1^{\beta=2}$

Fig. 4 Surface plots of $1/\varepsilon_{\mathrm{bkg}}$ for the indicated pairs of variables from Classes IV and V considered for quark-gluon discrimination as functions of R and p_T.

provement in the rejection rate of about 10% (0.5 out of 5) with essentially no change in the R and p_T dependence, while combining $C_1^{\beta=2}+\tau_1^{\beta=2}$ yields a rejection rate that is essentially identical to the single observable rejection rate for all R and p_T values (with a similar conclusion if one of these observables is replaced with the ungroomed jet mass m). This again confirms that expectation that the observables within a single class effectively probe the *same* jet properties.

Next we consider the cross-class pairs of observables indicated in Figure 5, where only one member of Classes IV and V is included. As expected the largest rejection rates are obtained from combining another observable with $\mathrm{N}_{\mathrm{constits}}$ (Figures 5(a) to (d)). In general, the rates are larger than

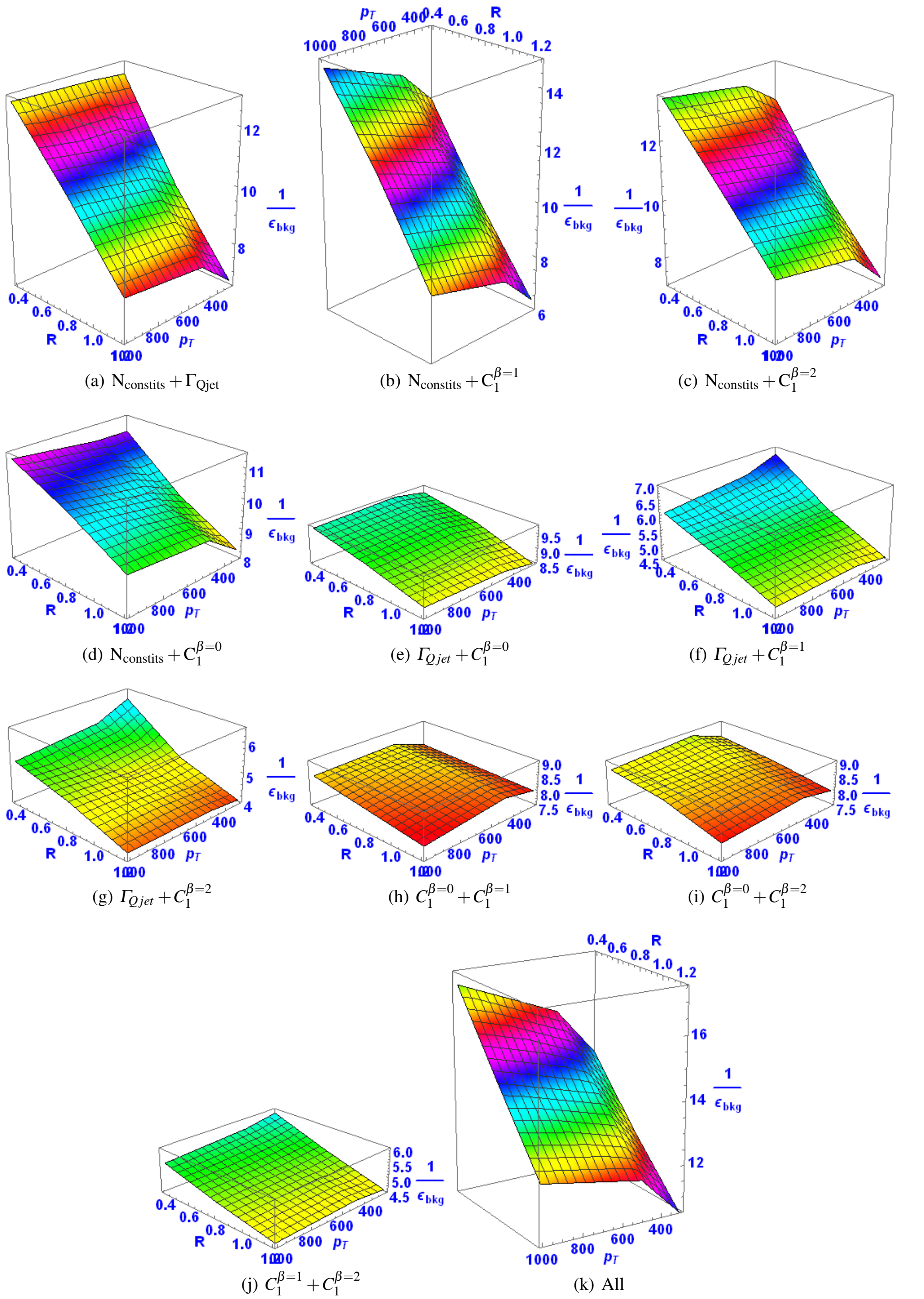

Fig. 5 Surface plots of $1/\varepsilon_{\mathrm{bkg}}$ for the indicated pairs of variables from different classes considered for quark-gluon discrimination as functions of R and p_T.

for the single variable case with similar R and p_T dependence. In particular, the pair $\mathrm{N_{constits}} + \mathrm{C}_1^{\beta=1}$ yields rejection rates in the range 6.4 to 14.7 (6.4 to 15 for the similar case $\mathrm{N_{constits}} + \tau_1^{\beta=1}$) with the largest values at small R and large p_T. The other pairings with $\mathrm{N_{constits}}$ (except with $\tau_1^{\beta=1}$) yield smaller rejection rates and smaller dynamic range. The pair $\mathrm{N_{constits}} + \mathrm{C}_1^{\beta=0}$ (Figure 5(d)) exhibits the smallest range of rates (8.3 to 11.3) suggesting that the differences between these two observables serve to substantially reduce the R and p_T dependence for the pair, but this also reduces the possible optimization. The other pairs indicated exhibit similar behavior. The pair rejection rates are somewhat better than either observable alone (since we are always combining from different classes), and the R and p_T dependence is generally similar to the more variant single observable case. The smallest R and p_T variation always occurs when pairing with $C_1^{\beta=0}$. Changing any of the observables in these pairs with a different observable in the same class (*e.g.*, $C_1^{\beta=2}$ for $\tau_1^{\beta=2}$ produces very similar results (at the few percent level). Figure 5(k) shows the result of a BDT analysis including all of the current observables with rejection rates in the range 10.5 to 17.1. This is a somewhat narrower range than in Figure 5(b) but with somewhat larger maximum values.

Another way to present the same data but by fixing R and p_T and showing all single observables and pairs of observables at once is in terms of the "matrices" indicated in Figures 6 and 7. The numbers in each cell are the now familiar rejection factor values of $1/\varepsilon_{\mathrm{bkg}}$ (gluons) for $\varepsilon_{\mathrm{sig}} = 50\,\%$ (quarks). Figure 6 corresponds $p_T = 1 - 1.1$ TeV and $R = 0.4, 0.8, 1.2$, while Figure 7 is for $R = 0.4$ and the 3 p_T bins. The actual numbers should be familiar from the discussion above with the single observable rejections rates appearing on the diagonal and the pairwise results off the diagonal. The correlations indicated by the shading should be largely understood as indicating the organization of the observables into the now familiar classes. The all-observable (BDT) result appears as the number at the lower right in each plot.

5.4 QCD Jet Masses

To close the discussion of the tagging of jets as either quark jets or gluon jets we provide some insight into the behavior of the masses of such QCD jets, both with and without grooming. Recall that, in practice, an identified jet is simply a list of constituents, *i.e.*, objects in the detector. To the extent that the masses of these individual constituents are irrelevant, typically because the detected constituents are relativistic, each constituent has a "well" defined 4-momentum. It follows that the 4-momentum of the jet is simply the sum of the 4-momenta of the constituents and its square is the jet mass squared. We have already seen one set of jet mass distributions in Figure 1(h) for quark and gluon jets found with the anti-k_{T} algorithm with $R = 0.8$ and p_T in the bin 500-600 GeV. If we consider the mass distributions for other kinematic points (other values of R and p_T), we observe considerable variation but that variation can largely be removed by plotting versus the scaled variable $m/p_T/R$. Simply on dimensional grounds we know that jet mass must scale essentially linearly with p_T, with the remaining p_T dependence arising predominantly from the running of the coupling, $\alpha_s(p_T)$. The R dependence is also crudely linear as the mass scales approximately with the largest angular opening between any 2 constituents and that is set by R. The mass distributions for quark and gluon jets versus $m/p_T/R$ for all of our kinematic points are indicated in Figure 8, where we use a logarithmic scale on the y-axis to clearly exhibit the behavior of these distributions over a large dynamic range. We observe that the distributions for the different kinematic points do approximately scale, *i.e.*, the simple arguments above do capture most of the variation with R and p_T. We will consider shortly an explanation of the residual non-scaling.

Several features of Figure 8 can be easily understood. The distributions all cut-off rapidly for $m/p_T/R > 0.5$, which is understood as the precise limit (maximum mass) for a jet composed of just 2 constituents. As expected from the soft and collinear singularities in QCD, the mass distribution peaks at small mass values. The actual peak is "pushed" away from the origin by the so-called Sudakov form factor. Summing the corresponding logarithmic structure (singular in both p_T and angle) to all orders in perturbation theory yields a distribution that is highly damped as the mass vanishes. In words, there is precisely *zero* probability that a color parton emits *no* radiation (and the resulting jet has zero mass). The large mass "shoulder" ($0.3 < m/p_T/R < 0.5$) is driven largely by the presence of a single large angle, energetic emission in the underlying QCD shower, *i.e.*, this regime is quite well described by low-order perturbation theory. (The shoulder label will be more clear after we groom the jet.) In contrast, we should think of the peak region as corresponding to multiple soft emissions. This simple (approximate) picture provides an understanding of the bulk of the differences between the quark and gluon jet mass distributions. Since the probability of the single large angle, energetic emission is proportional to the color charge, the gluon distribution should be enhanced in this region by a factor of about $C_A/C_F = 9/4$, consistent with what is observed in Figure 8. Similarly the exponent in the Sudakov damping factor for the gluon jet mass distribution is enhanced by the same factor, leading to a peak "pushed" further from the origin. So the gluon jet mass distribution exhibits a larger average jet mass than the quark jet, with a larger relative contribution arising from the perturbative shoulder region. Recall also that the number of constituents in the jet is also larger (on average) for the gluon jet simply because a gluon

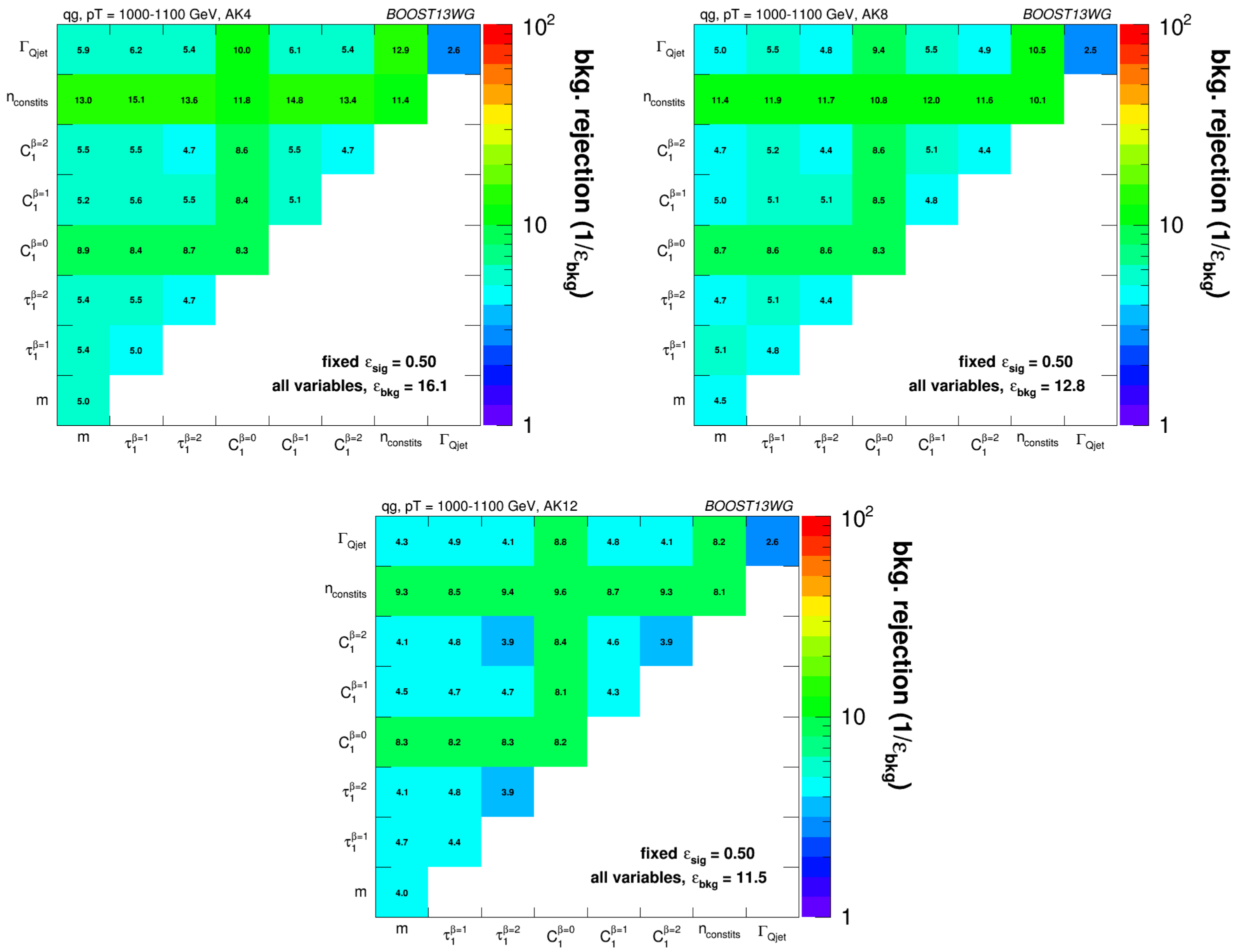

Fig. 6 Gluon rejection defined as $1/\varepsilon_{\text{gluon}}$ when using each 2-variable combination as a tagger with 50% acceptance for quark jets. Results are shown for jets with $p_T = 1-1.1$ TeV and for (top left) $R = 0.4$; (top right) $R = 0.8$; (bottom) $R = 1.2$. The rejection obtained with a tagger that uses all variables is also shown in the plots.

will radiate more than a quark. These features explain much of what we observed earlier in terms of the effectiveness of the various observable to separate quark jets from gluons jets. Note in particular that the enhanced role of the shoulder for gluon jet explains, at least qualitatively, the difference in the distributions for the observable Γ_{Qjet}. Since the shoulder is dominated by a single large angle, hard emission, ii is minimally impacted by pruning, which removes the large angle, *soft* constituents (as illustrated just below). Thus jets in the shoulder exhibit small volatility and they are a larger component in the gluon jet distribution. Hence gluon jets, on average, have smaller values of Γ_{Qjet} than quark jets as in Figure 1(b). Further this feature of gluon jets is distinct from fact that there are more constituents, which explains why Γ_{Qjet} and N$_{\text{constits}}$ supply largely independent information for distinguishing quark and gluon jets.

To illustrate some of these points in more detail, Figure 9 exhibits the jet mass distributions (of Figure 8) *after pruning*[34, 47]. Removing the large angle, soft constituents moves the peak in both of the distributions from $m/p_T/R \sim 0.1-0.2$ to the region around $m/p_T/R \sim 0.05$. This explains why pruning works to reduce the QCD background when looking for a signal in a specific jet mass bin. The "shoulder" feature is much more apparent after pruning, as is the larger shoulder for the gluon jets.

Our final topic is the residual R and p_T dependence exhibited in Figures 8 and 9, where we are using the scaled variable $m/p_T/R$. As already suggested, the residual p_T dependence can be understood as arising primarily from the slow decrease of the strong coupling $\alpha_s(p_T)$ as p_T increases. This will lead to a corresponding decrease in the (largely perturbative) shoulder regime for both distributions as p_T increases. At the same time, and for the same reason, the Sudakov damping is less strong with increasing p_T and the peak moves towards the origin. Thus the overall impact of increasing p_T for both distributions is a (slow) shift to smaller values of $m/p_T/R$. This is just what is observed in Figures 8 and 9, although the numerical size of the effect is reduced in

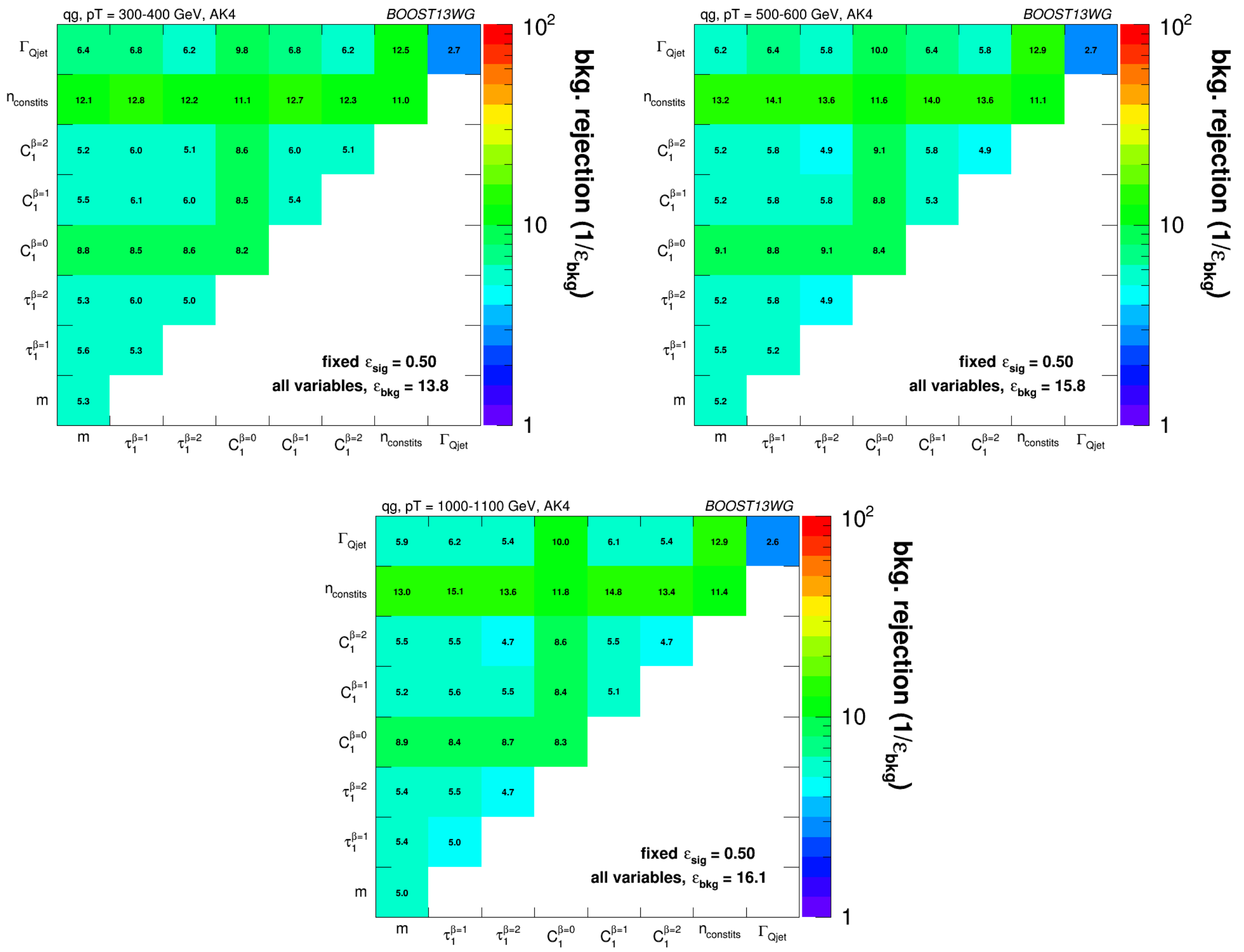

Fig. 7 Gluon rejection defined as $1/\varepsilon_{\text{gluon}}$ when using each 2-variable combination as a tagger with 50% acceptance for quark jets. Results are shown for R=0.4 jets with (top left) $p_T = 300-400$ GeV, (top right) $p_T = 500-600$ GeV and (bottom) $p_T = 1-1.1$ TeV. The rejection obtained with a tagger that uses all variables is also shown in the plots.

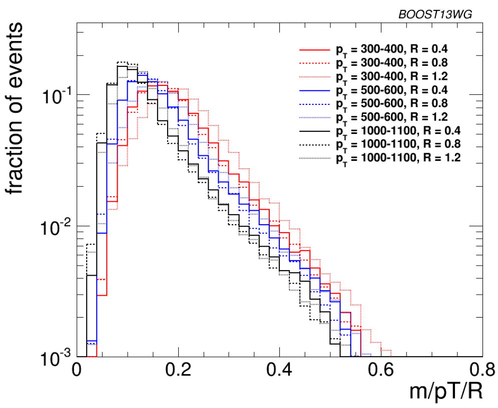

(a) Quark jets

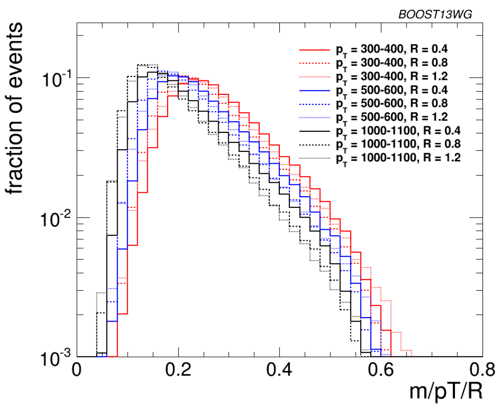

(b) Gluon jets

Fig. 8 Comparisons of quark and gluon ungroomed mass distributions versus the scaled variable $m/p_T/R$.

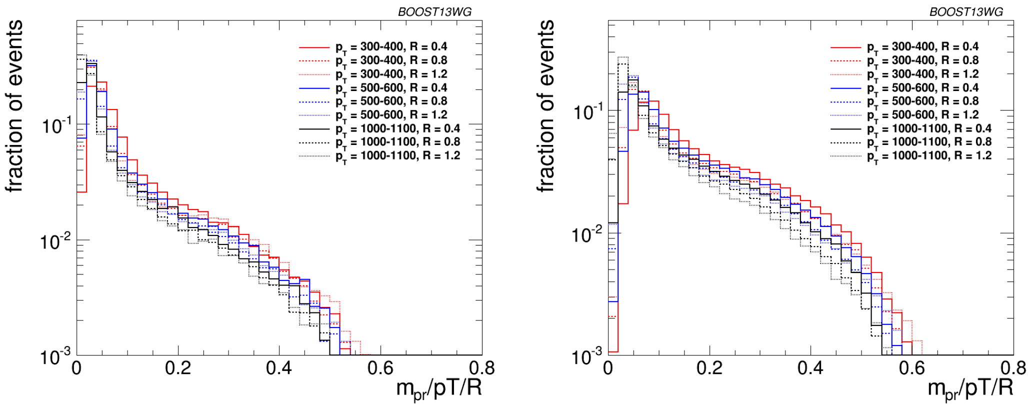

(a) Quark jets (b) Gluon jets

Fig. 9 Comparisons of quark and gluon pruned mass distributions versus the scaled variable $m_{\mathrm{pr}}/p_T/R$.

the pruned case. The R dependence is more complicated as there are effectively three different contributions to the mass distribution. The perturbative large angle, energetic single emission contribution largely scales in the variable $m/p_T/R$, which is why we see little residual R dependence in either figure for $m/p_T/R > 0.4$. The large angle soft emissions can both contribute at mass values that scale like R and increase in number as R increases (*i.e.*, as the area of the jet grows as R^2). Such contributions can yield a distribution that moves to the right as R increases and presumably explain the behavior at small p_T in Figure 8. Since pruning largely removes this contribution, we observe no such behavior in Figure 9. The contribution of small angle, soft emissions will be at fixed m values and thus shift to the left versus the scaled variable as R increases. This presumably explains the small shifts in this direction observed in both figures.

5.5 Conclusions

In Section 5 we have seen that a variety of jet observables provide information about the jet that can be employed effectively to separately tag quark and gluon jets. Further, when used in combination, these observables can provide even better separation. We saw that the best performing single observable is simply the number of constituents in the jet, N_{constits}, while the largest further improvement comes from combining with $C_1^{\beta=1}$ (or $\tau_1^{\beta=1}$), but the smallest R and p_T dependence arises from combining with $C_1^{\beta=0}$. On the other hand, some of the commonly used observables are highly correlated and do not provide extra information and enhanced tagging when used together. We have both demonstrated these correlations and provided a discussion of the physics behind the structure of the correlation. In particular, using the jet mass as a specific example observable we have tried to explicitly explain the differences between jets initiated by both quarks and gluons.

6 Boosted W-Tagging

In this section, we study the discrimination of a boosted hadronically decaying W signal against a gluon background, comparing the performance of various groomed jet masses, substructure variables, and BDT combinations of groomed mass and substructure. We produce ROC curves that elucidate the performance of the various groomed mass and substructure variables. A range of different distance parameters R for the anti-k_T jet algorithm are explored, as well as a variety of kinematic regimes (lead jet p_T 300-400 GeV, 500-600 GeV, 1.0-1.1 TeV). This allows us to determine the performance of observables as a function of jet radius and jet boost, and to see where different approaches may break down. The groomed mass and substructure variables are then combined in a BDT as described in Section 4, and the performance of the resulting BDT discriminant explored through ROC curves to understand the degree to which variables are correlated, and how this changes with jet boost and jet radius.

6.1 Methodology

These studies use the WW samples as signal and the dijet gg as background, described previously in Section 2. Whilst only gluonic backgrounds are explored here, the conclusions as to the dependence of the performance and correlations on the jet boost and radius have been verified to hold also for qq backgrounds. **ED: To be checked!**

As in the q/g tagging studies, the showered events were clustered with FASTJET 3.03 using the anti-k_{T} algorithm with jet radii of $R = 0.4, 0.8, 1.2$. In both signal and background samples, an upper and lower cut on the leading jet p_T is applied after showering/clustering, to ensure similar p_T spectra for signal and background in each p_T bin. The bins in leading jet p_T that are considered are 300-400 GeV, 500-600 GeV, 1.0-1.1 TeV, for the 300-400 GeV, 500-600 GeV, 1.0-1.1 TeV parton p_T slices respectively. The jets then have various grooming approaches applied and substructure observables reconstructed as described in Section 3.4. The substructure observables studied in this section are:

- The ungroomed, trimmed (m_{trim}), and pruned (m_{prun}) jet masses.
- The mass output from the modified mass drop tagger (m_{mmdt}).
- The soft drop mass with $\beta = -1, 2$ (m_{sd}).
- 2-point energy correlation function ratio $C_2^{\beta=1}$ (we also studied $\beta = 2$ but do not show its results because it showed poor discrimination power).
- N-subjettiness ratio τ_2/τ_1 with $\beta = 1$ ($\tau_{21}^{\beta=1}$) and with axes computed using one-pass k_t axis optimization (we also studied $\beta = 2$ but did not show its results because it showed poor discrimination power).
- The pruned Qjet mass volatility, Γ_{Qjet}.

6.2 Single Variable Performance

In this section we will explore the performance of the various groomed jet mass and substructure variables in terms of discriminating signal and background. Since we have not attempted to optimise the grooming parameter settings of each grooming algorithm, we do not want to place too much emphasis here on the relative performance of the groomed masses, but instead concentrate on how their performance changes depending on the kinematic bin and jet radius considered.

Figure 10 the compares the signal and background in terms of the different groomed masses explored for the anti-k_{T} R=0.8 algorithm in the p_T 500-600 bin. One can clearly see that in terms of separating signal and background the groomed masses will be significantly more performant than the ungroomed anti-k_{T} R=0.8 mass. Figure 11 compares signal and background in the different substructure variables explored for the same jet radius and kinematic bin.

Figures 12, 13 and 14 show the single variable ROC curves compared to the ROC curve for a BDT combination of all the variables (labelled “allvars”), for each of the anti-k_{T} distance parameters considered in each of the kinematic bins. One can see that, in all cases, the “allvars” option is considerably better performant than any of the individual single variables considered, indicating that there is considerable complementarity between the variables, and this will be explored further in the next section.

Although the ROC curves give all the relevant information, it is hard to compare performance quantitatively. In Figures 15, 16 and 17 are shown matrices which give the background rejection for a signal efficiency of 70% when two variables (that on the x-axis and that on the y-axis) are combined in a BDT. These are shown separately for each p_T bin and jet radius considered. In the final column of these plots are shown the background rejection performance for three-variable BDT combinations of $m_{sd}^{\beta=2} + C_2^{\beta=1} + X$. These results will be discussed later in Section 6.3.3. The diagonal of these plots correspond to the background rejections for a single variable BDT, and can thus be examined to get a quantitative measure of the individual single variable performance, and to study how this changes with jet radius and momenta.

One can see that in general the most performant single variables are the groomed masses. However, in certain kinematic bins and for certain jet radii, $C_2^{\beta=1}$ has a background rejection that is comparable to or better than the groomed masses.

By comparing Figures 15(a), 16(a) and 17(b), we can see how the background rejection performance evolves as we increase momenta whilst keeping the jet radius fixed to R=0.8. Similarly, by comparing Figures 15(b), 16(b) and 17(c) we can see how performance evolves with p_T for R=1.2. For both R=0.8 and R=1.2 the background rejection power of the groomed masses increases with increasing p_T, with a factor 1.5-2.5 increase in rejection in going from the 300-400 GeV to 1.0-1.1 TeV bins. **ED: Add some of the 1-D plots comparing signal and bkgd in the different masses and pT bins here?** However, the $C_2^{\beta=1}$, Γ_{Qjet} and $\tau_{21}^{\beta=1}$ substructure variables behave somewhat differently. The background rejection power of the Γ_{Qjet} and $\tau_{21}^{\beta=1}$ variables both decrease with increasing p_T, by up to a factor two in going from the 300-400 GeV to 1.0-1.1 TeV bins. Conversely the rejection power of $C_2^{\beta=1}$ dramatically increases with increasing p_T for R=0.8, but does not improve with p_T for the larger jet radius R=1.2. **ED: Can we explain this? Again, should we add some of the 1-D plots?**

By comparing the individual sub-figures of Figures 15, 16 and 17 we can see how the background rejection performance depends on jet radius within the same p_T bin. To within $\sim 25\%$, the background rejection power of the groomed masses remains constant with respect to the jet radius. However, we again see rather different behaviour for the substructure variables. In all p_T bins considered the most performant substructure variable, $C_2^{\beta=1}$, performs best for an anti-k_{T} distance parameter of R=0.8. The performance of this variable is dramatically worse for the larger jet radius of R=1.2 (a factor seven worse background rejection in the 1.0-1.1 TeV bin), and substantially worse for R=0.4. For the other jet substructure variables considered, Γ_{Qjet} and $\tau_{21}^{\beta=1}$,

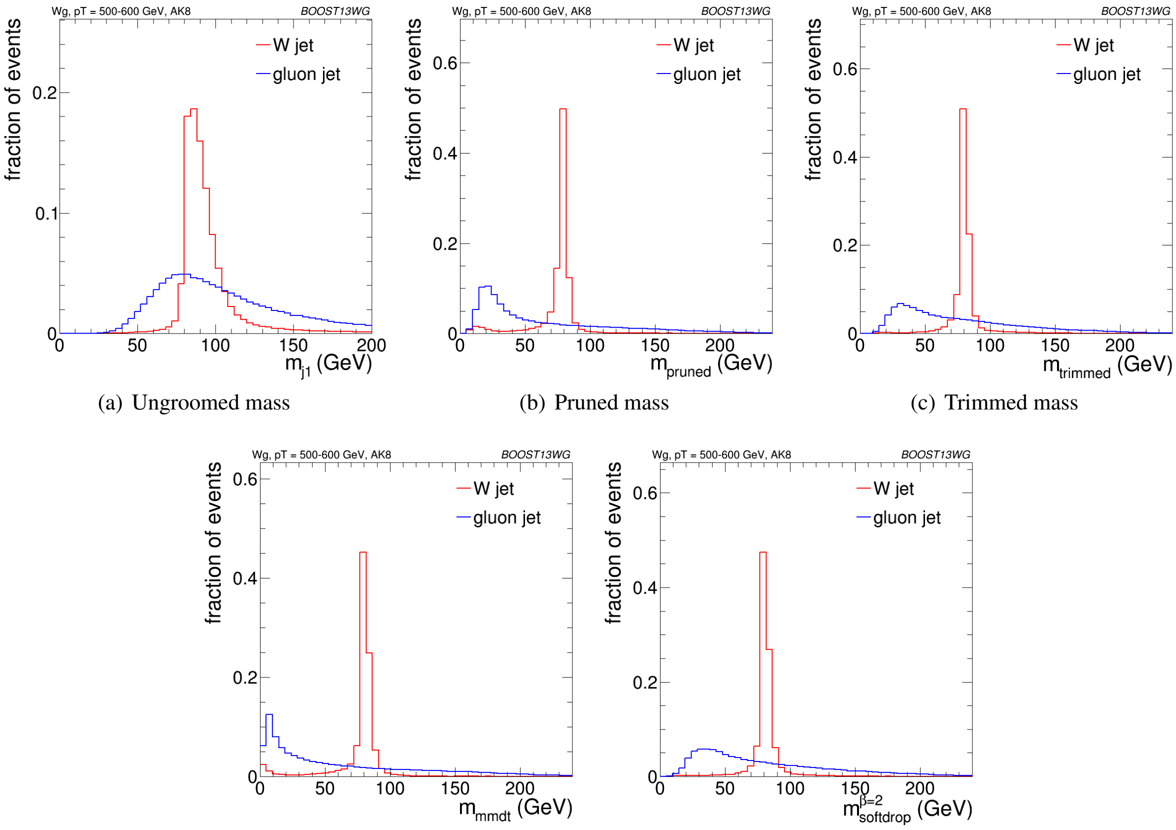

(a) Ungroomed mass (b) Pruned mass (c) Trimmed mass

(d) mMDT mass (e) Soft-drop $\beta = 2$ mass

Fig. 10 Comparisons of the QCD background to the WW signal in the p_T 500-600 GeV bin using the anti-k_T R=0.8 algorithm: leading jet mass distributions.

their background rejection power also reduces for larger jet radius, but not to the same extent. **ED: Insert some nice discussion/explanation of why jet substructure power generally gets worse as we go to large jet radius, but groomed mass performance does not. Probably need the 1-D figures for this.**

6.3 Combined Performance

The off-diagonal entries in Figures 15, 16 and 17 can be used to compare the performance of different BDT two-variable combinations, and see how this varies as a function of p_T and R. By comparing the background rejection achieved for the two-variable combinations to the background rejection of the "all variables" BDT, one can understand how much more discrimination is possible by adding further variables to the two-variable BDTs.

One can see that in general the most powerful two-variable combinations involve a groomed mass and a non-mass substructure variable ($C_2^{\beta=1}$, Γ_{Qjet} or $\tau_{21}^{\beta=1}$). Two-variable combinations of the substructure variables are not powerful in comparison. Which particular mass + substructure variable combination is the most powerful depends strongly on the p_T and R of the jet, as discussed in the sections that follow.

There is also modest improvement in the background rejection when different groomed masses are combined, compared to the single variable groomed mass performance, indicating that there is complementary information between the different groomed masses. In addition, there is an improvement in the background rejection when the groomed masses are combined with the ungroomed mass, indicating that grooming removes some useful discriminatory information from the jet. These observations are explored further in the section below.

Generally one can see that the R=0.8 jets offer the best two-variable combined performance in all p_T bins explored here. This is despite the fact that in the highest 1.0-1.1 GeV p_T bin the average separation of the quarks from the W decay is much smaller than 0.8, and well within 0.4. This conclusion could of course be susceptible to pile-up, which is not considered in this study.

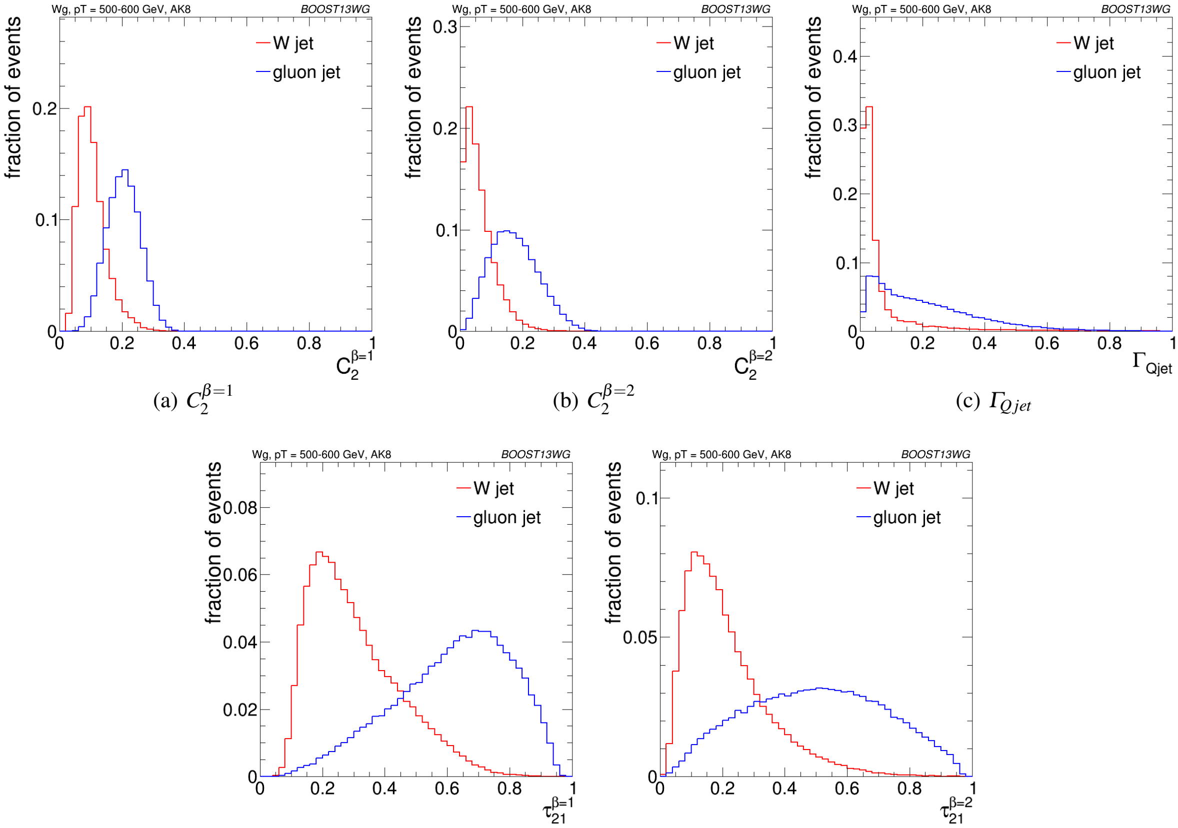

(a) $C_2^{\beta=1}$ (b) $C_2^{\beta=2}$ (c) Γ_{Qjet}

(d) $\tau_{21}^{\beta=1}$ (e) $\tau_{21}^{\beta=2}$

Fig. 11 Comparisons of the QCD background to the WW signal in the p_T 500-600 GeV bin using the anti-k_{T} R=0.8 algorithm: substructure variables.

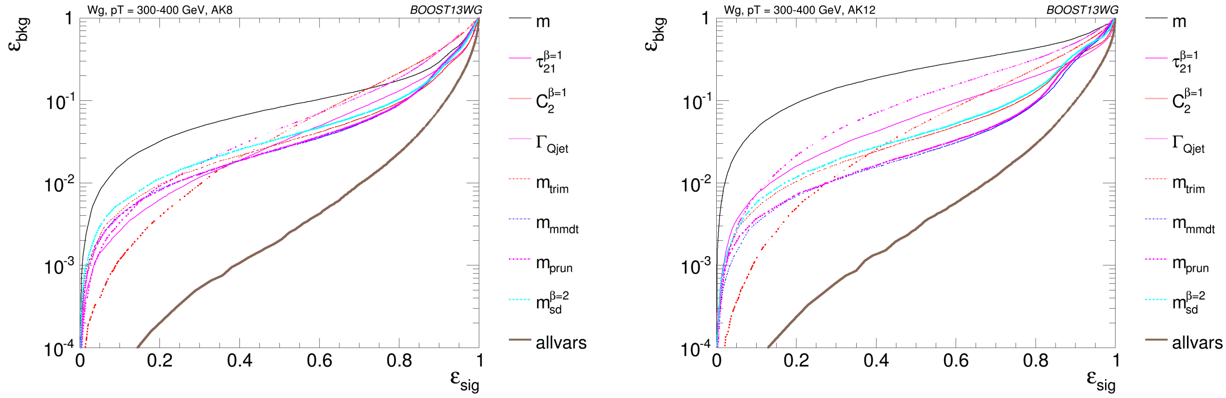

(a) anti-k_{T} R=0.8, p_T 300-400 GeV bin (b) anti-k_{T} R=1.2, p_T 300-400 GeV bin

Fig. 12 The ROC curve for all single variables considered for W tagging in the p_T 300-400 GeV bin using the anti-k_{T} R=0.8 algorithm and R=1.2 algorithm.

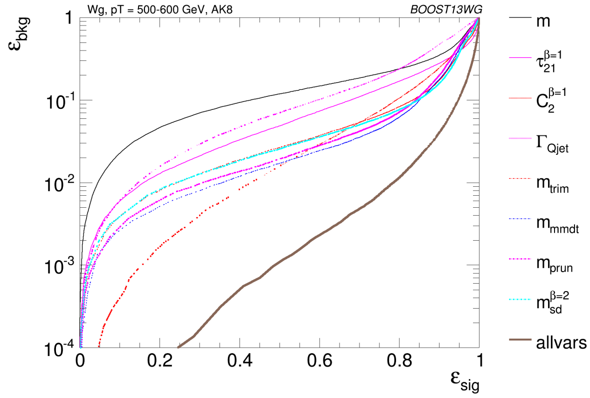

(a) anti-k_T R=0.8, p_T 500-600 GeV bin

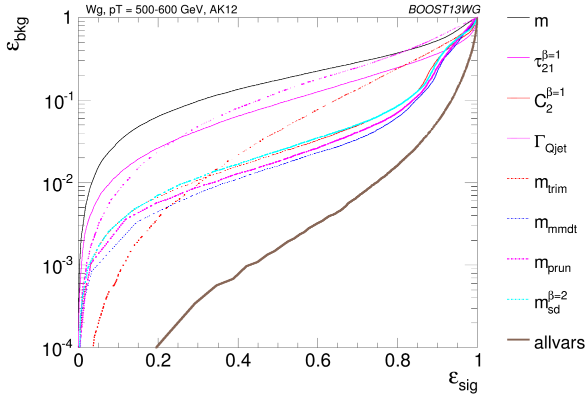

(b) anti-k_T R=1.2, p_T 500-600 GeV bin

Fig. 13 The ROC curve for all single variables considered for W tagging in the p_T 500-600 GeV bin using the anti-k_T R=0.8 algorithm and R=1.2 algorithm.

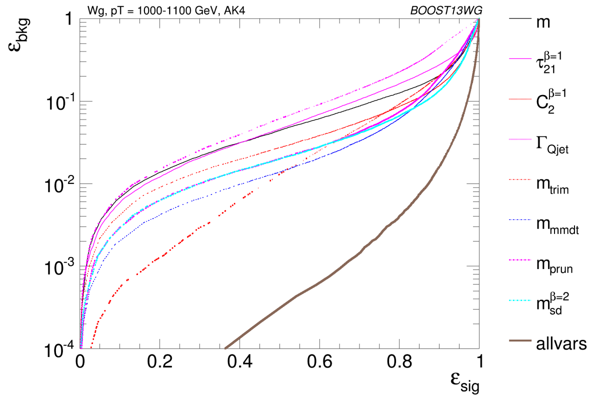

(a) anti-k_T R=0.4, p_T 1.0-1.1 TeV bin

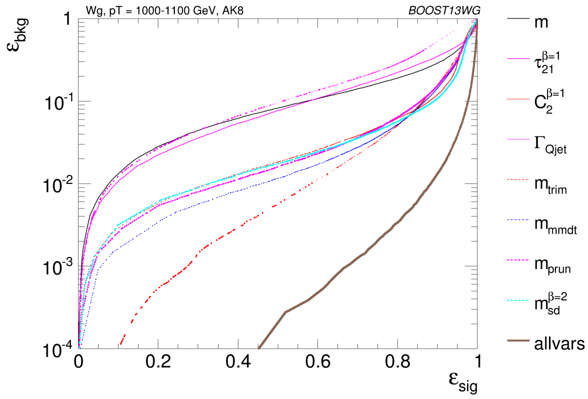

(b) anti-k_T R=0.8, p_T 1.0-1.1 TeV bin

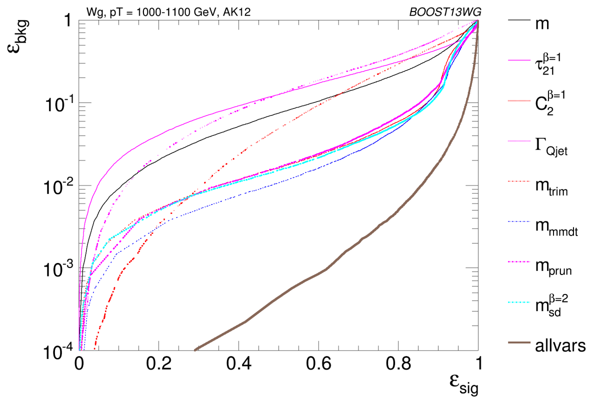

(c) anti-k_T R=1.2, p_T 1.0-1.1 TeV bin

Fig. 14 The ROC curve for all single variables considered for W tagging in the p_T 1.0-1.1 TeV bin using the anti-k_T R=0.4 algorithm, anti-k_T R=0.8 algorithm and R=1.2 algorithm.

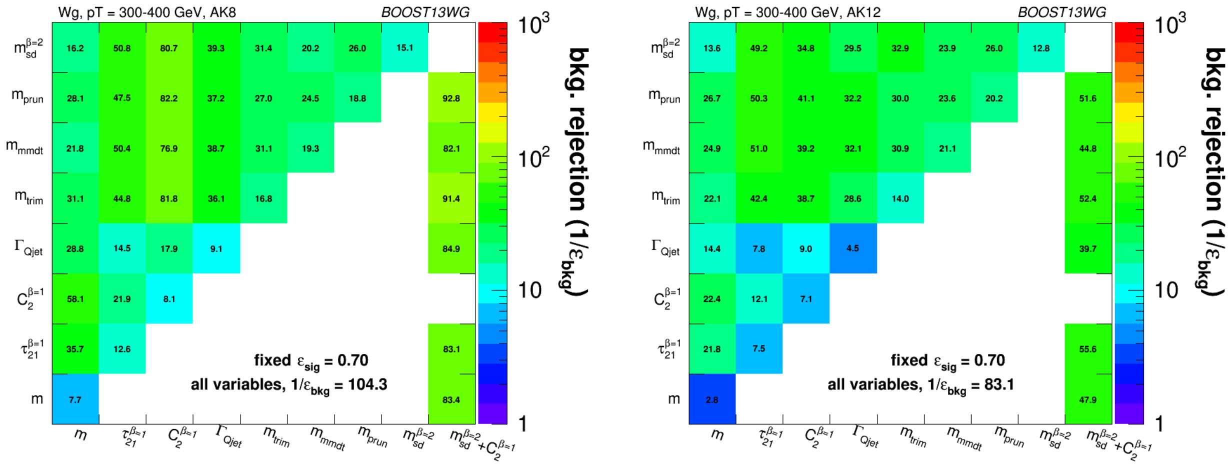

(a) anti-k_T R=0.8, p_T 300-400 GeV bin

(b) anti-k_T R=1.2, p_T 300-400 GeV bin

Fig. 15 The background rejection for a fixed signal efficiency (70%) of each BDT combination of each pair of variables considered, in the p_T 300-400 GeV bin using the anti-k_T R=0.8 algorithm and R=1.2 algorithm. Also shown is the background rejection for a BDT combination of all of the variables considered.

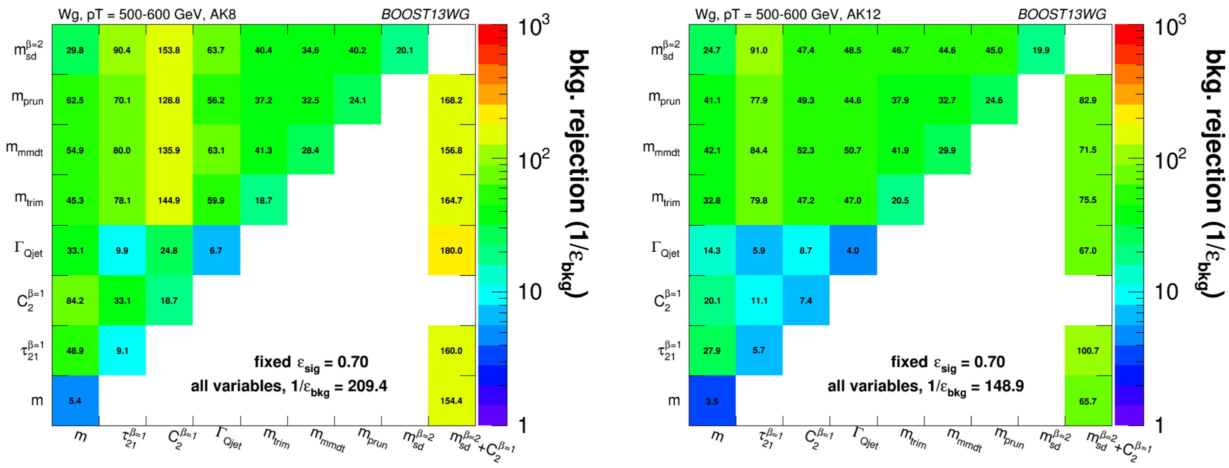

(a) anti-k_T R=0.8, p_T 500-600 GeV bin

(b) anti-k_T R=1.2, p_T 500-600 GeV bin

Fig. 16 The background rejection for a fixed signal efficiency (70%) of each BDT combination of each pair of variables considered, in the p_T 500-600 GeV bin using the anti-k_T R=0.8 algorithm and R=1.2 algorithm. Also shown is the background rejection for a BDT combination of all of the variables considered.

6.3.1 Mass + Substructure Performance

As already noted, the largest background rejection at 70% signal efficiency are in general achieved using those two variable BDT combinations which involve a groomed mass and a non-mass substructure variable. For both R=0.8 and R=1.2 jets, the rejection power of these two variable combinations increases substantially with increasing p_T , at least within the p_T range considered here.

For a jet radius of R=0.8, across the full p_T range considered, the groomed mass + substructure variable combinations with the largest background rejection are those which involve $C_2^{\beta=1}$. For example, in combination with $m_{sd}^{\beta=2}$, this produces a five-, eight- and fifteen-fold increase in background rejection compared to using the groomed mass alone. In Figure 18 the low degree of correlation between $m_{sd}^{\beta=2}$ versus $C_2^{\beta=1}$ that leads to these large improvements in background rejection can be seen. One can also see that what little correlation exists is rather non-linear in nature, changing from a negative to a positive correlation as a function of the groomed mass, something which helps to improve the background rejection in the region of the W mass peak.

However, when we switch to a jet radius of R=1.2 the picture for $C_2^{\beta=1}$ combinations changes dramatically. These

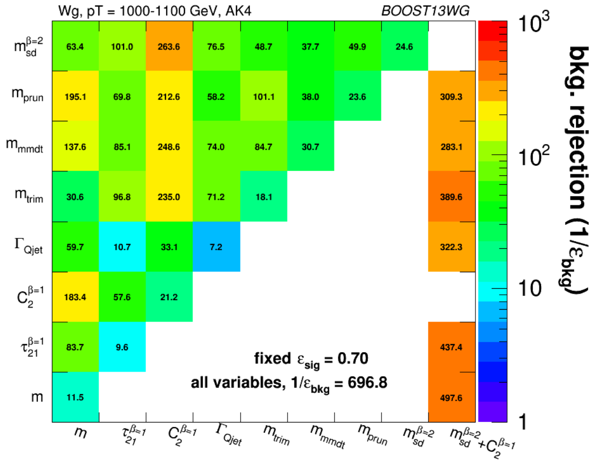

(a) anti-k_{T} R=0.4, p_T 1.0-1.1 TeV bin

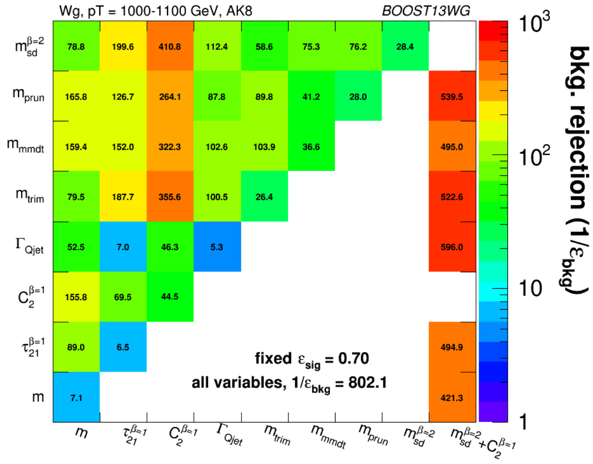

(b) anti-k_{T} R=0.8, p_T 1.0-1.1 TeV bin

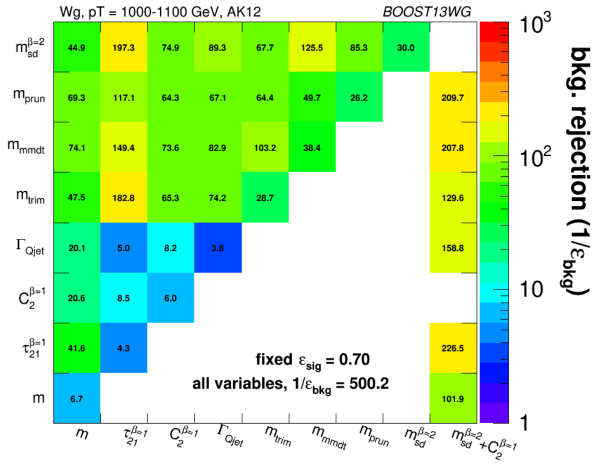

(c) anti-k_{T} R=1.2, p_T 1.0-1.1 TeV bin

Fig. 17 The background rejection for a fixed signal efficiency (70%) of each BDT combination of each pair of variables considered, in the p_T 1.0-1.1 TeV bin using the anti-k_{T} R=0.4, R=0.8 and R=1.2 algorithm. Also shown is the background rejection for a BDT combination of all of the variables considered.

become significantly less powerful, and the most powerful variable in groomed mass combinations becomes $\tau_{21}^{\beta=1}$ for all jet p_T considered. Figure 19 shows the correlation between $m_{sd}^{\beta=2}$ and $C_2^{\beta=1}$ in the p_T 1.0 - 1.2 TeV bin for the various jet radii considered. Figure 20 is the equivalent set of distributions for $m_{sd}^{\beta=2}$ and $\tau_{21}^{\beta=1}$. One can see from Figure 19 that, due to the sensitivity of the observable to to soft, wide-angle radiation, as the jet radius increases $C_2^{\beta=1}$ increases and becomes more and more smeared out for both signal and background, leading to worse discrimination power. This does not happen to the same extent for $\tau_{21}^{\beta=1}$. We can see from Figure 20 that the negative correlation between $m_{sd}^{\beta=2}$ and $\tau_{21}^{\beta=1}$ that is clearly visible for R=0.4 decreases for larger jet radius, such that the groomed mass and substructure variable are far less correlated and $\tau_{21}^{\beta=1}$ offers improved discrimination within a $m_{sd}^{\beta=2}$ mass window.

6.3.2 Mass + Mass Performance

The different groomed masses and the ungroomed mass are of course not fully correlated, and thus one can always see some kind of improvement in the background rejection (relative to the single mass performance) when two different mass variables are combined in the BDT. However, in some cases the improvement can be dramatic, particularly at higher p_T, and particularly for combinations with the ungroomed mass. For example, in Figure 17 we can see that in the p_T 1.0-1.1 TeV bin the combination of pruned mass with ungroomed mass produces a greater than eight-fold improvement in the background rejection for R=0.4 jets, a greater

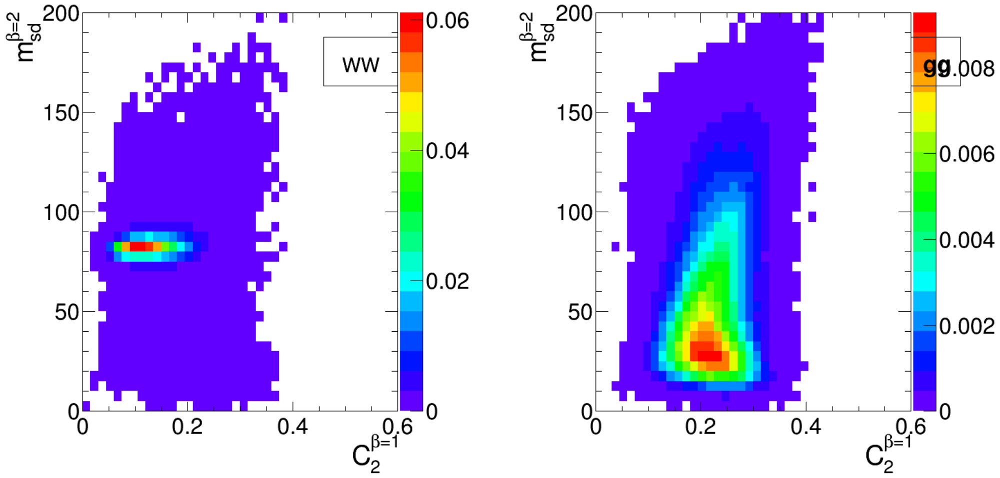

(a) p_T 300-400 GeV

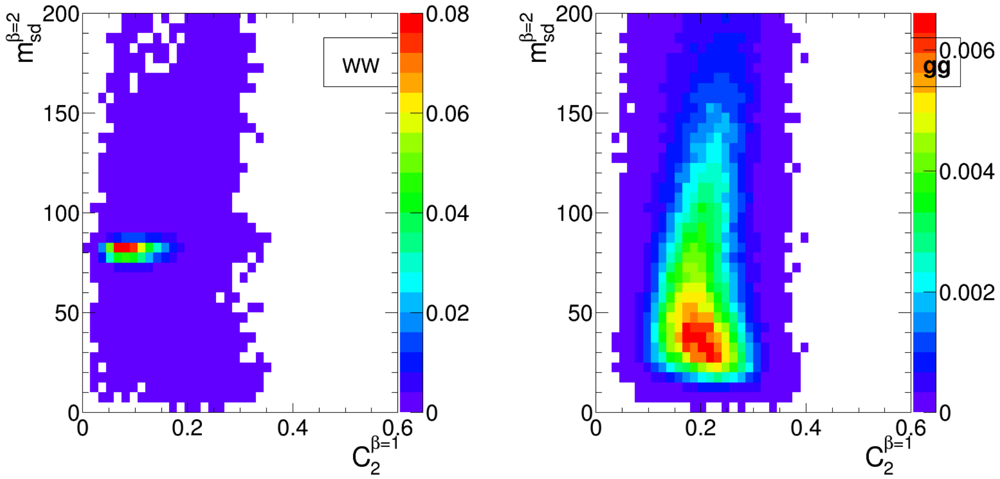

(b) p_T 500-600 GeV

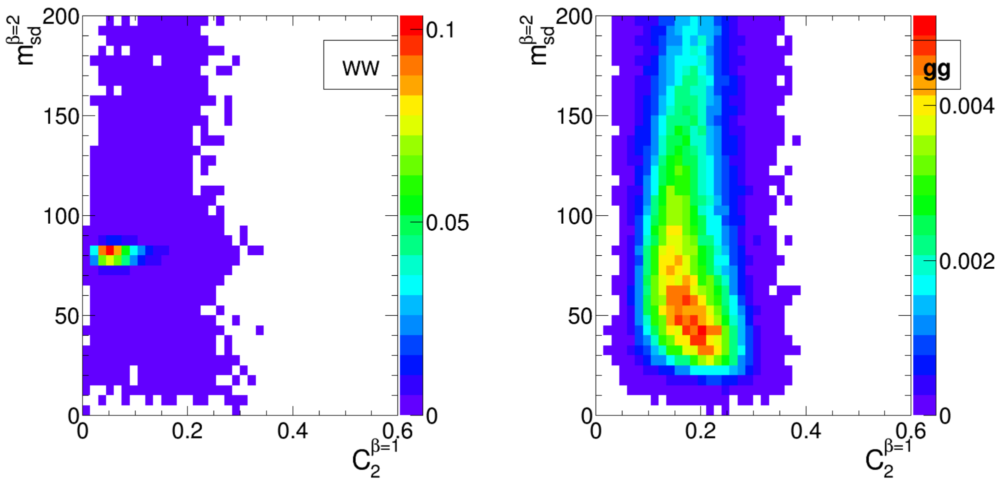

(c) p_T 1.0-1.1 TeV

Fig. 18 2-D plots showing $m_{sd}^{\beta=2}$ versus $C_2^{\beta=1}$ for R=0.8 jets in the various p_T bins considered.

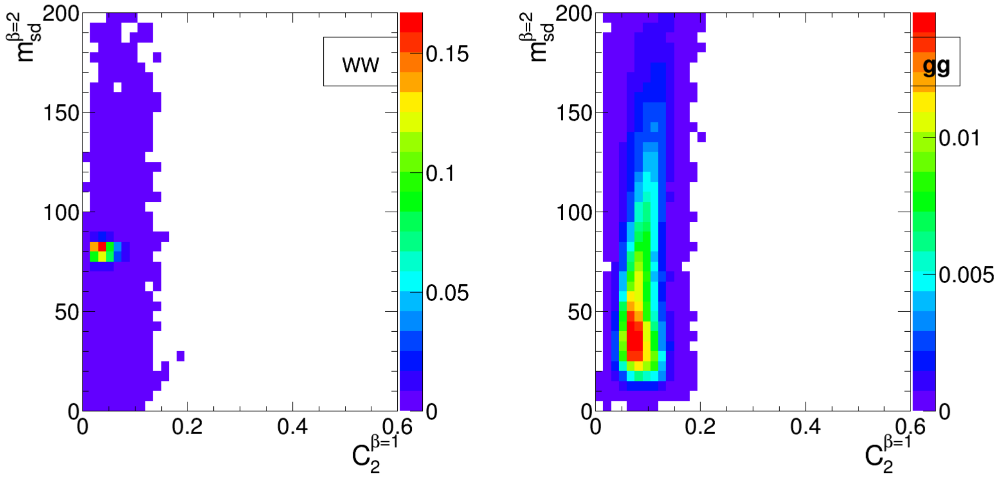

(a) p_T R=0.4

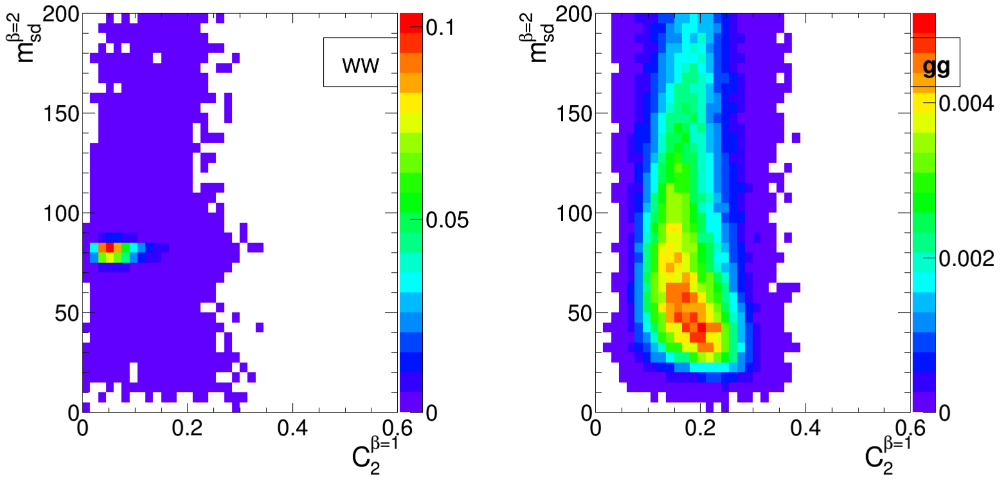

(b) p_T R=0.8

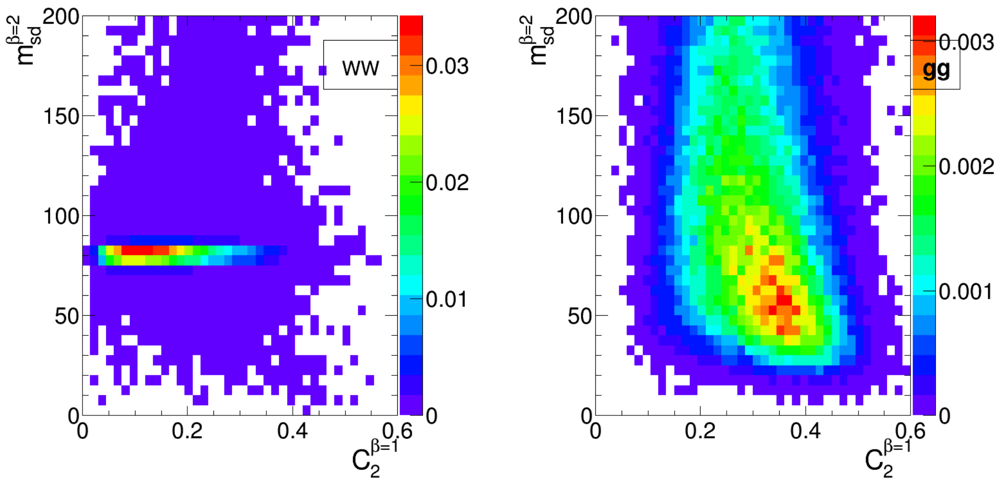

(c) p_T R=1.2

Fig. 19 2-D plots showing $m_{sd}^{\beta=2}$ versus $C_2^{\beta=1}$ for R=0.4, 0.8 and 1.2 jets in the p_T 1.0-1.1 TeV bin.

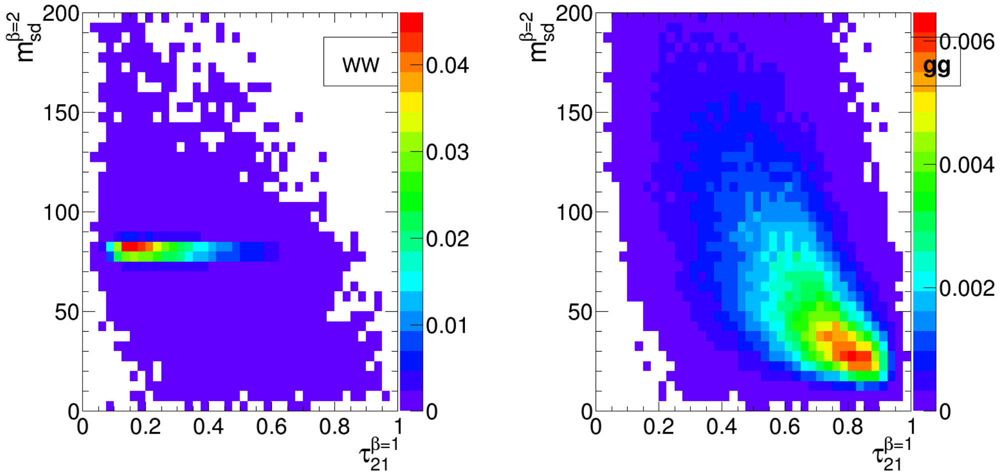

(a) p_T R=0.4

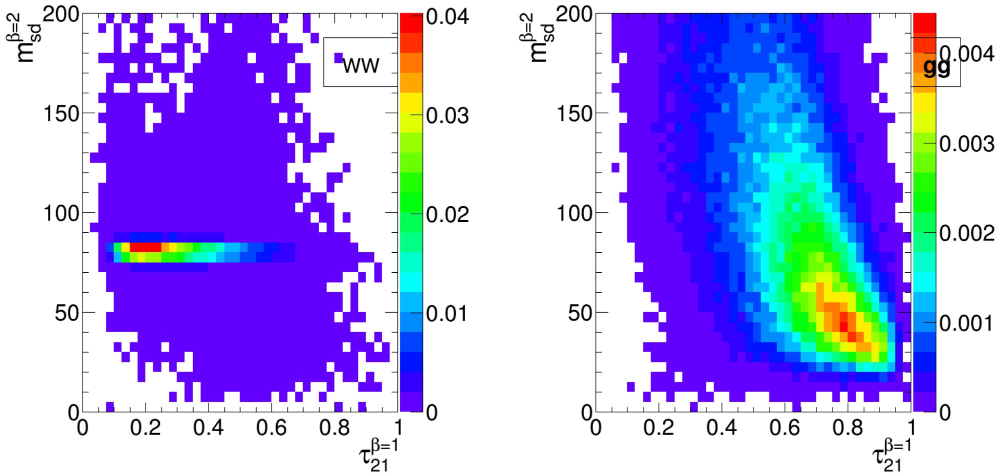

(b) p_T R=0.8

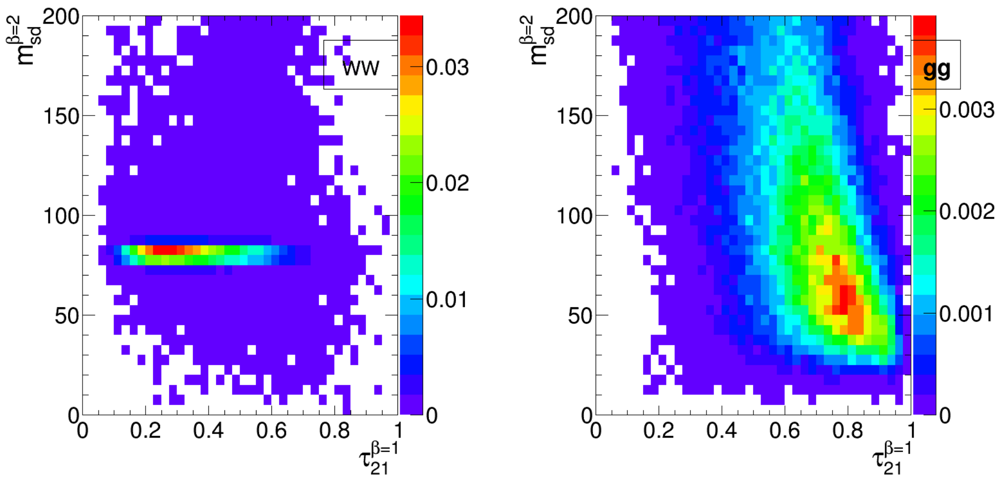

(c) p_T R=1.2

Fig. 20 2-D plots showing $m_{sd}^{\beta=2}$ versus $\tau_{21}^{\beta=1}$ for R=0.4, 0.8 and 1.2 jets in the p_T 1.0-1.1 TeV bin.

than five-fold improvement for R=0.8 jets, and a factor ∼two improvement for R=1.2 jets. A similar behaviour can be seen for mMDT mass. In Figures 21, 22 and 23 is shown the 2-D correlation plots of the pruned mass versus the ungroomed mass separately for the WW signal and gg background samples in the p_T 1.0-1.1 TeV bin, for the various jet radii considered. For comparison, the correlation of the trimmed mass with the ungroomed mass, a combination that does not improve on the single mass as dramatically, is shown. In all cases one can see that there is a much smaller degree of correlation between the pruned mass and the ungroomed mass in the backgrounds sample than for the trimmed mass and the ungroomed mass. This is most obvious in Figure 21, where the high degree of correlation between the trimmed and ungroomed mass is expected, since with the parameters used (in particular $R_{trim} = 0.2$) we cannot expect trimming to have a significant impact on an R=0.4 jet. The reduced correlation with ungroomed mass for pruning in the background means that, once we have made the requirement that the pruned mass is consistent with a W (i.e. ∼80 GeV), a relatively large difference between signal and background in the ungroomed mass still remains, and can be exploited to improve the background rejection further. In other words, many of the background events which pass the pruned mass requirement do so because they are shifted to lower mass (to be within a signal mass window) by the grooming, but these events still have the property that they look very much like background events before the grooming. A single requirement on the groomed mass only does not exploit this. Of course, the impact of pile-up, not considered in this study, could significantly limit the degree to which the ungroomed mass could be used to improve discrimination in this way.

6.3.3 *"All Variables" Performance*

As well as the background rejection at a fixed 70% signal efficiency for two-variable combinations, Figures 15, 16 and 17 also report the background rejection achieved by a combination of all the variables considered into a single BDT discriminant. One can see that, in all cases, the rejection power of this "all variables" BDT is significantly larger than the best two-variable combination. This indicates that beyond the best two-variable combination there is still significant complementary information availiable in the remaining variables in order to improve the discrimination of signal and background. How much complementary information is available appears to be p_T dependent. In the lower p_T 300-400 and 500-600 GeV bins the background rejection of the "all variables" combination is a factor ~ 1.5 greater than the best two-variable combination, but in the highest p_T bin it is a factor ~ 2.5 greater.

The final column in Figures 15, 16 and 17 allows us to explore the all variables performance a little further. It shows the background rejection for three variable BDT combinations of $m_{sd}^{\beta=2} + C_2^{\beta=1} + X$, where X is the variable on the y-axis. For jets with R=0.4 and R=0.8, the combination $m_{sd}^{\beta=2} + C_2^{\beta=1}$ is the best performant (or very close to the best performant) two-variable combination in every p_T bin considered. For R=1.2 this is not the case, as $C_2^{\beta=1}$ is superceded by $\tau_{21}^{\beta=1}$ in performance, as discussed earlier. Thus, in considering the three-variable combination results it is best to focus on the R=0.4 and R=0.8 cases. Here we see that, for the lower p_T 300-400 and 500-600 GeV bins, adding the third variable to the best two-variable combination brings us to within $\sim 15\%$ of the "all variables" background rejection. However, in the highest p_T 1.0-1.1 TeV bin, whilst adding the third variable does improve the performance considerably, we are still $\sim 40\%$ from the observed "all variables" background rejection, and clearly adding a fourth or maybe even fifth variable would bring considerable gains. In terms of which variable offers the best improvement when added to the $m_{sd}^{\beta=2} + C_2^{\beta=1}$ combination, it is hard to see an obvious pattern; the best third variable changes depending on the p_T and R considered.

In conclusion, it appears that there is a rich and complex structure in terms of the degree to which the discriminatory information provided by the set of variables considered overlaps, with the degree of overlap apparently decreasing at higher p_T . This suggests that in all p_T ranges, but especially at higher p_T , there are substantial performance gains to be made by designing a more complex multivariate W tagger.

6.4 Conclusions

We have studied the performance, in terms of the degree to which a hadronically decaying W boson can be separated from a gluonic background, of a number of groomed jet masses, substructure variables, and BDT combinations of the above. We have used this to build a picture of how the discriminatory information contained in the variables overlaps, and how this complementarity between the variables changes with p_T and anti-k_T distance parameter R.

In terms of the performance of individual variables, we find that, in agreement with other studies**[REF]**, in general the groomed masses perform best, with a background rejection power that increases with increasing p_T , but which is more constant with respect to changes in R. Conversely, the performance of other substructure variables, such as $C_2^{\beta=1}$ and $\tau_{21}^{\beta=1}$ is more susceptible to changes in radius, with background rejection power decreasing with increasing R.

The best two-variable performance is obtained by combining a groomed mass with a substructure variable. Which particular substructure variable works best in combination is strongly dependent on p_T and R. $C_2^{\beta=1}$ offers significant complimentarity to groomed mass at smaller R, owing to the

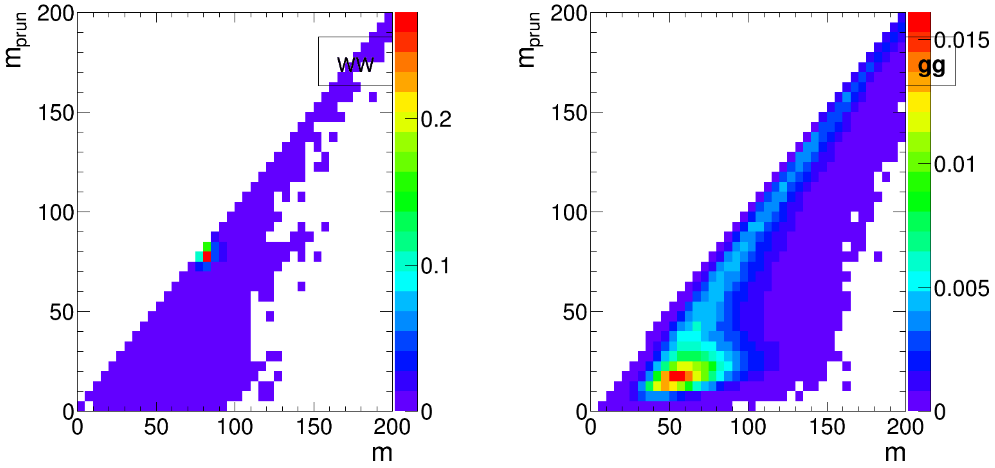

(a) Pruned mass vs ungroomed mass

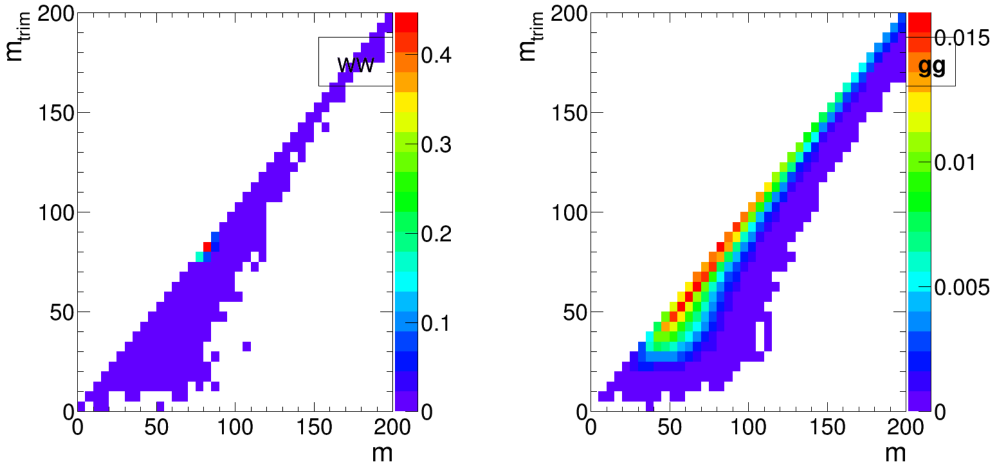

(b) Trimmed mass vs ungroomed mass

Fig. 21 2-D plots showing the correlation between groomed and ungroomed mass for WW and gg events in the p_T 1.0-1.1 TeV bin using the anti-k_{T} R=0.4 algorithm.

small degree of correlation between the variables. However, the sensitivity of $C_2^{\beta=1}$ to soft, wide-angle radiation leads to worse discrimination power at large R, where $\tau_{21}^{\beta=1}$ performs better in combination. Our studies also demonstrate the potential for enhanced discrmination by combining groomed and ungroomed mass information, although the use of ungroomed mass in this may in practice be limited by the presence of pile-up that is not considered in these studies.

By examining the performance of a BDT combination of all the variables considered, it is clear that there are potentially substantial performance gains to be made by designing a more complex multivariate W tagger, especially at higher p_T .

7 Top Tagging

In this section, we study the identification of boosted top quarks at Run II of the LHC. Boosted top quarks result in large-radius jets with complex substructure, containing a b-subjet and a boosted W. The additional kinematic handles coming from the reconstruction of the W mass and b-tagging allow a very high degree of discrimination of top quark jets from QCD backgrounds.

We consider top quarks with moderate boost (600-1000 GeV), and perhaps most interestingly, at high boost ($\gtrsim$ 1500 GeV). Top tagging faces several challenges in the high-p_T regime. For such high-p_T jets, the b-tagging efficiencies are no longer reliably known. Also, the top jet can also accompanied by additional radiation with $p_T \sim m_t$, leading to combinatoric ambiguities of reconstructing the top and W, and

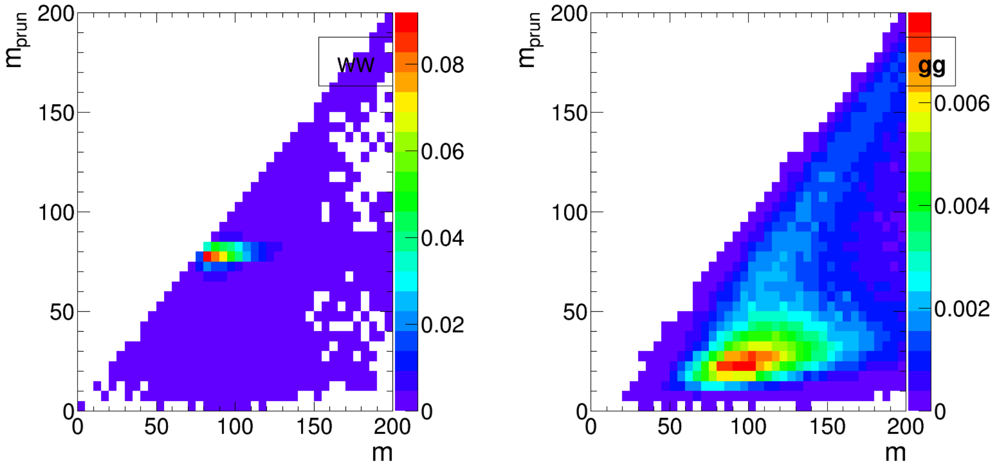

(a) Pruned mass vs ungroomed mass

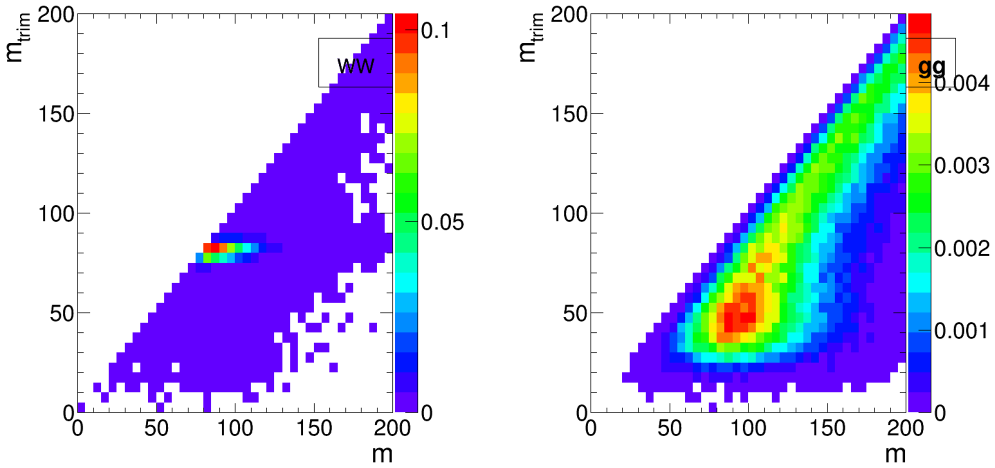

(b) Trimmed mass vs ungroomed mass

Fig. 22 2-D plots showing the correlation between groomed and ungroomed mass for WW and gg events in the p_T 1.0-1.1 TeV bin using the anti-k_{T} R=0.8 algorithm.

the possibility that existing taggers or observables shape the background by looking for subjet combinations that reconstruct m_t/m_W. To study this, we examine the performance of both mass-reconstruction variables, as well as shape observables that probe the three-pronged nature of the top jet and the accompanying radiation pattern.

We use the top quark MC samples for each bin described in Section 2.2. The analysis relies on FastJet 3.0.3 for jet clustering and calculation of jet substructure observables. Jets are clustered using the anti-k_t algorithm. An upper and lower p_T cut are applied after jet clustering to each sample to ensure similar p_T spectra in each bin. The bins in leading jet p_T that are investigated for top tagging are 600-700 GeV, 1-1.1 TeV, and 1.5-1.6 TeV. Jets are clustered with radii $R = 0.4$, 0.8, and 1.2; $R = 0.4$ jets are only studied in the 1.5-1.6 TeV bin because for top quarks with this boost, the top decay products are all contained within an $R = 0.4$ jet.

7.1 Methodology

We study a number of top-tagging strategies, in particular:

1. HEPTopTagger
2. Johns Hopkins Tagger (JH)
3. Trimming
4. Pruning

The top taggers have criteria for reconstructing a top and W candidate, and a corresponding top and W mass, as described in Section 3.3, while the grooming algorithms (trimming and pruning) do not incorporate a W-identification step.

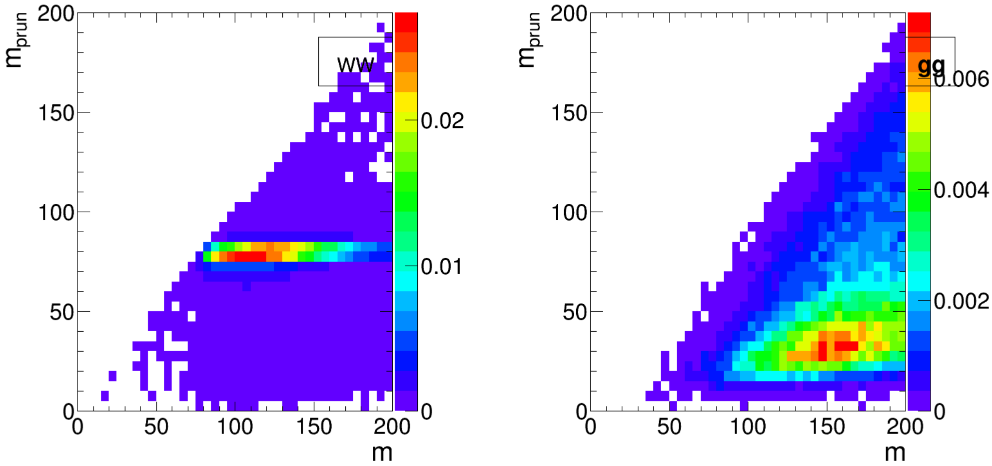

(a) Pruned mass vs ungroomed mass

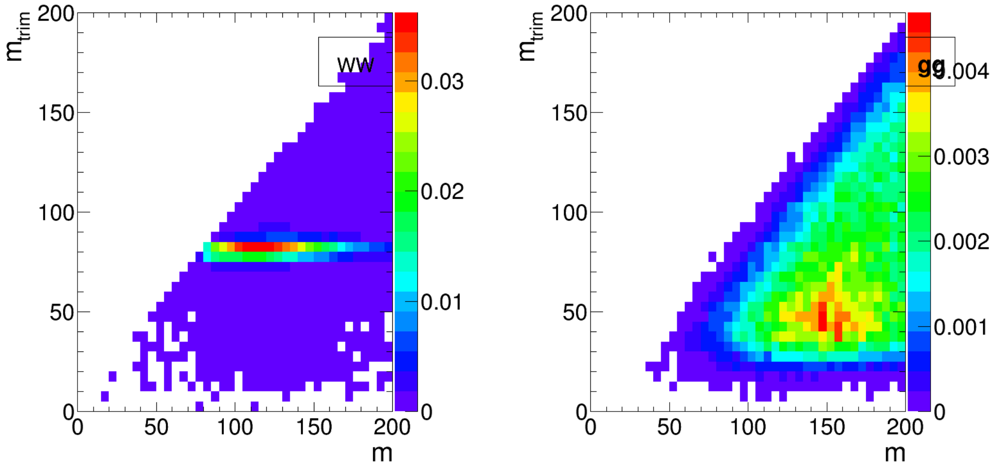

(b) Trimmed mass vs ungroomed mass

Fig. 23 2-D plots showing the correlation between groomed and ungroomed mass for WW and gg events in the p_T 1.0-1.1 TeV bin using the anti-k_{T} R=1.2 algorithm.

For a level playing field, where grooming is used we construct a W candidate mass, m_W, from the three leading subjets by taking the mass of the pair of subjets with the smallest invariant mass; in the case that only two subjets are reconstructed, we take the mass of the leading subjet. The top mass, m_t, is the mass of the groomed jet. All of the above taggers and groomers incorporate a step to remove pile-up and other soft radiation.

We also consider the performance of the following jet shape observables:

- The ungroomed jet mass.
- N-subjettiness ratios τ_2/τ_1 and τ_3/τ_2 with $\beta = 1$ and the "winner-takes-all" axes.
- 2-point energy correlation function ratios $C_2^{\beta=1}$ and $C_3^{\beta=1}$.
- The pruned Qjet mass volatility, Γ_{Qjet}.

In addition to the jet shape performance, we combine the jet shapes with the mass-reconstruction methods described above to determine the optimal combined performance.

For determining the performance of multiple variables, we combine the relevant tagger output observables and/or jet shapes into a boosted decision tree (BDT), which determines the optimal cut. Additionally, because each tagger has two input parameters, as described in Section 3.3, we scan over reasonable values of the parameters to determine the optimal value that gives the largest background rejection for each top tagging signal efficiency. This allows a direct comparison of the optimized version of each tagger. The input values scanned for the various algorithms are:

- **HEPTopTagger:** $m \in [30, 100]$ GeV, $\mu \in [0.5, 1]$
- **JH Tagger:** $\delta_p \in [0.02, 0.15]$, $\delta_R \in [0.07, 0.2]$
- **Trimming:** $f_{\mathrm{cut}} \in [0.02, 0.14]$, $R_{\mathrm{trim}} \in [0.1, 0.5]$

– **Pruning:** $z_{\mathrm{cut}} \in [0.02, 0.14]$, $R_{\mathrm{cut}} \in [0.1, 0.6]$

7.2 Single-observable performance

We start by investigating the behaviour of individual jet substructure observables. Because of the rich, three-pronged structure of the top decay, it is expected that combinations of masses and jet shapes will far outperform single observables in identifying boosted tops. However, a study of the top-tagging performance of single variables facilitates a direct comparison with the W tagging results in Section 6, and also allows a straightforward examination of the performance of each observable for different p_T and jet radius.

Fig. 24 shows the ROC curves for each of the top-tagging observables, with the bare (ungroomed) jet mass also plotted for comparison. The jet shape observables all perform substantially worse than jet mass, unlike W tagging for which several observables are competitive with or perform better than jet mass (see, for example, Fig. 10). To understand why this is the case, consider N-subjettiness. The W is two-pronged and the top is three-pronged; therefore, we expect τ_{21} and τ_{32} to be the best-performant N-subjettiness ratio, respectively. However, τ_{21} also contains an implicit cut on the denominator, τ_1, which is strongly correlated with jet mass. Therefore, τ_{21} combines both mass and shape information to some extent. By contrast, and as is clear in Fig.24(a), the best shape for top tagging is τ_{32}, which contains no information on the mass. Therefore, it is unsurprising that the shapes most useful for top tagging are less sensitive to the jet mass, and under-perform relative to the corresponding observables for W tagging.

Of the two top tagging algorithms, we can see from Figure 24 that the Johns Hopkins (JH) tagger out-performs the HEPTopTagger in terms of its signal-to-background separation power in both the top and W candidate masses. In Figure 25 we show the histograms for the top mass output from the JH and HEPTopTagger for different R in the p_T 1.5-1.6 TeV bin, and in Figure 26 for different p_T at at R =0.8, optimized at a signal efficiency of 30%. One can see from these figures that the likely reason for the better performance of the JH tagger is that, in the HEPTopTagger algorithm, the jet is filtered to select the five hardest subjets, and then three subjets are chosen which reconstruct the top mass. This requirement tends to shape a peak in the QCD background around m_t for the HEPTopTagger, while the JH tagger has no such requirement. It has been suggested by Anders *et al.* [48] that performance in the HEPTopTagger may be improved by selecting the three subjets reconstructing the top only among those that pass the W mass constraints, which somewhat reduces the shaping of the background. The discrepancy between the JH and HEPTopTaggers is more pronounced at higher p_T and larger jet radius (see Figs. 29 and 32).

We also see in Figure 24(b) that the top mass from the JH tagger and the HEPTopTagger has superior performance relative to either of the grooming algorithms; this is because the pruning and trimming algorithms do not have inherent W-identification steps and are not optimized for this purpose. Indeed, because of the lack of a W-identification step, grooming algorithms are forced to strike a balance between under-grooming the jet, which broadens the signal peak due to UE contamination and features a larger background rate, and over-grooming the jet, which occasionally throws out the b-jet and preserves only the W components inside the jet. We demonstrate this effect in Figures 25 and 26, showing that with $\varepsilon_{\mathrm{sig}} = 0.3 - 0.35$, the optimal performance of the tagger over-grooms a substantial fraction of the jets ($\sim 20 - 30\%$), leading to a spurious second peak at the W mass. This effect is more pronounced at large R and p_T, since more aggressive grooming is required in these limits to combat the increased contamination from UE and QCD radiation.

In Figures 27 and 29 we directly compare ROC curves for jet shape observable performance and top mass performance respectively in the three different p_T bins considered whilst keeping the jet radius fixed at R=0.8. The input parameters of the taggers, groomers and shape variables are separately optimized in each p_T bin. One can see from Figure 27 that the tagging performance of jet shapes do not change substantially with p_T. The observables $\tau_{32}^{(\beta=1)}$ and Qjet volatility Γ have the most variation and tend to degrade with higher p_T, as can be seen in Figure 28. This makes sense, as higher-p_T QCD jets have more, harder emissions within the jet, giving rise to substructure that fakes the signal. By contrast, from Figure 29 we can see that most of the top mass observables have superior performance at higher p_T due to the radiation from the top quark becoming more collimated. The notable exception is the HEPTopTagger, which degrades at higher p_T, likely in part due to the background-shaping effects discussed earlier.

In Figures 30 and 32 we directly compare ROC curves for jet shape observable performance and top mass performance respectively for the three different jet radii considered within the p_T 1.5-1.6 TeV bin. Again, the input parameters of the taggers, groomers and shape variables are separately optimized for each jet radius. We can see from these figures that most of the top tagging variables, both shape and reconstructed top mass, perform best for smaller radius. This is likely because, at such high p_T, most of the radiation from the top quark is confined within $R = 0.4$, and having a larger jet radius makes the observable more susceptible to contamination from the underlying event and other uncorrelated radiation. In Figure 31, we compare the individual top signal and QCD background distributions for each shape variable considered in the p_T 1.5-1.6 TeV bin for the various jet radii. One can see that the distributions for both signal and background broaden with increasing R, degrading the discrimi-

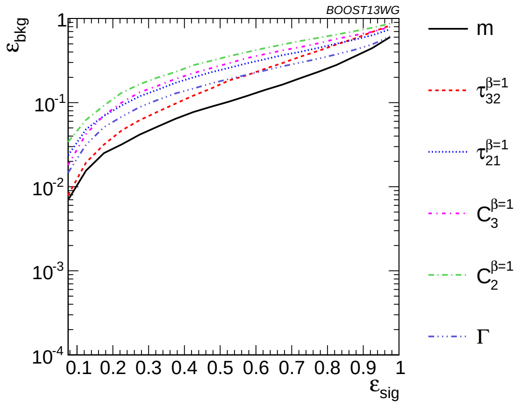

(a) Jet shapes

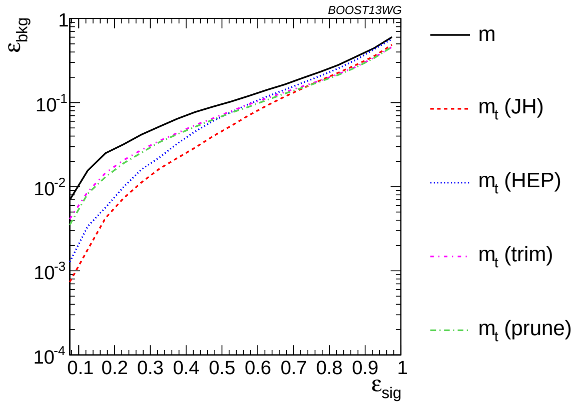

(b) Top mass

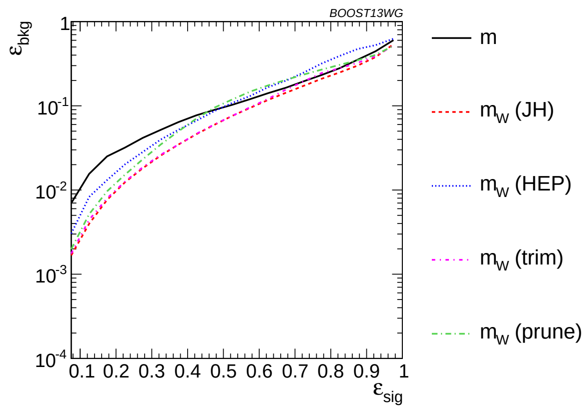

(c) W mass

Fig. 24 Comparison of single-variable top-tagging performance in the $p_T = 1-1.1$ GeV bin using the anti-k_{T}, R=0.8 algorithm.

nating power. For $C_2^{(\beta=1)}$ and $C_3^{(\beta=1)}$, the background distributions are shifted upward as well. Therefore, the discriminating power generally gets worse with increasing R. The main exception is for $C_3^{(\beta=1)}$, which performs optimally at $R = 0.8$; in this case, the signal and background coincidentally happen to have the same distribution around $R = 0.4$, and so $R = 0.8$ gives better discrimination.

7.3 Performance of multivariable combinations

We now consider various BDT combinations of the observables from Section 7.2, using the techniques described in Section 4. In particular, we consider the performance of individual taggers such as the JH tagger and HEPTopTagger, which output information about the top and W candidate masses and the helicity angle; groomers, such as trimming and pruning, which remove soft, uncorrelated radiation from the top candidate to improve mass reconstruction, and to which we have added a W reconstruction step; and the combination of the outputs of the above taggers/groomers, both with each other, and with shape variables such as N-subjettiness ratios and energy correlation ratios. For all observables with tuneable input parameters, we scan and optimize over realistic values of such parameters, as described in Section 7.1.

In Figure 33, we directly compare the performance of the HEPTopTagger, the JH tagger, trimming, and pruning, in the $p_T = 1-1.1$ TeV bin using jet radius R=0.8, where both m_t and m_W are used in the groomers. Generally, we find that pruning, which does not naturally incorporate subjets into the algorithm, does not perform as well as the others. Interestingly, trimming, which does include a subjet-identification step, performs comparably to the HEPTopTagger over much of the range, possibly due to the background-shaping observed in Section 7.2. By contrast, the JH tagger outperforms the other algorithms. To determine whether there is complementary information in the mass outputs from different top taggers, we also consider in Figure 33 a multivariable combination of all of the JH and HEPTopTagger outputs. The maximum efficiency of the combined JH and HEPTopTaggers is limited, as some fraction of signal events inevitably fails either one or other of the taggers. We do see a 20-50% improvement in performance when combining all outputs, which suggests that the different algorithms used to identify

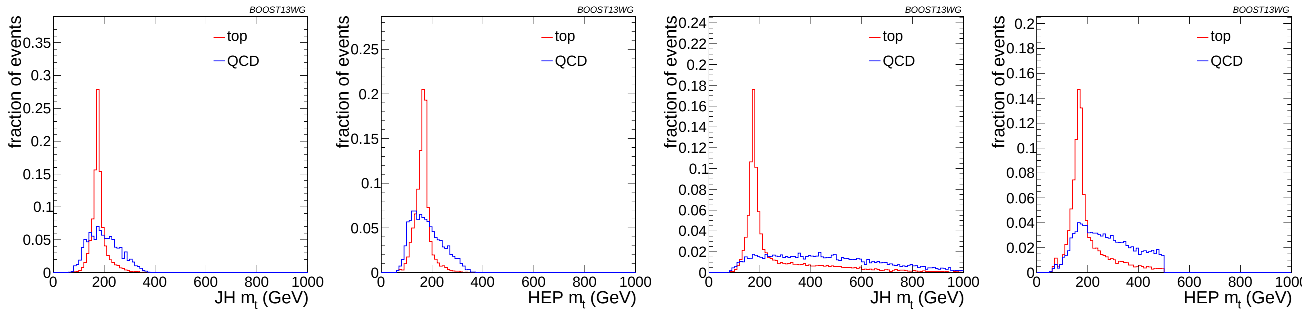

(a) JH, $R = 0.4$ (b) HEP, $R = 0.4$ (c) JH, $R = 1.2$ (d) HEP, $R = 1.2$

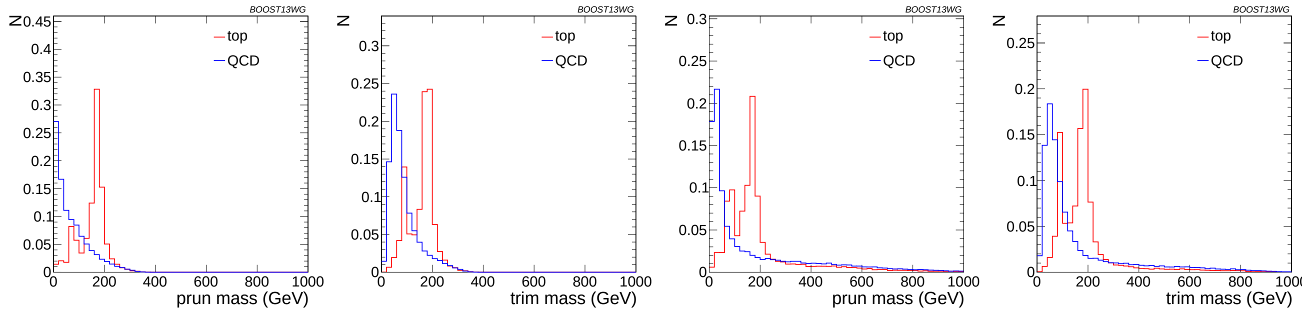

(e) prune, $R = 0.4$ (f) trim, $R = 0.4$ (g) prune, $R = 1.2$ (h) trim, $R = 1.2$

Fig. 25 Comparison of top mass reconstruction with the Johns Hopkins (JH), HEPTopTaggers (HEP), pruning, and trimming at different R using the anti-k_{T} algorithm, $p_{\mathrm{T}} = 1.5 - 1.6$ TeV. Each histogram is shown for the working point optimized for best performance with m_t in the $0.3 - 0.35$ signal efficiency bin, and is normalized to the fraction of events passing the tagger. In this and subsequent plots, the HEPTopTagger distribution cuts off at 500 GeV because the tagger fails to tag jets with a larger mass.

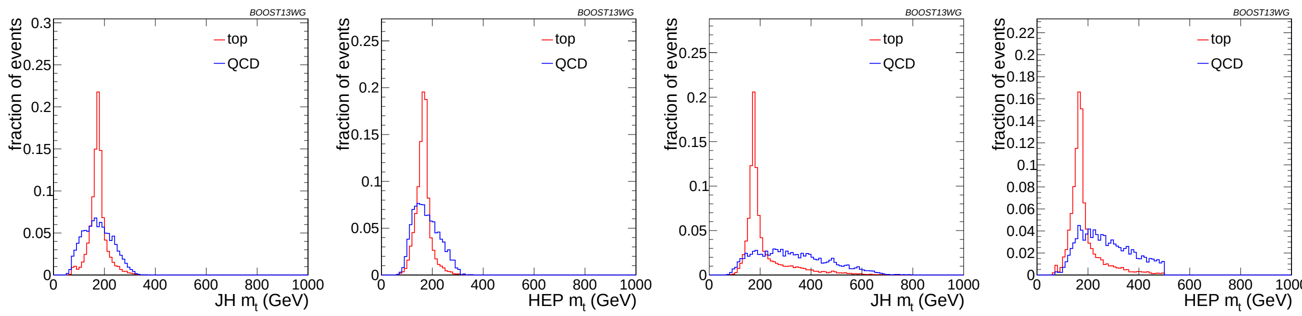

(a) JH, $p_T = 600 - 700$ GeV (b) HEP, $p_T = 600 - 700$ GeV (c) JH, $p_T = 1.5 - 1.6$ TeV (d) HEP, $p_T = 1.5 - 1.6$ TeV

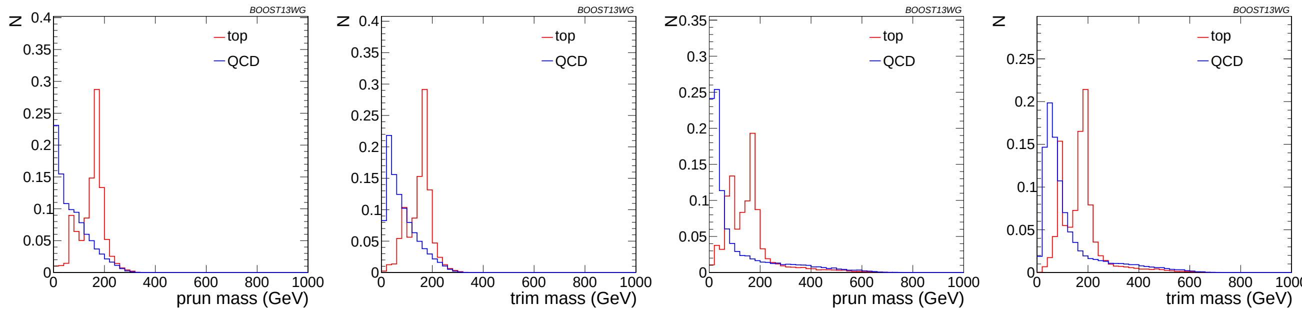

(e) prune, $p_T = 600 - 700$ GeV (f) trim, $p_T = 600 - 700$ GeV (g) prune, $p_T = 1.5 - 1.6$ TeV (h) trim, $p_T = 1.5 - 1.6$ TeV

Fig. 26 Comparison of top mass reconstruction with the Johns Hopkins (JH), HEPTopTaggers (HEP), pruning, and trimming at different p_T using the anti-k_{T} algorithm, $R = 0.8$. Each histogram is shown for the working point optimized for best performance with m_t in the $0.3 - 0.35$ signal efficiency bin, and is normalized to the fraction of events passing the tagger.

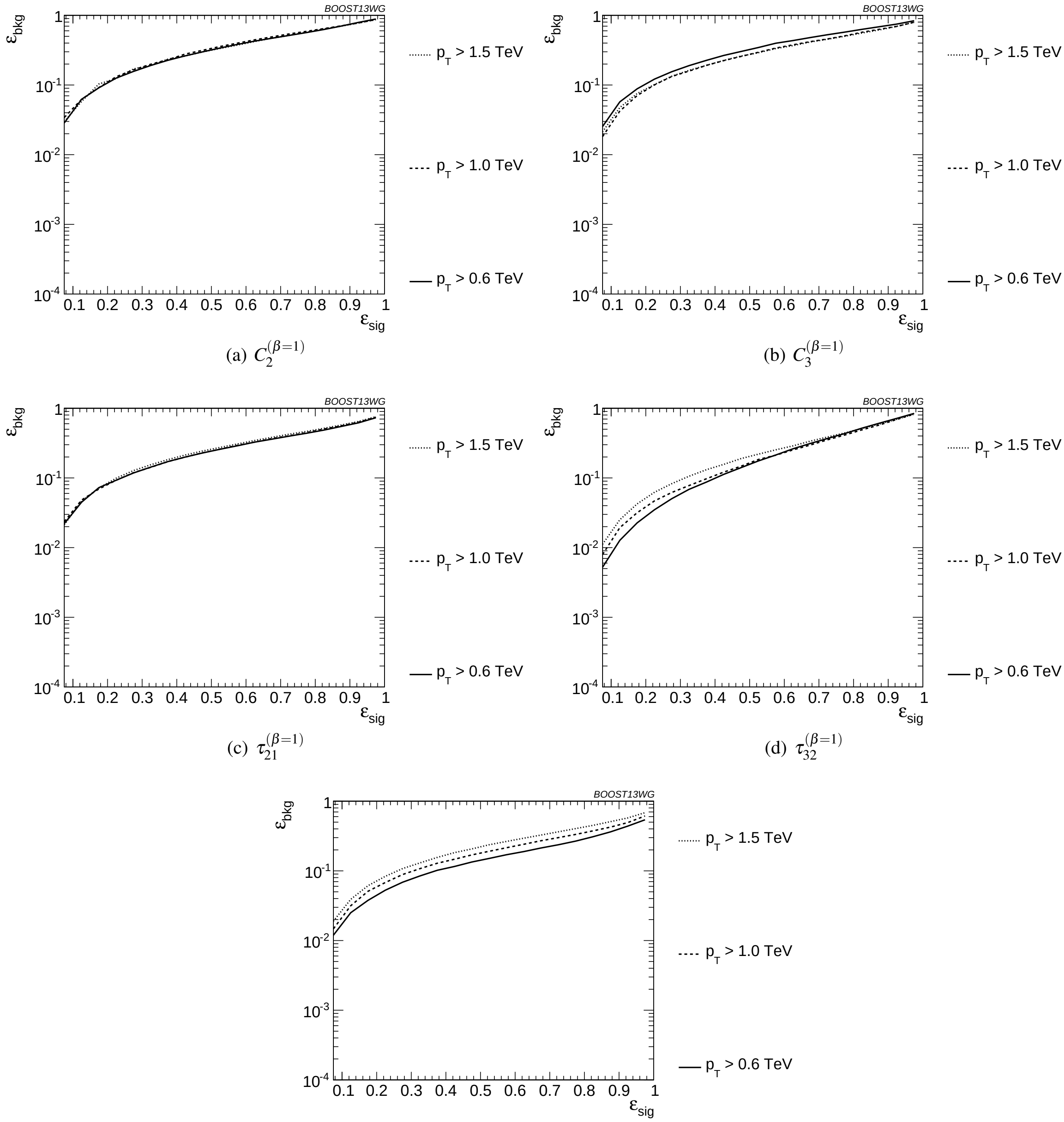

(a) $C_2^{(\beta=1)}$ (b) $C_3^{(\beta=1)}$

(c) $\tau_{21}^{(\beta=1)}$ (d) $\tau_{32}^{(\beta=1)}$

(e) Qjet mass volatility

Fig. 27 Comparison of individual jet shape performance at different p_T using the anti-k_T R=0.8 algorithm.

the top and W for different taggers contains complementary information.

In Figure 34 we present the results for multivariable combinations of the top tagger outputs with and without shape variables. We see that, for both the HEPTopTagger and the JH tagger, the shape observables contain additional information uncorrelated with the masses and helicity angle, and give on average a factor 2-3 improvement in signal discrimination. We see that, when combined with the tagger outputs, both the energy correlation functions $C_2 + C_3$ and the N-subjettiness ratios $\tau_{21} + \tau_{32}$ give comparable performance, while the Qjet mass volatility is slightly worse; this is unsurprising, as Qjets accesses shape information in a more indirect way from other shape observables. Combining all shape observables with a single top tagger provides even greater enhancement in discrimination power. We directly

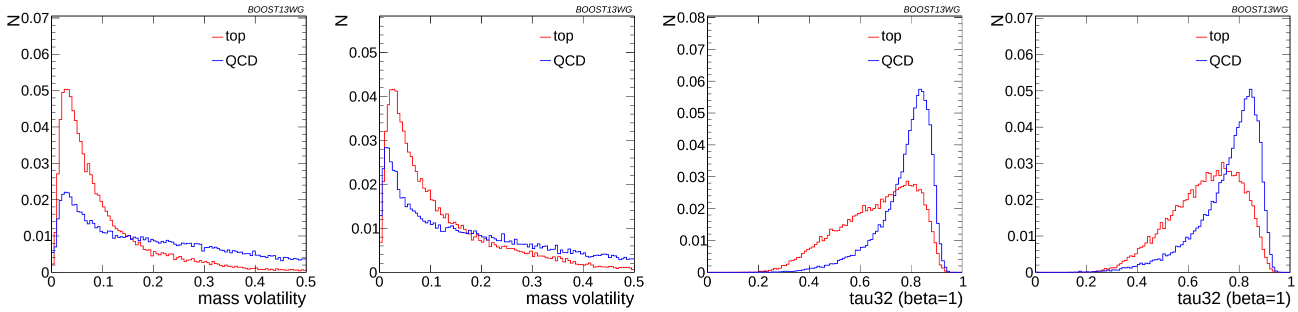

(a) Γ_{Qjet}, $p_T = 600-700$ GeV (b) Γ_{Qjet}, $p_T = 1.5-1.6$ TeV (c) $\tau_{32}^{(\beta=1)}$, $p_T = 600-700$ GeV (d) $\tau_{32}^{(\beta=1)}$, $p_T = 1.5-1.6$ TeV

Fig. 28 Comparison of Γ_{Qjet} and $\tau_{32}^{\beta=1}$ at $R = 0.8$ and different values of the p_T. These shape observables are the most sensitive to varying p_T.

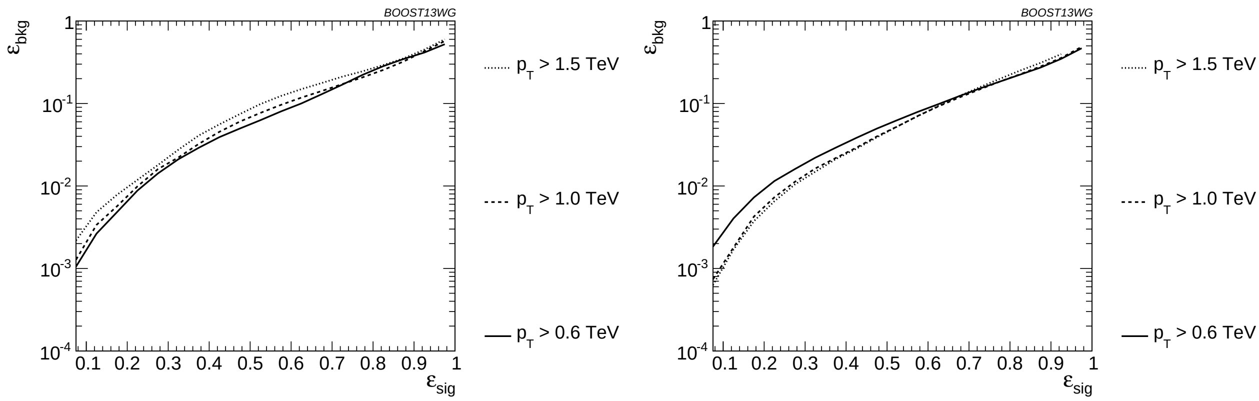

(a) HEPTopTagger m_t (b) Johns Hopkins Tagger m_t

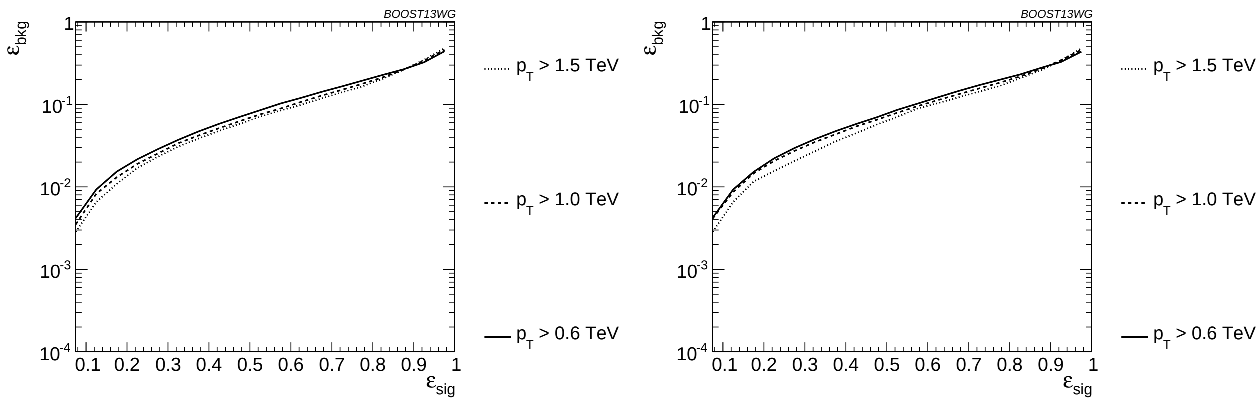

(c) Pruning m_t (d) Trimming m_t

Fig. 29 Comparison of top mass performance of different taggers at different p_T using the anti-k_{T} R=0.8 algorithm.

compare the performance of the JH and HEPTopTaggers in Figure 34(c). Combining the taggers with shape information nearly erases the difference between the tagging methods observed in Figure 33; this indicates that combining the shape information with the HEPTopTagger identifies the differences between signal and background missed by the tagger alone. This also suggests that further improvement to discriminating power may be minimal, as various multivariable combinations are converging to within a factor of 20% or so.

In Figure 35 we present the results for multivariable combinations of groomer outputs with and without shape variables. As with the tagging algorithms, combinations of groomers with shape observables improves their discriminating power; combinations with $\tau_{32} + \tau_{21}$ perform comparably to those with $C_3 + C_2$, and both of these are superior to combinations with the mass volatility, Γ. Substantial improvement is

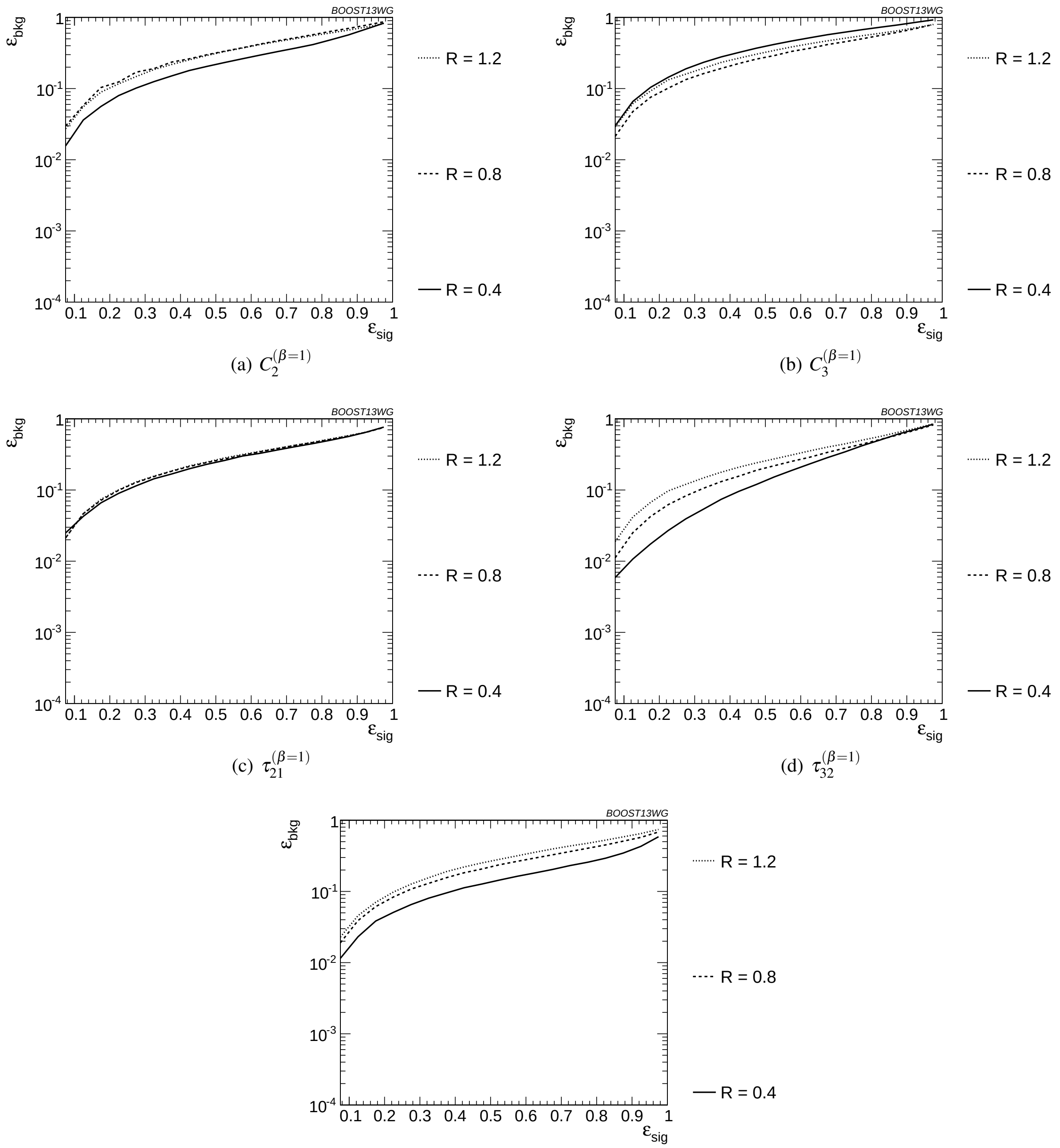

(a) $C_2^{(\beta=1)}$ (b) $C_3^{(\beta=1)}$

(c) $\tau_{21}^{(\beta=1)}$ (d) $\tau_{32}^{(\beta=1)}$

(e) Qjet mass volatility

Fig. 30 Comparison of individual jet shape performance at different R in the $p_T = 1.5 - 1.6$ TeV bin.

further possible by combining the groomers with all shape observables. Not surprisingly, the taggers that lag behind in performance enjoy the largest gain in signal-background discrimination with the addition of shape observables. Once again, in Figure 35(c), we find that the differences between pruning and trimming are erased when combined with shape information.

Finally, in Figure 36, we compare the performance of each of the tagger/groomers when their outputs are combined with all of the shape observables considered. One can see that the discrepancies between the performance of the different taggers/groomers all but vanishes, suggesting perhaps that we are here utilising all available signal-background discrmination information, and that this is the optimal top

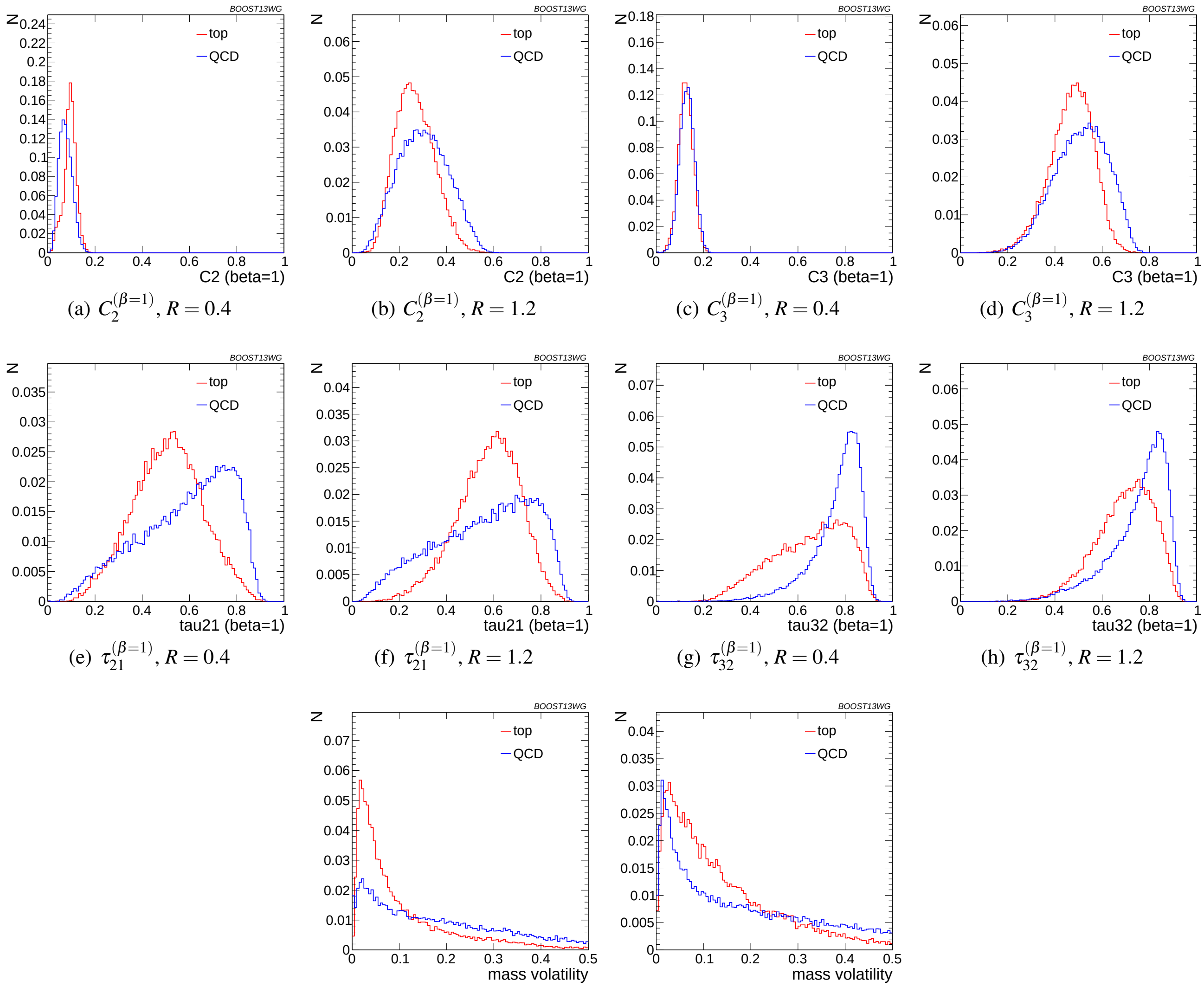

(a) $C_2^{(\beta=1)}$, $R = 0.4$ (b) $C_2^{(\beta=1)}$, $R = 1.2$ (c) $C_3^{(\beta=1)}$, $R = 0.4$ (d) $C_3^{(\beta=1)}$, $R = 1.2$

(e) $\tau_{21}^{(\beta=1)}$, $R = 0.4$ (f) $\tau_{21}^{(\beta=1)}$, $R = 1.2$ (g) $\tau_{32}^{(\beta=1)}$, $R = 0.4$ (h) $\tau_{32}^{(\beta=1)}$, $R = 1.2$

(i) Γ_{Qjet}, $R = 0.4$ (j) Γ_{Qjet}, $R = 1.2$

Fig. 31 Comparison of various shape observables in the $p_T = 1.5 - 1.6$ TeV bin and different values of the anti-k_{T} radius R.

tagging performance that could be achieved in these conditions.

Up to this point we have just considered the combined multivariable performance in the p_T 1.0-1.1 TeV bin with jet radius R=0.8. We now compare the BDT combinations of tagger outputs, with and without shape variables, at different p_T. The taggers are optimized over all input parameters for each choice of p_T and signal efficiency. As with the single-variable study, we consider anti-k_{T} jets clustered with $R = 0.8$ and compare the outcomes in the $p_T = 500 - 600$ GeV, $p_T = 1 - 1.1$ TeV, and $p_T = 1.5 - 1.6$ TeV bins. The comparison of the taggers/groomers is shown in Figure 37. The behaviour with p_T is qualitatively similar to the behaviour of the $m_t$observable for each tagger/groomer shown in Figure 29; this suggests that the p_T behaviour of the taggers is dominated by the top mass reconstruction. As before, the HEPTopTagger performance degrades slightly with increased p_T due to the background shaping effect, while the JH tagger and groomers modestly improve in performance.

In Figure 38, we show the p_T dependence of BDT combinations of the JH tagger output combined with shape observables. We find that the curves look nearly identical: the p_T dependence is dominated by the top mass reconstruction, and combining the tagger outputs with different shape observables does not substantially change this behaviour. The same holds true for trimming and pruning. By contrast, HEPTopTagger ROC curves, shown in Figure 39, do change somewhat when combined with different shape observables; due to the suboptimal performance of the HEPTopTagger at high p_T , we find that combining the HEPTopTagger with $C_3^{(\beta=1)}$, which in Figure 27(b) is seen to have some modest improvement at high p_T , can improve its performance.

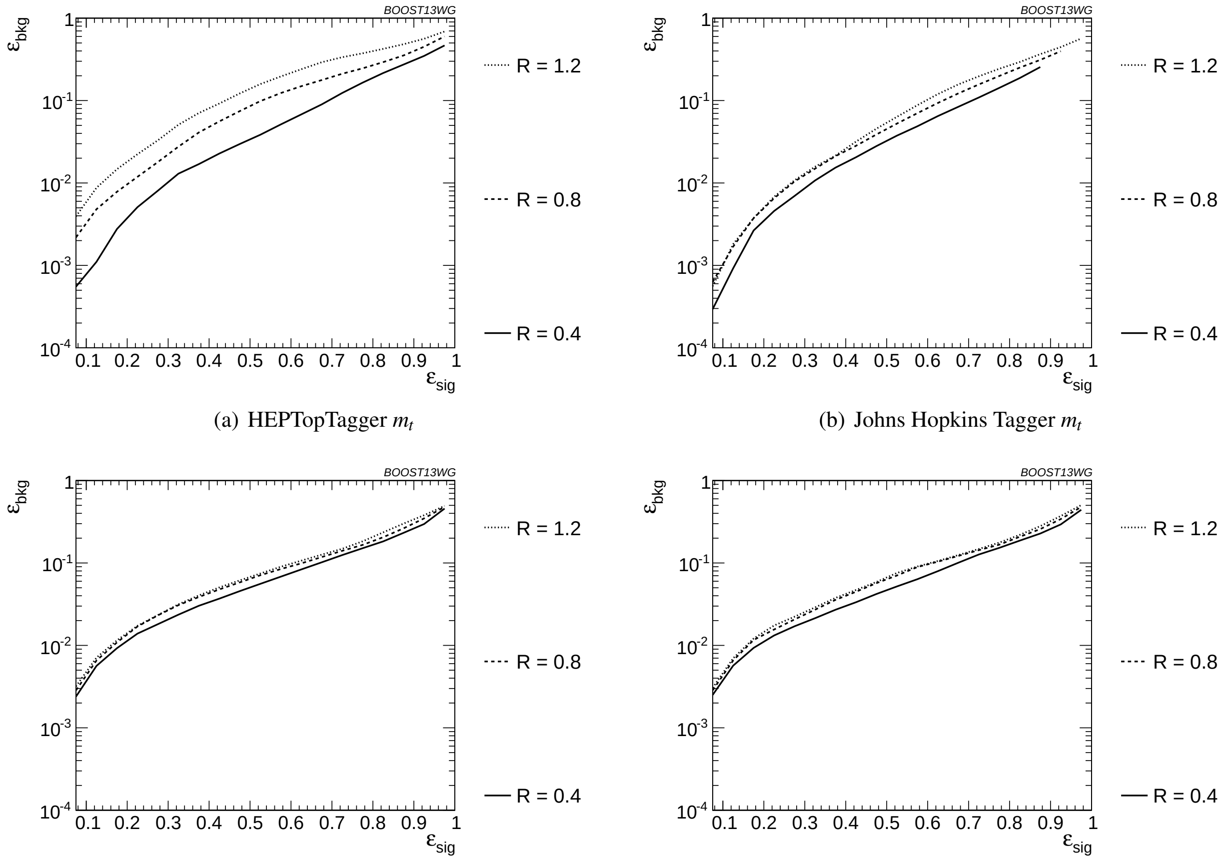

(a) HEPTopTagger m_t

(b) Johns Hopkins Tagger m_t

(c) Pruning m_t

(d) Trimming m_t

Fig. 32 Comparison of top mass performance of different taggers at different R in the $p_T = 1.5 - 1.6$ TeV bin.

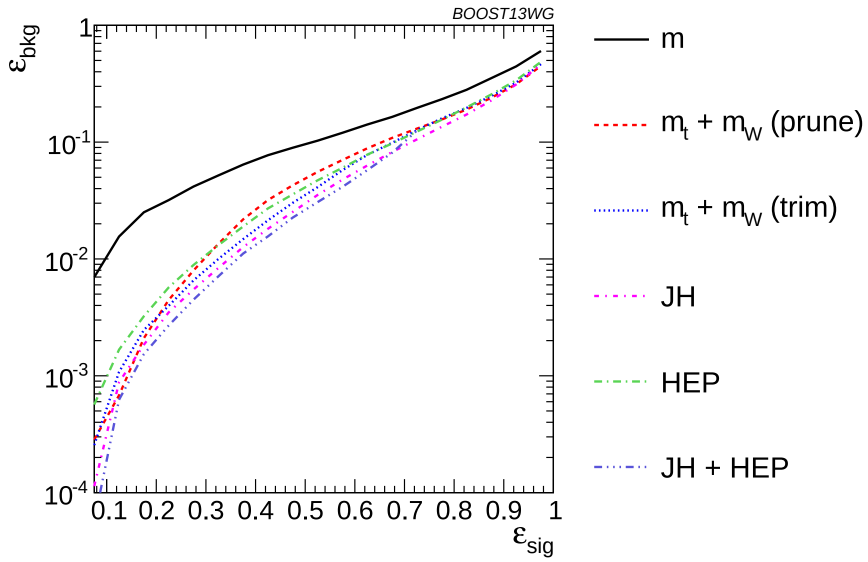

Fig. 33 The performance of the various taggers in the $p_T = 1 - 1.1$ TeV bin using the anti-k_T R=0.8 algorithm. For the groomers a BDT combination of the reconstructed $m_t$and $m_W$are used. Also shown is a multivariable combination of all of the JH and HEPTopTagger outputs. The ungroomed mass performance is shown for comparison.

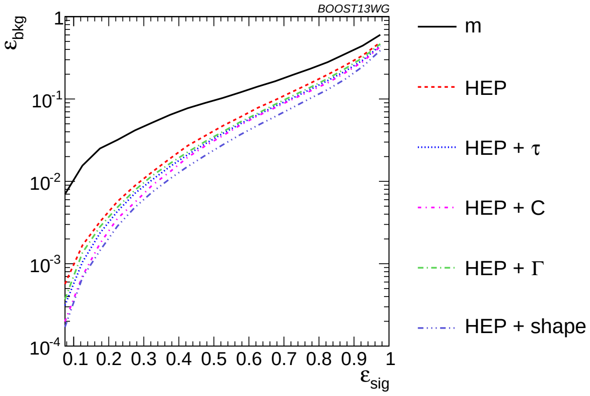

(a) HEPTopTagger + Shape

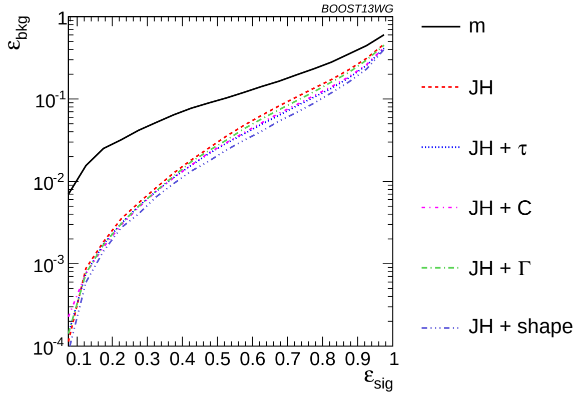

(b) Johns Hopkins Tagger + shape

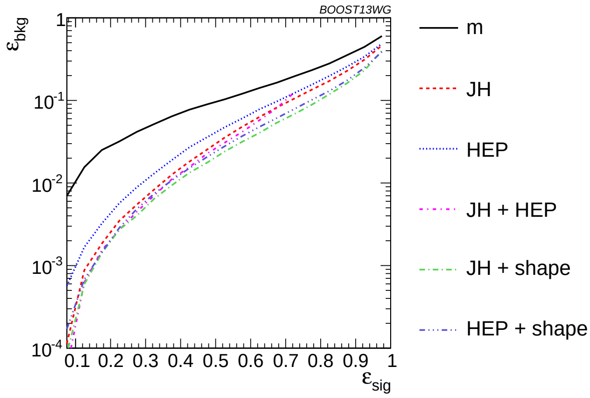

(c) HEP vs. JH comparison (incl. shape)

Fig. 34 The performance of BDT combinations of the JH and HepTopTagger outputs with various shape observables in the $p_T = 1-1.1$ TeV bin using the anti-k_{T} R=0.8 algorithm. Taggers are combined with the following shape observables: $\tau_{21}^{(\beta=1)} + \tau_{32}^{(\beta=1)}$, $C_2^{(\beta=1)} + C_3^{(\beta=1)}$, Γ_{Qjet}, and all of the above (denoted "shape").

Combining the HEPTopTagger with multiple shape observables gives the maximum improvement in performance at high p_T relative to at low p_T .

In Figure 40 we compare the BDT combinations of tagger outputs, with and without shape variables, at different jet radius R in the $p_T = 1.5-1.6$ TeV bin. The taggers are optimized over all input parameters for each choice of R and signal efficiency. We find that, for all taggers and groomers, the performance is always best at small R; the choice of R is sufficiently large to admit the full top quark decay at such high p_T , but is small enough to suppress contamination from additional radiation. This is not altered when the taggers are combined with shape observable. For example, in Figure 41 is shown the depedence on R of the JH tagger when combined with shape observables, where one can see that the R-dependence is identical for all combinations. The same holds true for the HEPTopTagger, trimming, and pruning.

7.4 Performance at Sub-Optimal Working Points

Up until now, we have re-optimized our tagger and groomer parameters for each p_T, R, and signal efficiency working point. In reality, experiments will choose a finite set of working points to use. How do our results hold up when this is taken into account? To address this concern, we replicate our analyses, but only optimize the top taggers for a particular p_T/R/efficiency and apply the same parameters to other scenarios. This allows us to determine the extent to which re-optimization is necessary to maintain the high signal-background discrimination power seen in the top tagging algorithms we study. The shape observables typically do not have any input parameters to optimize. Therefore, we focus on the taggers and groomers, and their combination with shape observables, in this section.

Optimizing at a single p_T : We show in Figure 42 the performance of the top taggers, using just the reconstructed top mass as the discriminating variable, with all input parameters optimized to the $p_T = 1.5-1.6$ TeV bin, relative to the performance optimized at each p_T. We see that while

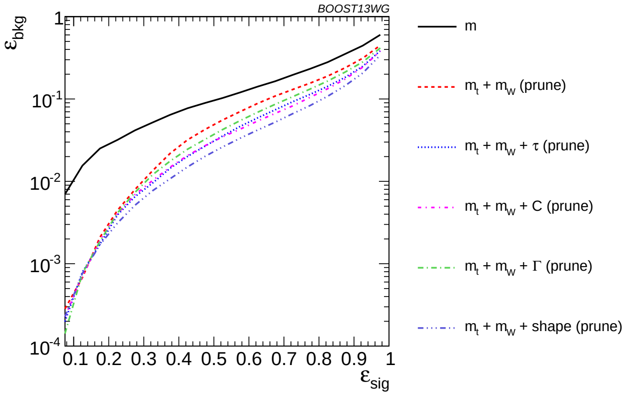

(a) Pruning + Shape

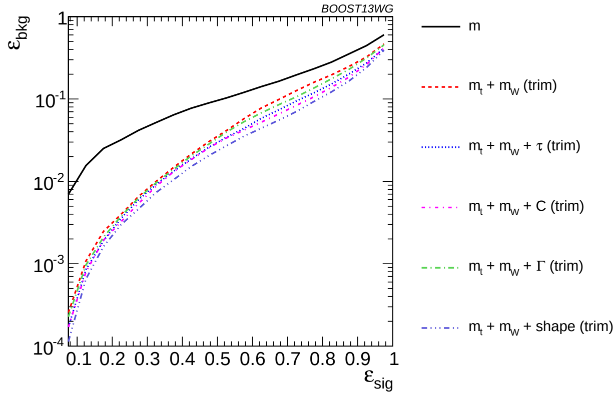

(b) Trimming + Shape

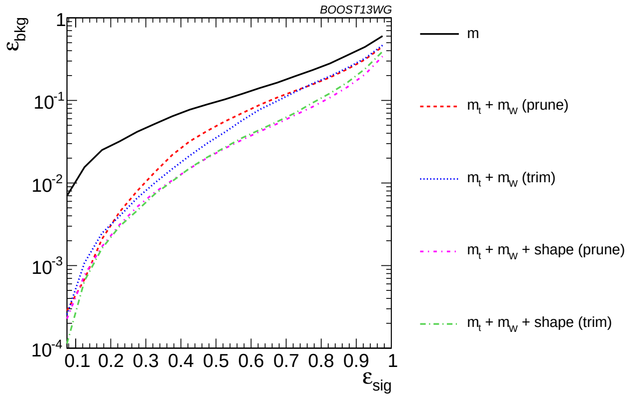

(c) Trim vs. Prune comparison (incl. shape)

Fig. 35 The performance of the BDT combinations of the trimming and pruning outputs with various shape observables in the $p_T = 1-1.1$ TeV bin using the anti-k_T R=0.8 algorithm. Groomer mass outputs are combined with the following shape observables: $\tau_{21}^{(\beta=1)} + \tau_{32}^{(\beta=1)}$, $C_2^{(\beta=1)} + C_3^{(\beta=1)}$, Γ_{Qjet}, and all of the above (denoted "shape").

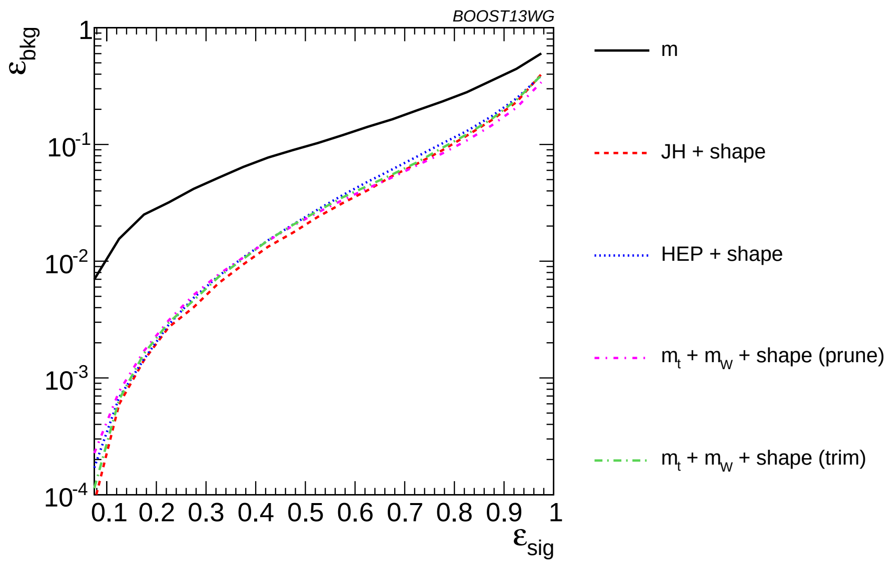

Fig. 36 Comparison of the performance of the BDT combinations of all the groomer/tagger outputs with all the available shape observables in the $p_T = 1-1.1$ TeV bin using the anti-k_T R=0.8 algorithm. Tagger/groomer outputs are combined with all of the following shape observables: $\tau_{21}^{(\beta=1)} + \tau_{32}^{(\beta=1)}$, $C_2^{(\beta=1)} + C_3^{(\beta=1)}$, Γ_{Qjet}.

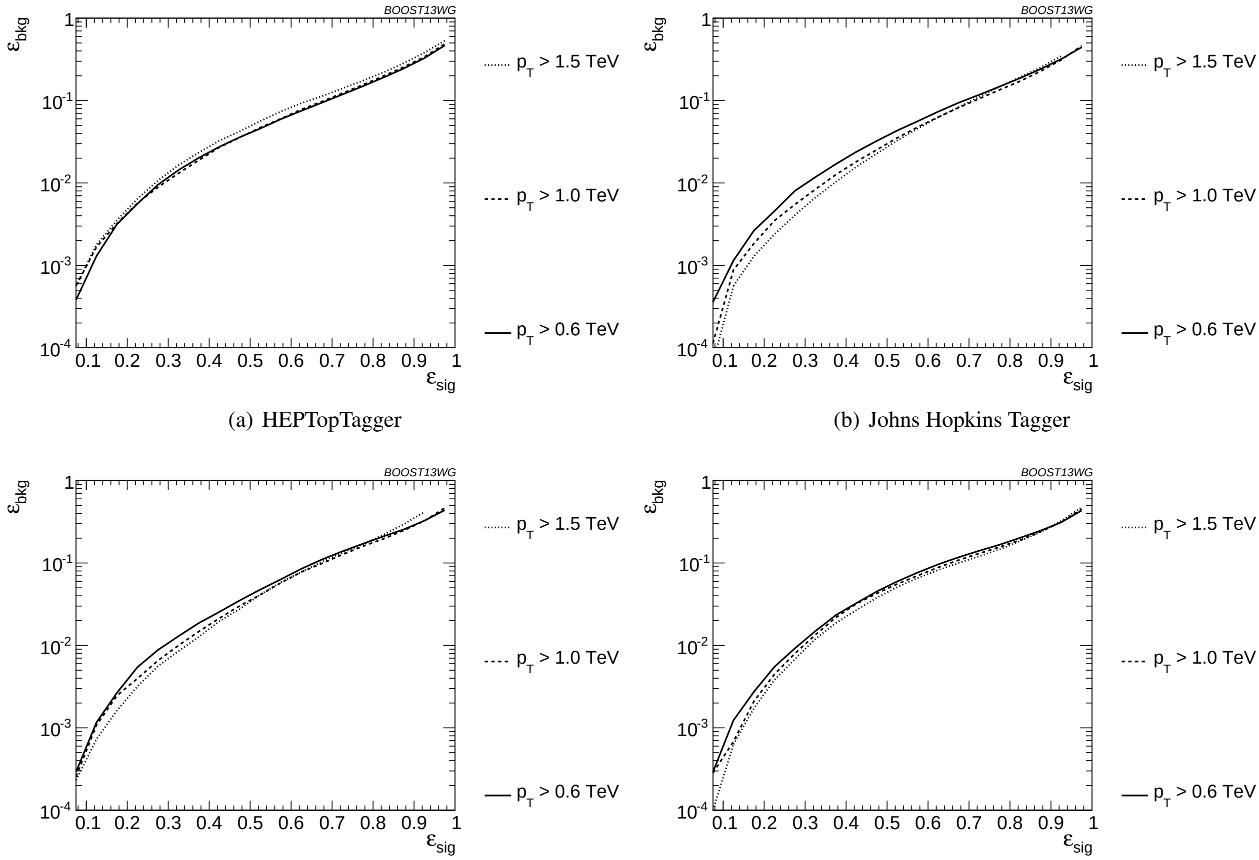

(a) HEPTopTagger

(b) Johns Hopkins Tagger

(c) Trimming

(d) Pruning

Fig. 37 Comparison of BDT combination of tagger performance at different p_T using the anti-k_T R=0.8 algorithm.

the performance degrades by about 50% when the high-p_T optimized points are used at other momenta, this is only an order-one adjustment of the tagger performance, with trimming and the Johns Hopkins tagger degrading the most. The jagged behaviour of the points is due to the finite resolution of the scan. We also observe a particular effect associated with using suboptimal taggers: since taggers sometimes fail to return a top candidate, parameters optimized for a particular efficiency ε_S at $p_T = 1.5-1.6$ TeV may not return enough signal candidates to reach the same efficiency at a different p_T. Consequently, no point appears for that p_T value. This is not often a practical concern, as the largest gains in signal discrimination and significance are for smaller values of ε_S, but it is something that must be considered when selecting benchmark tagger parameters and signal efficiencies.

The degradation in performance is more pronounced for the BDT combinations of the full tagger outputs, shown in Figure 43), particularly at very low signal efficiency where the optimization picks out a cut on the tail of some distribution that depends precisely on the p_T/R of the jet. Once again, trimming and the Johns Hopkins tagger degrade more markedly. Similar behaviour holds for the BDT combinations of tagger outputs plus all shape observables.

Optimizing at a single R: We perform a similar analysis, optimizing tagger parameters for each signal efficiency at $R = 1.2$, and then use the same parameters for smaller R, in the p_T 1.5-1.6 TeV bin. In Figure 44 we show the ratio of the performance of the top taggers, using just the reconstructed top mass as the discriminating variable, with all input parameters optimized to the $R = 1.2$ values compared to input parameters optimized separately at each radius. While the performance of each observable degrades at small $\varepsilon_{\mathrm{sig}}$ compared to the optimized search, the HEPTopTagger fares the worst as the observed is quite sensitive to the selected value of R. It is not surprising that a tagger whose top mass reconstruction is susceptible to background-shaping at large R and p_T would require a more careful optimization of parameters to obtain the best performance.

The same holds true for the BDT combinations of the full tagger outputs, shown in Figure 45). The performance for the sub-optimal taggers is still within an $O(1)$ factor of the optimized performance, and the HEPTopTagger per-

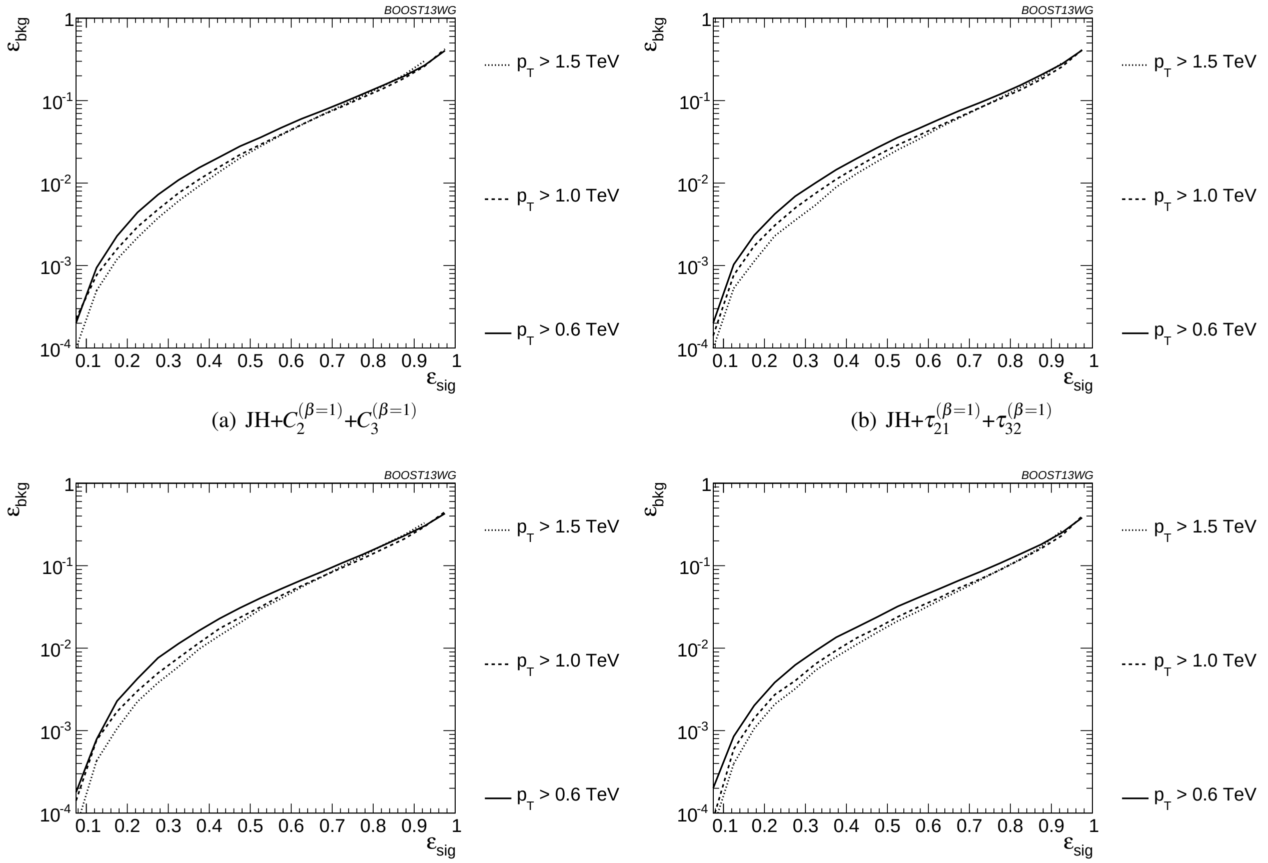

(a) JH+$C_2^{(\beta=1)}$+$C_3^{(\beta=1)}$

(b) JH+$\tau_{21}^{(\beta=1)}$+$\tau_{32}^{(\beta=1)}$

(c) JH + Qjet mass volatility

(d) JH + all

Fig. 38 Comparison of BDT combination of JH tagger + shape at different p_T using the anti-k_{T} R=0.8 algorithm.

forms better with the combination of all of its outputs relative to the performance with just m_t. The same behaviour holds for the BDT combinations of tagger outputs and shape observables.

Optimizing at a single efficiency: The strongest assumption we have made so far is that the taggers can be reoptimized for each signal efficiency point. This is useful for making a direct comparison of the power of different top tagging algorithms, but is not particularly practical for the LHC analyses. We now consider the effects when the tagger inputs are optimized once, in the $\varepsilon_S = 0.3-0.35$ bin, and then used to determine the full ROC curve. We do this in the $p_T 1-1.1$ TeV bin and with $R = 0.8$.

The performance of each tagger, normalized to its performance optimized in each bin, is shown in Figure 46 for cuts on the top mass and W mass, and in Figure 47 for BDT combinations of tagger outputs and shape variables. In both plots, it is apparent that optimizing the taggers in the 0.3-0.35 efficiency bin gives comparable performance over efficiencies ranging from 0.2-0.5, although performance degrades at small and large signal efficiencies. Pruning appears to give especially robust signal-background discrimination without re-optimization, possibly due to the fact that there are no absolute distance or p_T scales that appear in the algorithm. Figures 46 and 47 suggest that, while optimization at all signal efficiencies is a useful tool for comparing different algorithms, it is not crucial to achieve good top-tagging performance in experiments.

7.5 Conclusions

We have studied the performance of various jet substructure observables, groomed masses, and top taggers to study the performance of top tagging at different p_T and jet radius parameter. At each p_T, R, and signal efficiency working point, we optimize the parameters for those observables with tuneable inputs. Overall, we have found that these techniques, individually and in combination, continue to perform well at high p_T, which is important for future LHC running. In general, the John Hopkins tagger performs best, while jet grooming algorithms under-perform relative to the best top taggers due to the lack of an optimized W-identification step. Tagger performance can be improved by a further factor of

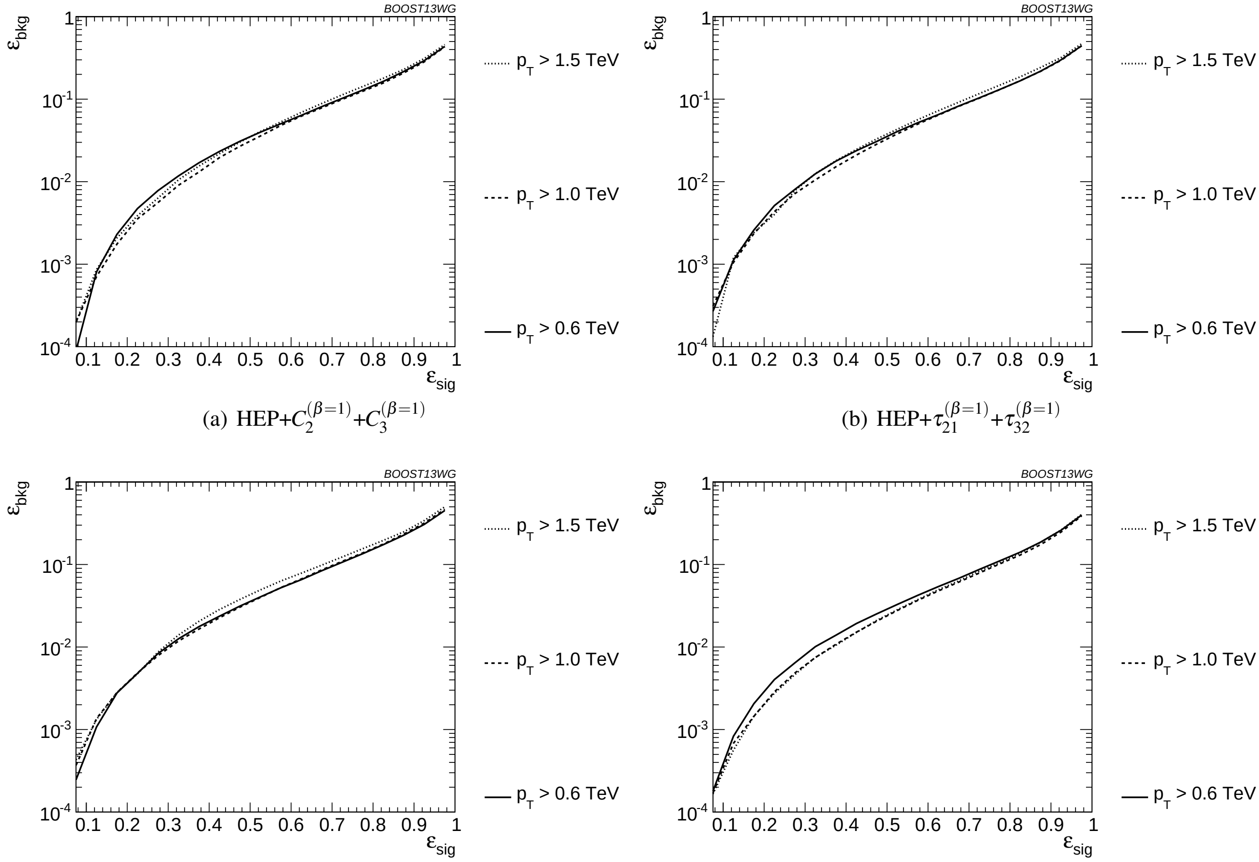

(a) HEP+$C_2^{(\beta=1)}$+$C_3^{(\beta=1)}$

(b) HEP+$\tau_{21}^{(\beta=1)}$+$\tau_{32}^{(\beta=1)}$

(c) HEP + Qjet mass volatility

(d) HEP + all

Fig. 39 Comparison of BDT combination of HEP tagger + shape at different p_T using the anti-k_{T} R=0.8 algorithm.

2-4 through combination with jet substructure observables such as τ_{32}, C_3, and Qjet mass volatility; when combined with jet substructure observables, the performance of various groomers and taggers becomes very comparable, suggesting that, taken together, the observables studied are sensitive to nearly all of the physical differences between top and QCD jets. A small improvement is also found by combining the Johns Hopkins and HEPTopTaggers, indicating that different taggers are not fully correlated.

Comparing results at different p_T and R, top tagging performance is generally better at smaller R due to less contamination from uncorrelated radiation. Similarly, most observables perform better at larger p_T due to the higher degree of collimation of radiation. Some observables fare worse at higher p_T, such as the N-subjettiness ratio τ_{32} and the Qjet mass volatility Γ, as higher-p_T QCD jets have more, harder emissions that fake the top jet substructure. The HEPTopTagger is also worse at large p_T due to the tendency of the tagger to shape backgrounds around the top mass. The p_T- and R-dependence of the multivariable combinations is dominated by the p_T- and R-dependence of the top mass reconstruction component of the tagger/groomer.

Finally, we consider the performance of various observable combinations under the more realistic assumption that the input parameters are only optimized at a single p_T, R, or signal efficiency, and then the same inputs are used at other working points. Remarkably, the performance of all observables is typically within a factor of 2 of the fully optimized inputs, suggesting that while optimization can lead to substantial gains in performance, the general behaviour found in the fully optimized analyses extends to more general applications of each variable. In particular, the performance of pruning typically varies the least when comparing suboptimal working points to the fully optimized tagger due to the scale-invariant nature of the pruning algorithm.

8 Summary & Conclusions

In this report we have attempted to understand the degree to which the discriminatory information in various jet substructure observables/taggers overlaps, and how this varies as a function of the parameters of the jets, such as their p_T and radius. This has been done by combining the variables into BDT discriminants, and comparing the background re-

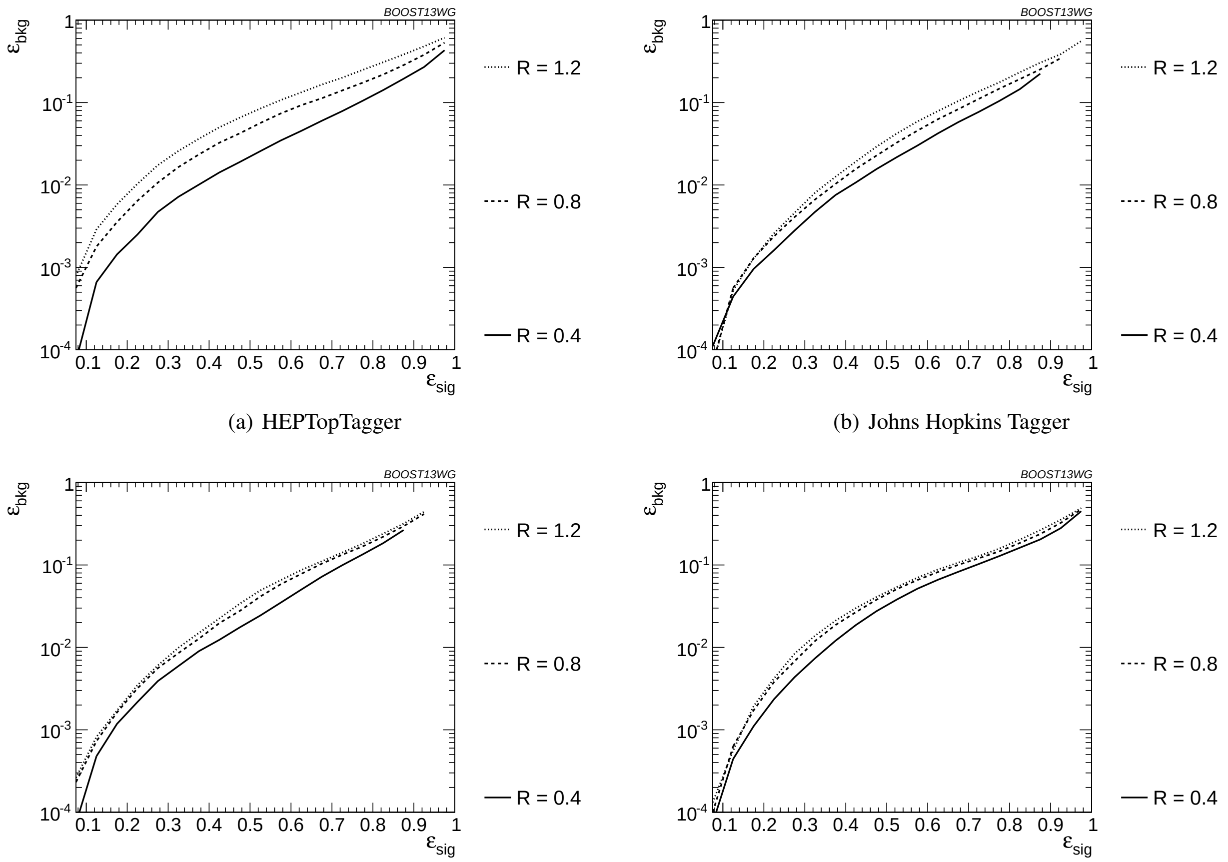

(a) HEPTopTagger (b) Johns Hopkins Tagger (c) Trimming (d) Pruning

Fig. 40 Comparison of tagger and jet shape performance at different radius at p_T = 1.5-1.6 TeV.

jection power of this discriminant to the rejection power achieved by the individual variables. The performance of "all variables" BDT discriminants has also been investigated, to understand the potential of the "ultimate" tagger where "all" available information (at least, all of that provided by the variables considered) is used.

Ideas for general conclusions:

– It is clear from both the q/g tagging and W tagging studies that the correlation structure between the observables considered is complicated, being both p_T and R dependent.

References

1. *Boost2009*, SLAC National Accelerator Laboratory, 9-10 July, 2009, [http://www-conf.slac.stanford.edu/Boost2009].
2. *Boost2010*, University of Oxford, 22-25 June 2010, [http://www.physics.ox.ac.uk/boost2010].
3. *Boost2011*, Princeton University, 22-26 May 2011, [https://indico.cern.ch/event/138809/].
4. *Boost2012*, IFIC Valencia, 23-27 July 2012, [http://ific.uv.es/boost2012].
5. *Boost2013*, University of Arizona, 12-16 August 2013, [https://indico.cern.ch/event/215704/].
6. *Boost2014*, University College London, 18-22 August 2014, [http://http://www.hep.ucl.ac.uk/boost2014/].
7. A. Abdesselam, E. B. Kuutmann, U. Bitenc, G. Brooijmans, J. Butterworth, et al., *Boosted objects: A Probe of beyond the Standard Model physics*, *Eur.Phys.J.* **C71** (2011) 1661, [arXiv:1012.5412].
8. A. Altheimer, S. Arora, L. Asquith, G. Brooijmans, J. Butterworth, et al., *Jet Substructure at the Tevatron and LHC: New results, new tools, new benchmarks*, *J.Phys.* **G39** (2012) 063001, [arXiv:1201.0008].
9. A. Altheimer, A. Arce, L. Asquith, J. Backus Mayes, E. Bergeaas Kuutmann, et al., *Boosted objects and jet substructure at the LHC*, arXiv:1311.2708.
10. M. Cacciari, G. P. Salam, and G. Soyez, *FastJet User Manual*, *Eur.Phys.J.* **C72** (2012) 1896, [arXiv:1111.6097].

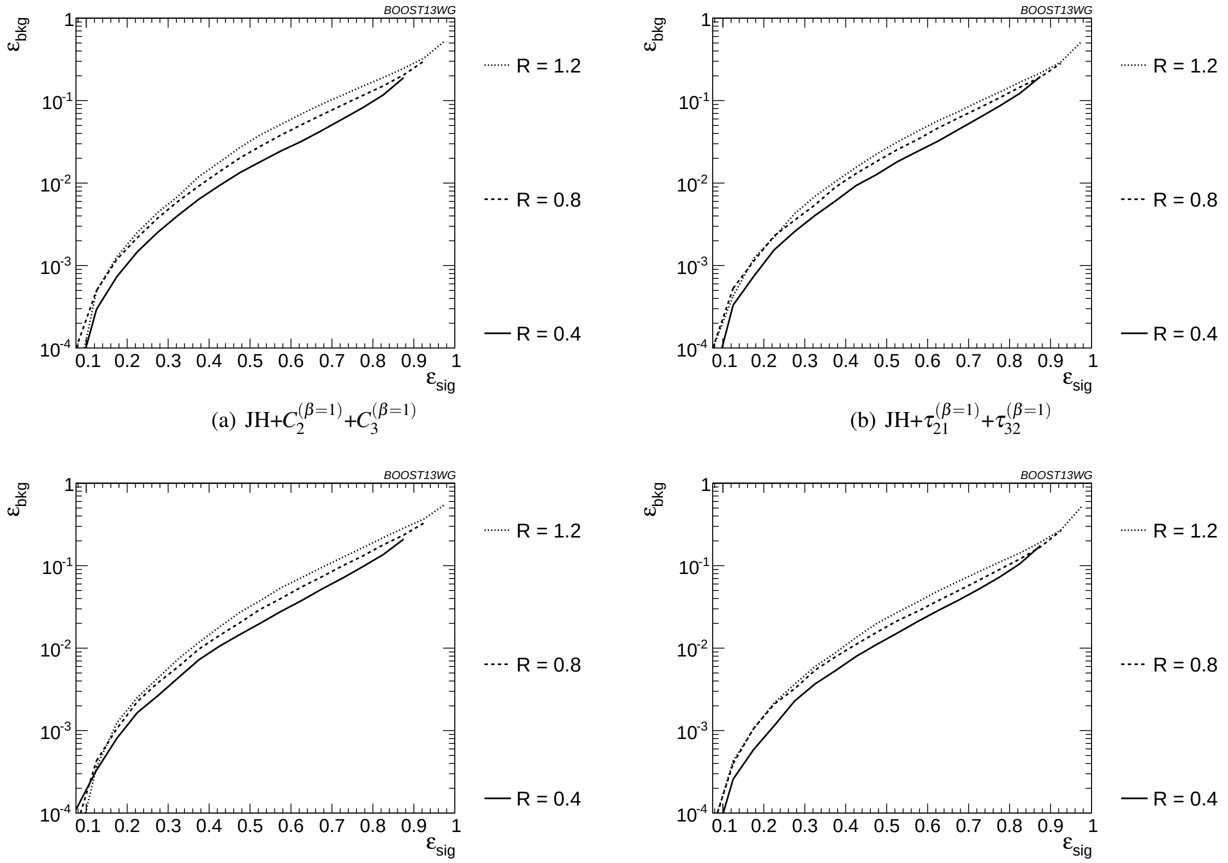

(a) JH+$C_2^{(\beta=1)}$+$C_3^{(\beta=1)}$

(b) JH+$\tau_{21}^{(\beta=1)}$+$\tau_{32}^{(\beta=1)}$

(c) JH + Qjet mass volatility

(d) JH + all

Fig. 41 Comparison of BDT combination of JH tagger + shape at different radius at p_T = 1.5-1.6 TeV.

11. T. Plehn, M. Spannowsky, M. Takeuchi, and D. Zerwas, *Stop Reconstruction with Tagged Tops*, *JHEP* **1010** (2010) 078, [arXiv:1006.2833].
12. D. E. Kaplan, K. Rehermann, M. D. Schwartz, and B. Tweedie, *Top Tagging: A Method for Identifying Boosted Hadronically Decaying Top Quarks*, *Phys.Rev.Lett.* **101** (2008) 142001, [arXiv:0806.0848].
13. J. Alwall, M. Herquet, F. Maltoni, O. Mattelaer, and T. Stelzer, *MadGraph 5 : Going Beyond*, *JHEP* **1106** (2011) 128, [arXiv:1106.0522].
14. Y. Gao, A. V. Gritsan, Z. Guo, K. Melnikov, M. Schulze, et al., *Spin determination of single-produced resonances at hadron colliders*, *Phys.Rev.* **D81** (2010) 075022, [arXiv:1001.3396].
15. S. Bolognesi, Y. Gao, A. V. Gritsan, K. Melnikov, M. Schulze, et al., *On the spin and parity of a single-produced resonance at the LHC*, *Phys.Rev.* **D86** (2012) 095031, [arXiv:1208.4018].
16. I. Anderson, S. Bolognesi, F. Caola, Y. Gao, A. V. Gritsan, et al., *Constraining anomalous HVV interactions at proton and lepton colliders*, *Phys.Rev.* **D89** (2014) 035007, [arXiv:1309.4819].
17. J. Pumplin, D. Stump, J. Huston, H. Lai, P. M. Nadolsky, et al., *New generation of parton distributions with uncertainties from global QCD analysis*, *JHEP* **0207** (2002) 012, [hep-ph/0201195].
18. T. Sjostrand, S. Mrenna, and P. Z. Skands, *A Brief Introduction to PYTHIA 8.1*, *Comput.Phys.Commun.* **178** (2008) 852–867, [arXiv:0710.3820].
19. A. Buckley, J. Butterworth, S. Gieseke, D. Grellscheid, S. Hoche, et al., *General-purpose event generators for LHC physics*, *Phys.Rept.* **504** (2011) 145–233, [arXiv:1101.2599].
20. T. Gleisberg, S. Hoeche, F. Krauss, M. Schonherr, S. Schumann, et al., *Event generation with SHERPA 1.1*, *JHEP* **0902** (2009) 007, [arXiv:0811.4622].
21. S. Schumann and F. Krauss, *A Parton shower algorithm based on Catani-Seymour dipole factorisation*, *JHEP* **0803** (2008) 038, [arXiv:0709.1027].
22. F. Krauss, R. Kuhn, and G. Soff, *AMEGIC++ 1.0: A Matrix element generator in C++*, *JHEP* **0202** (2002) 044, [hep-ph/0109036].

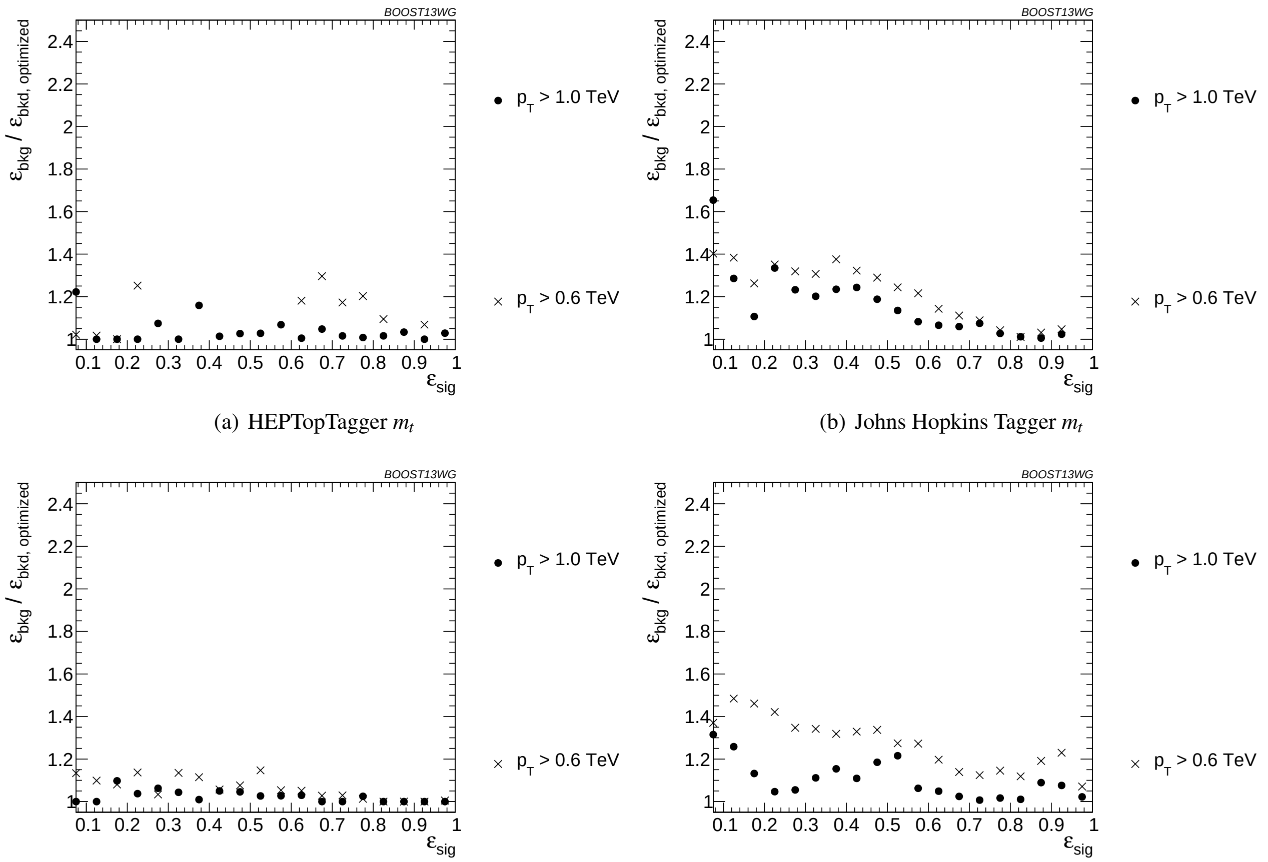

(a) HEPTopTagger m_t

(b) Johns Hopkins Tagger m_t

(c) Pruning m_t

(d) Trimming m_t

Fig. 42 Comparison of top mass performance of different taggers at different p_T using the anti-k_T R=0.8 algorithm; the tagger inputs are set to the optimum value for $p_T = 1.5 - 1.6$ TeV.

23. T. Gleisberg and S. Hoeche, *Comix, a new matrix element generator*, *JHEP* **0812** (2008) 039, [arXiv:0808.3674].
24. S. Hoeche, F. Krauss, S. Schumann, and F. Siegert, *QCD matrix elements and truncated showers*, *JHEP* **0905** (2009) 053, [arXiv:0903.1219].
25. M. Schonherr and F. Krauss, *Soft Photon Radiation in Particle Decays in SHERPA*, *JHEP* **0812** (2008) 018, [arXiv:0810.5071].
26. **JADE Collaboration** Collaboration, S. Bethke et al., *Experimental Investigation of the Energy Dependence of the Strong Coupling Strength*, *Phys.Lett.* **B213** (1988) 235.
27. M. Cacciari, G. P. Salam, and G. Soyez, *The Anti-k(t) jet clustering algorithm*, *JHEP* **0804** (2008) 063, [arXiv:0802.1189].
28. Y. L. Dokshitzer, G. Leder, S. Moretti, and B. Webber, *Better jet clustering algorithms*, *JHEP* **9708** (1997) 001, [hep-ph/9707323].
29. M. Wobisch and T. Wengler, *Hadronization corrections to jet cross-sections in deep inelastic scattering*, hep-ph/9907280.
30. S. Catani, Y. L. Dokshitzer, M. Seymour, and B. Webber, *Longitudinally invariant K_t clustering algorithms for hadron hadron collisions*, *Nucl.Phys.* **B406** (1993) 187–224.
31. S. D. Ellis and D. E. Soper, *Successive combination jet algorithm for hadron collisions*, *Phys.Rev.* **D48** (1993) 3160–3166, [hep-ph/9305266].
32. S. D. Ellis, A. Hornig, T. S. Roy, D. Krohn, and M. D. Schwartz, *Qjets: A Non-Deterministic Approach to Tree-Based Jet Substructure*, *Phys.Rev.Lett.* **108** (2012) 182003, [arXiv:1201.1914].
33. S. D. Ellis, A. Hornig, D. Krohn, and T. S. Roy, *On Statistical Aspects of Qjets*, *JHEP* **1501** (2015) 022, [arXiv:1409.6785].
34. S. D. Ellis, C. K. Vermilion, and J. R. Walsh, *Recombination Algorithms and Jet Substructure: Pruning as a Tool for Heavy Particle Searches*, *Phys.Rev.* **D81** (2010) 094023, [arXiv:0912.0033].
35. D. Krohn, J. Thaler, and L.-T. Wang, *Jet Trimming*, *JHEP* **1002** (2010) 084, [arXiv:0912.1342].
36. J. M. Butterworth, A. R. Davison, M. Rubin, and G. P. Salam, *Jet substructure as a new Higgs search channel*

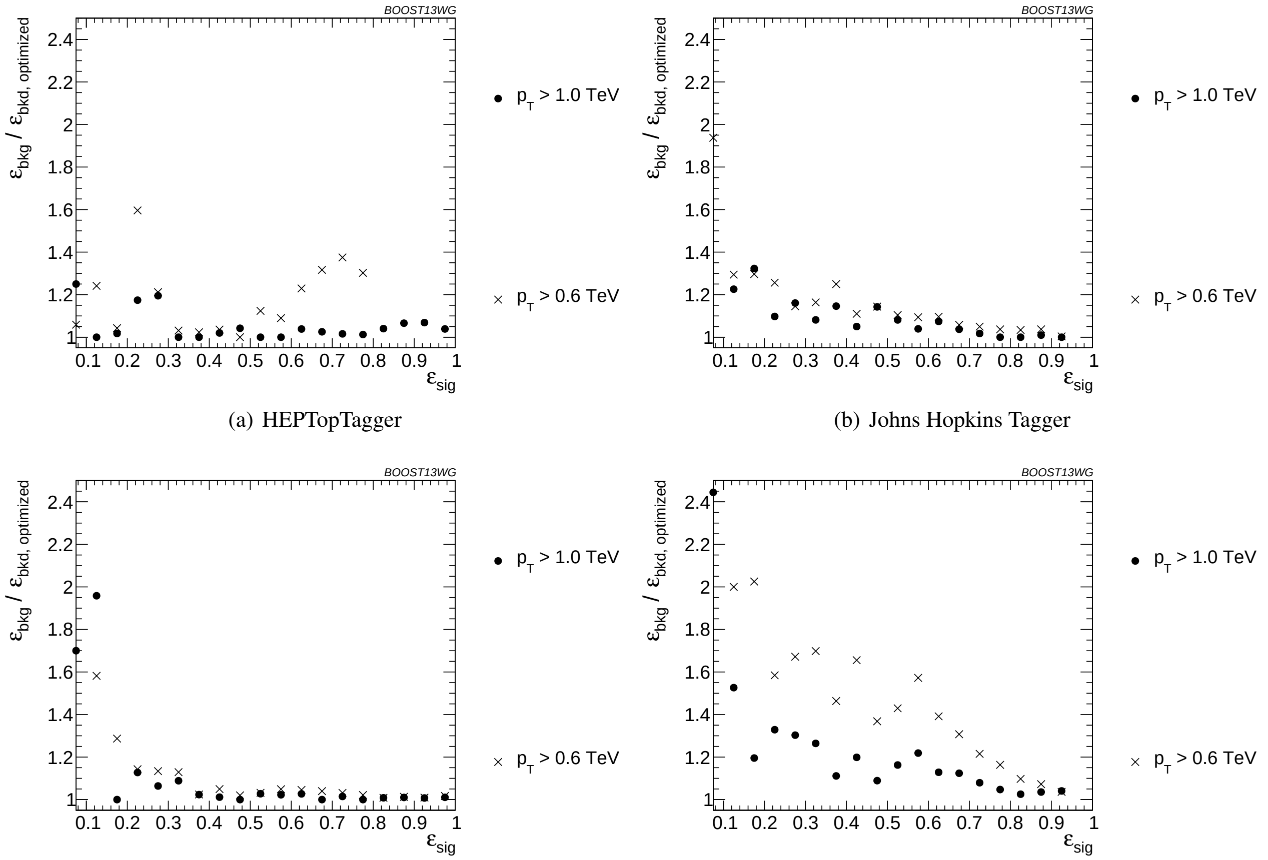

(a) HEPTopTagger (b) Johns Hopkins Tagger

(c) Pruning (d) Trimming

Fig. 43 Comparison of BDT combination of tagger performance at different p_T using the anti-k_T R=0.8 algorithm; the tagger inputs are set to the optimum value for $p_T = 1.5 - 1.6$ TeV.

at the LHC, *Phys.Rev.Lett.* **100** (2008) 242001, [arXiv:0802.2470].

37. A. J. Larkoski, S. Marzani, G. Soyez, and J. Thaler, *Soft Drop*, *JHEP* **1405** (2014) 146, [arXiv:1402.2657].
38. M. Dasgupta, A. Fregoso, S. Marzani, and G. P. Salam, *Towards an understanding of jet substructure*, *JHEP* **1309** (2013) 029, [arXiv:1307.0007].
39. J. Thaler and K. Van Tilburg, *Identifying Boosted Objects with N-subjettiness*, *JHEP* **1103** (2011) 015, [arXiv:1011.2268].
40. A. J. Larkoski, D. Neill, and J. Thaler, *Jet Shapes with the Broadening Axis*, *JHEP* **1404** (2014) 017, [arXiv:1401.2158].
41. A. J. Larkoski and J. Thaler, *Unsafe but Calculable: Ratios of Angularities in Perturbative QCD*, *JHEP* **1309** (2013) 137, [arXiv:1307.1699].
42. A. J. Larkoski, G. P. Salam, and J. Thaler, *Energy Correlation Functions for Jet Substructure*, *JHEP* **1306** (2013) 108, [arXiv:1305.0007].
43. A. Hoecker, P. Speckmayer, J. Stelzer, J. Therhaag, E. von Toerne, and H. Voss, *TMVA: Toolkit for Multivariate Data Analysis*, *PoS* **ACAT** (2007) 040, [physics/0703039].
44. **ATLAS Collaboration** Collaboration, G. Aad et al., *Light-quark and gluon jet discrimination in pp collisions at* $\sqrt{s} = 7$ TeV *with the ATLAS detector*, *Eur.Phys.J.* **C74** (2014), no. 8 3023, [arXiv:1405.6583].
45. J. Gallicchio and M. D. Schwartz, *Quark and Gluon Jet Substructure*, *JHEP* **1304** (2013) 090, [arXiv:1211.7038].
46. J. Gallicchio and M. D. Schwartz, *Quark and Gluon Tagging at the LHC*, *Phys.Rev.Lett.* **107** (2011) 172001, [arXiv:1106.3076].
47. S. D. Ellis, C. K. Vermilion, and J. R. Walsh, *Techniques for improved heavy particle searches with jet substructure*, *Phys.Rev.* **D80** (2009) 051501, [arXiv:0903.5081].
48. C. Anders, C. Bernaciak, G. Kasieczka, T. Plehn, and T. Schell, *Benchmarking an Even Better HEPTopTagger*, *Phys.Rev.* **D89** (2014) 074047, [arXiv:1312.1504].

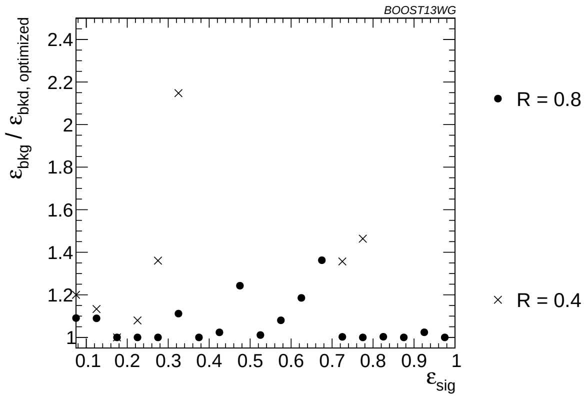

(a) HEPTopTagger m_t

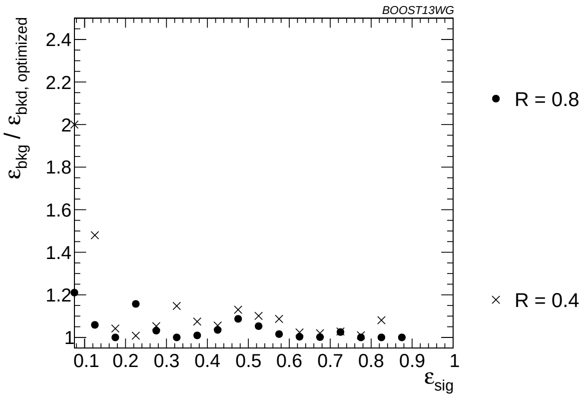

(b) Johns Hopkins Tagger m_t

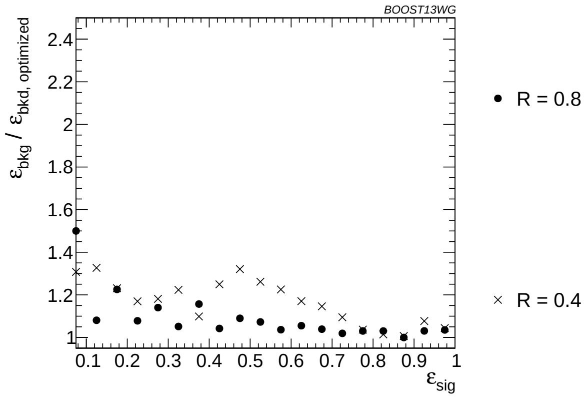

(c) Pruning m_t

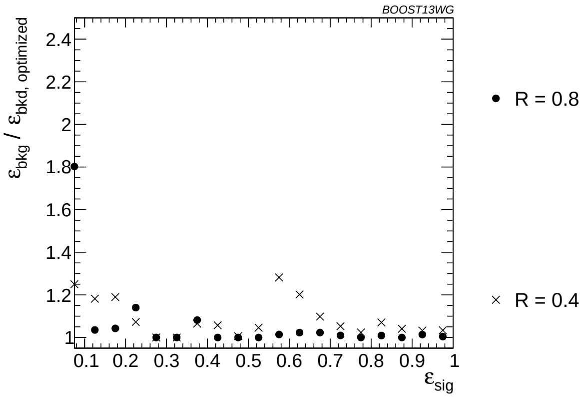

(d) Trimming m_t

Fig. 44 Comparison of top mass performance of different taggers at different R in the $p_T = 1500-1600$ GeV bin; the tagger inputs are set to the optimum value for $R = 1.2$.

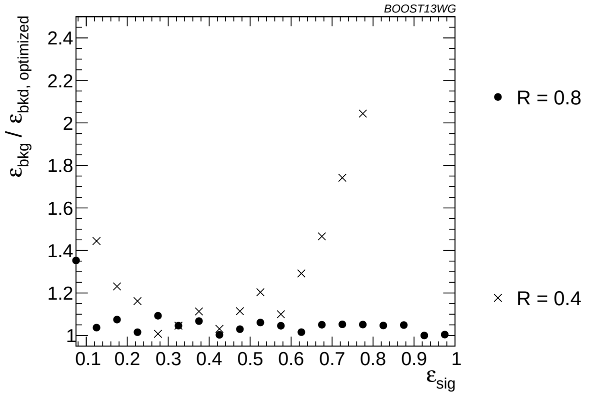

(a) HEPTopTagger

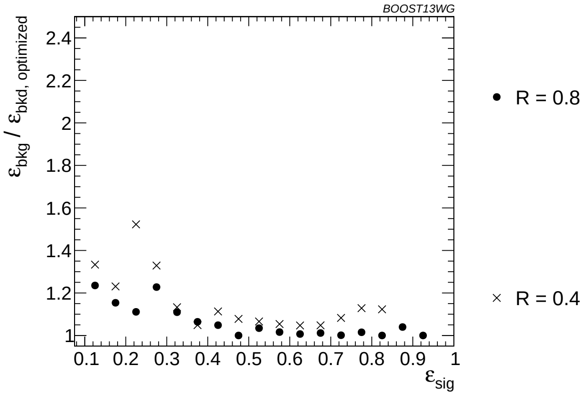

(b) Johns Hopkins Tagger

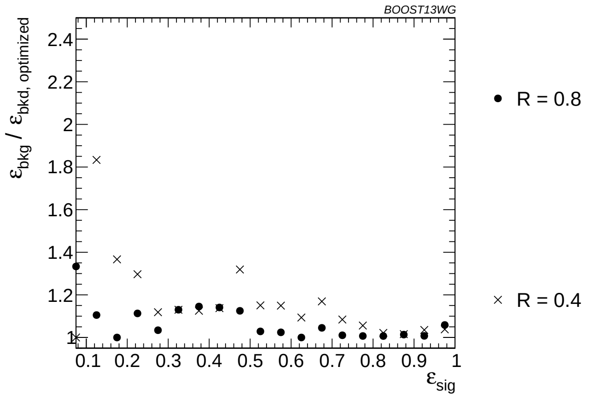

(c) Pruning

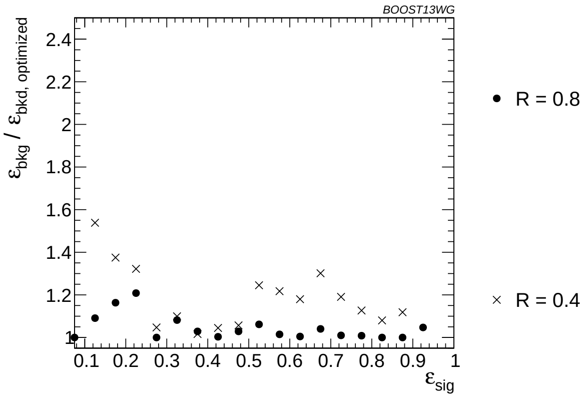

(d) Trimming

Fig. 45 Comparison of BDT combination of tagger performance at different radius at p_T = 1.5-1.6 TeV; the tagger inputs are set to the optimum value for $R = 1.2$.

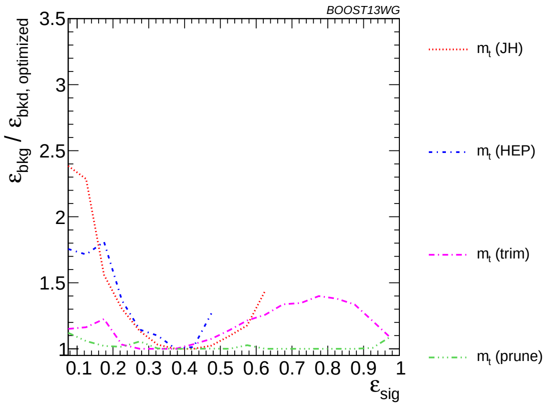

(a) Top mass

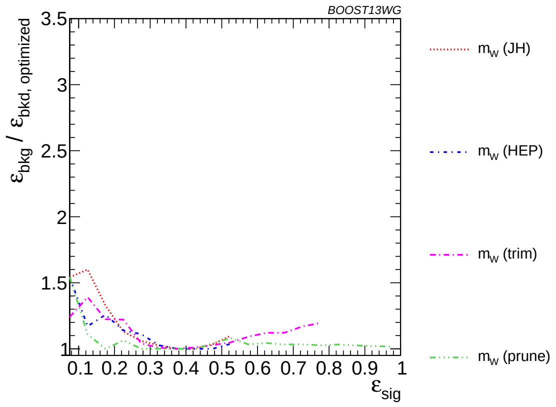

(b) W mass

Fig. 46 Comparison of single-variable top-tagging performance in the $p_T = 1 - 1.1$ GeV bin using the anti-k_{T}, R=0.8 algorithm; the inputs for each tagger are optimized for the $\varepsilon_{\mathrm{sig}} = 0.3 - 0.35$ bin.

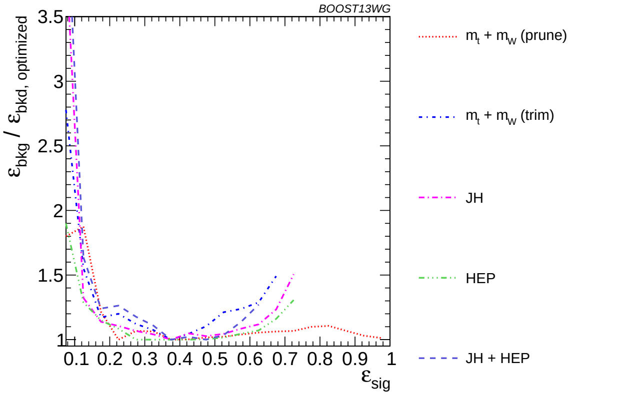

(a) Tagger-Groomer comparison

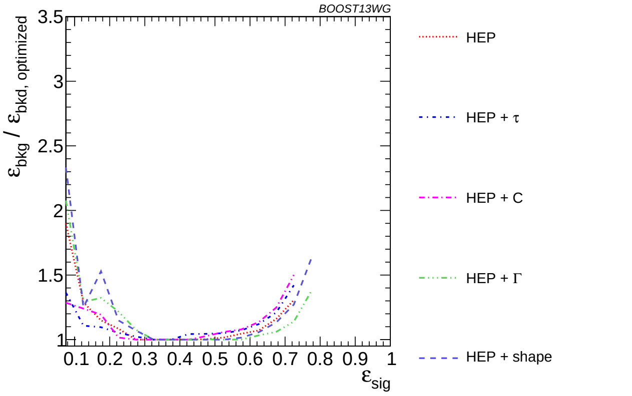

(b) HEPTopTagger + Shape

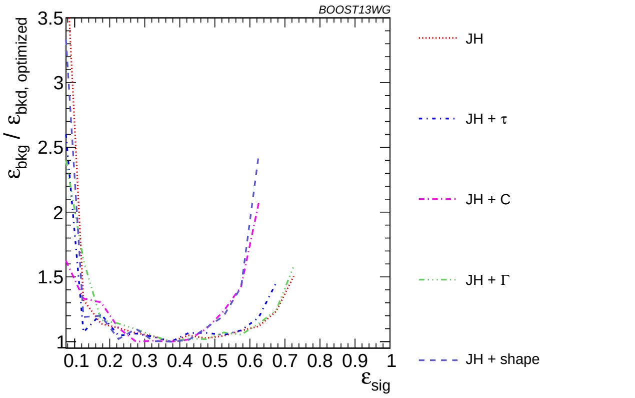

(c) Johns Hopkins Tagger + shape

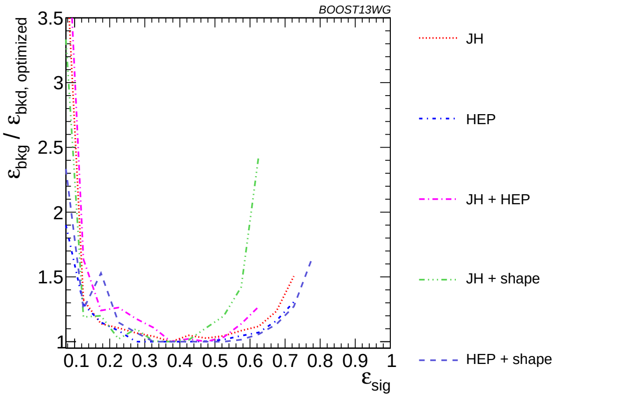

(d) HEP vs. JH comparison (incl. shape)

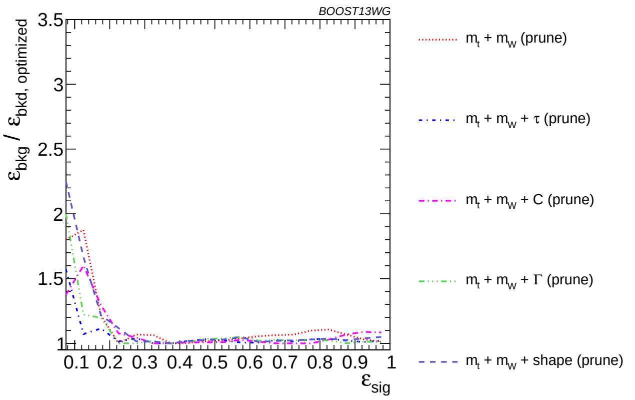

(e) Pruning + Shape

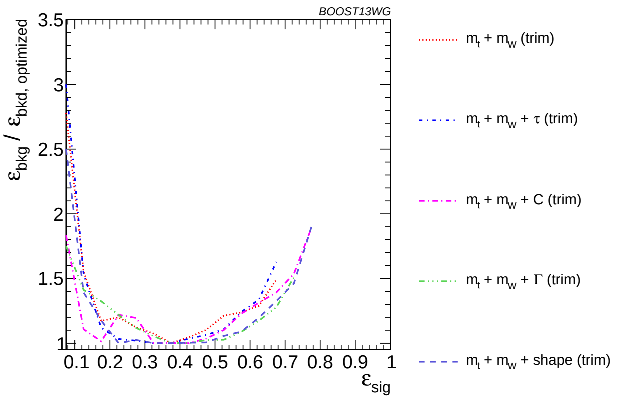

(f) Trimming + Shape

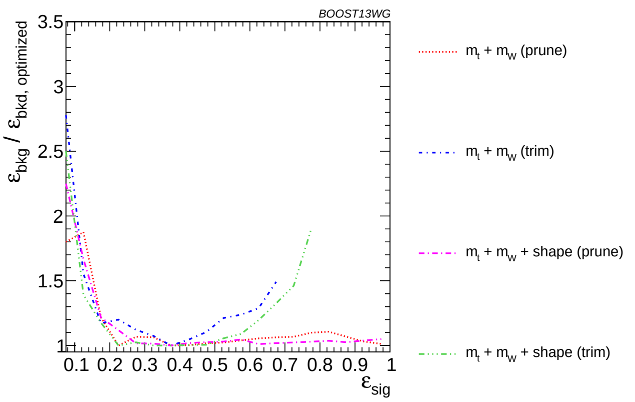

(g) Trim vs. Prune comparison (incl. shape)

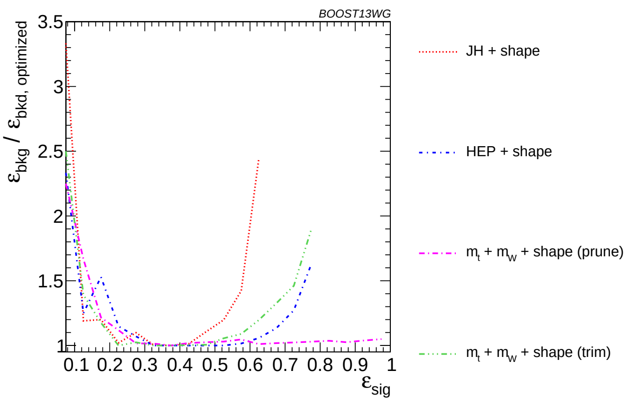

(h) Comparison of all Tagger+Shape

Fig. 47 The BDT combinations in the $p_T = 1 - 1.1$ TeV bin using the anti-k_T R=0.8 algorithm. Taggers are combined with the following shape observables: $\tau_{21}^{(\beta=1)} + \tau_{32}^{(\beta=1)}$, $C_2^{(\beta=1)} + C_3^{(\beta=1)}$, Γ_{Qjet}, and all of the above (denoted "shape"). The inputs for each tagger are optimized for the $\varepsilon_{\mathrm{sig}} = 0.3 - 0.35$ bin.